The Pennsylvania State University

The Graduate School

Department of Physics

A RAMAN AND RAYLEIGH SCATTERING STUDY OF ELECTRICAL AND PHONON PROPERTIES OF SEMICONDUCTING NANOWIRES

A Dissertation in

Physics

by

Qiujie Lu

Submitted in Partial Fulfillment
of the Requirements
for the Degree of

Doctor of Philosophy

August 2010

The dissertation of Qiujie Lu was reviewed and approved* by the following:

Nitin Samarth
Professor of Physics
Dissertation Advisor
Chair of Committee

Gerald D. Mahan
Distinguished Professor of Physics

Vincent H. Crespi
Professor of Physics
Professor of Materials Science and Engineering

John V. Badding
Professor of Chemistry

Jayanth R. Banavar
Distinguished Professor of Physics
Head of the Department of Physics

*Signatures are on file in the Graduate School

ABSTRACT

Semiconducting nanowires have the potential to become the next generation of building blocks for nanoelectronics, optoelectronics and sensors. Due to the their quasi-one-dimensional nature and high aspect ratio, semiconducting nanowires exhibit distinct phonon and electrical properties compared to the bulk. This thesis collects three original studies focusing on both computational and experimental results of light scattering from semiconducting nanowires.

The first study focuses on Raman scattering results on $Si_{1-x}Ge_x$ nanowires ($0<x<1$) grown by the vapor-liquid-solid (VLS) growth mechanism using a chemical vapor deposition (CVD). Transmission electron microscopy (TEM) and X-ray diffraction (XRD) were used to characterize the morphology growth axis and lattice constant of these materials. Typical wire diameters were in the range 80-130 nm. Based on Raman scattering studies of the bulk, three Raman bands are expected that can be identified as a perturbed Si-Si (~500 cm^{-1}) mode, a Ge-Ge (~280 cm^{-1}) mode and a new mode (~390 cm^{-1}) assigned to Si-Ge or Ge-Si clusters. Peaks in this region are also observed in the case of our nanowires, although the frequencies are a few cm^{-1} lower than observed in the bulk. We also observe that the compositional (x) dependence of the Si-Ge band in nanowires is somewhat different than that in the bulk.

The second research project studies the Rayleigh and Raman scattering from GaP semiconducting nanowires with different polarized incident excitations. GaP nanowires were grown using pulsed laser vaporization (PLV). The diameters of the nanowires range from 50 nm to 500 nm. Rayleigh and Raman spectra were obtained from single GaP

nanowires suspended over TEM grid holes. Experiments show that the plots of the scattering intensity vs. the polarization of the incident laser depend on the diameters of the nanowires. Mie theory, the discrete dipole approximation (DDA) and the finite difference time domain (FDTD) methods were used to explain this dependence.

The third study focuses on the internal electric field's dependence on the position of the laser spot relative to the nanowire. About 60% of the Raman scattering spectra from the tips of GaP nanowires were greater than the scattering intensities from the center of the same nanowire. This enhancement factor (ratio of the TO mode intensity at a tip to the TO mode intensity at the center) is around 3~5 for GaP nanowires measured on Si substrates and about 1~2 for GaP nanowires suspended over TEM grid holes. The effect of polarization and energy of the incident excitation on the enhancement factor was studied experimentally with GaP nanowires over TEM grid holes. Further, the FDTD method was applied to compute the theoretical enhancement factor. We carried out a statistical exploration to understand the deviation of the enhancement factor from its computed value.

TABLE OF CONTENTS

LIST OF FIGURES

LIST OF TABLES

ACKNOWLEDGEMENTS

I would like to acknowledge my advisers Prof. Peter C. Eklund and Prof. Nitin Samarth for their persistent and patient education and encouragement. It was their insight and enthusiasm in physics that inspired me into the fascinating nanophysics and guided me through the difficulties in my career. I also owe the great gratitude to my committee numbers: Prof. Gerald D. Mahan, Prof. Vincent H. Crespi, Prof. John V. Badding for their help and suggestions in my research. I give special thanks to my colleagues, Dr. Gugang Chen (Honda Research Institute, USA), Dr. Qihua Xiong (Nanyang Technological University, Singapore), Dr. Humberto R. Gutierrez and Dr. Jian Wu for sharing with me their valuable experience and giving me helpful suggestions. I also want to thank my other group members who gave a lot of help. They are Dr. Xiaoming Liu, Dr. Timothy J. Russin, Dr. Awnish K. Gupta, Dr. Hugo E. Romero, Mr. Duming Zhang, Ms. Bei Wang and Mr. Qingzhen Hao.

Finally, I would like to thank my parents and my friends for their support over years. For the encouragement and joy they gave me in my life, I dedicate my thesis to them.

Chapter 1

Introduction

1.1 Motivation of Thesis

Scientists and engineers have studied semiconductors for over a century, with growing interest in nanoscale semiconductor crystals. In this context, semiconductor nanowires have attracted increasing interest during the last decade due to their potential to become the next generation of building blocks for electronic devices [1]. The reduced size, dimensionality and the increasing aspect ratio for nanowires introduce unique electrical and optical scattering characteristics which are absent from bulk or thin film materials. The purpose of this study is to uncover the intriguing phonon and electrical properties of semiconducting nanowires arising from either the reduced size of the nanowires or the different aspect ratio of the nanowires compared to the bulk.

1.2 Structure of Thesis

Chapter two reviews the growth mechanism and procedures for semiconducting nanowires studied in this thesis. Chapter three will discuss the classical and quantum theory of Raman and Rayleigh scattering. Chapter four focuses on similarity and difference in phonon properties between Si_xGe_{1-x} bulk and nanowire batches. Chapter five presents three methods to compute the electric field inside a nanowire and the

scattering of electromagnetic waves by a nanowire. These include Mie theory, the Discrete Dipole Approximation (DDA) and Finite Difference Time Domain (FDTD) simulations. The last two chapters focus on Raman scattering from single GaP nanowires. Chapter six discusses the internal electric field's dependence on the incident laser polarization. Chapter seven deals with the electric field's dependence on the position of the laser spot relative to the nanowire.

Chapter 2

Synthesis of Semiconducting Nanowires in This Thesis

2.1 Vapor-Liquid-Solid (VLS) Growth Mechanism

The Vapor-Liquid-Solid (VLS) growth mechanism is the most widely used and successful technique in synthesizing crystalline nanowires in large quantities. VLS growth was first proposed by Wagner and Ellis [2] to explain whisker growth in 1964. Not until 2001 was VLS growth directly observed by Yiying Wu and Peidong Yang in *in situ* TEM studies [3].

Figure 2-1 is a TEM image taken by Yiying Wu and Peidong Yang [3] showing three stages of nanowire growth by VLS growth mechanism. VLS growth of nanowires typically uses metal nanoparticles, for example Au or Fe, as the catalyst, and these seed particles initiate nanowire growth. In Wu and Yang's experiment, Au was used as the catalyst, and the sample stage was maintained at 800 - 900 °C.

The first stage in VLS nanowire growth is called alloying. In this stage, chemical reactions take place between seed particles and the vapor of the target nanowire's chemical elements. This stage is illustrated in Figure 2-1 (a)-(c). The Au nanoclusters react with Ge vapor and form Au-Ge liquid alloy. In Figure 2-2, this stage is also represented by an isothermal line on the Au-Ge phase diagram.

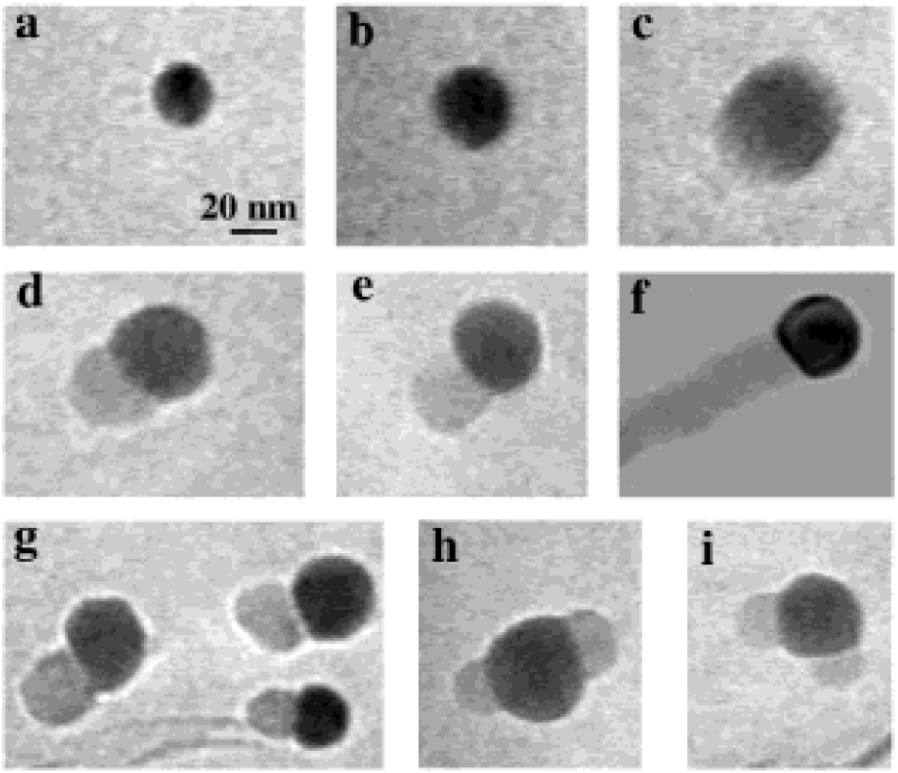

Figure 2-1: *In situ* TEM images recorded the process of Ge nanowire growth by VLS growth mechanism. (a) Au nanoclusters in solid state at 500 °C; (b) alloying initiates at 800 °C, and Au is in mostly solid state; (c) liquid Au-Ge alloy; (d) the nucleation of Ge nanocrystal on the alloy surface; (e) Ge nanocrystal elongates with further Ge condensation and eventually a wire starts to form; (f), (g) Several other examples of Ge nanowire nucleation; (h), (i) two nucleation events on single alloy droplet [3].

The second stage is nucleation, depicted in Figure 2-1 (d) (e). As more Ge vapor dissolves into the Au-Ge liquid alloy and the composition of the alloy crosses the second liquidus line shown in Figure 2-2 (b), Ge becomes oversaturated and starts to precipitate. The composition enters another biphasic region (Au-Ge alloy and Ge crystal).

The third stage is axial growth, shown in Figure 2-1 (d)-(f). After the Ge nanocrystal nucleates at the liquid-solid interface, further condensation and dissolution of

Ge vapor into the Au-Ge liquid alloy increases the amount of Ge crystal precipitation from the alloy. Because less energy is needed with crystal step growth compared to secondary nucleation events in a finite volume [3], Ge will prefer to diffuse and condense at the existing liquid-solid interface and therefore form a nanowire. This is illustrated as a cartoon in Figure 2-2 (a) II III.

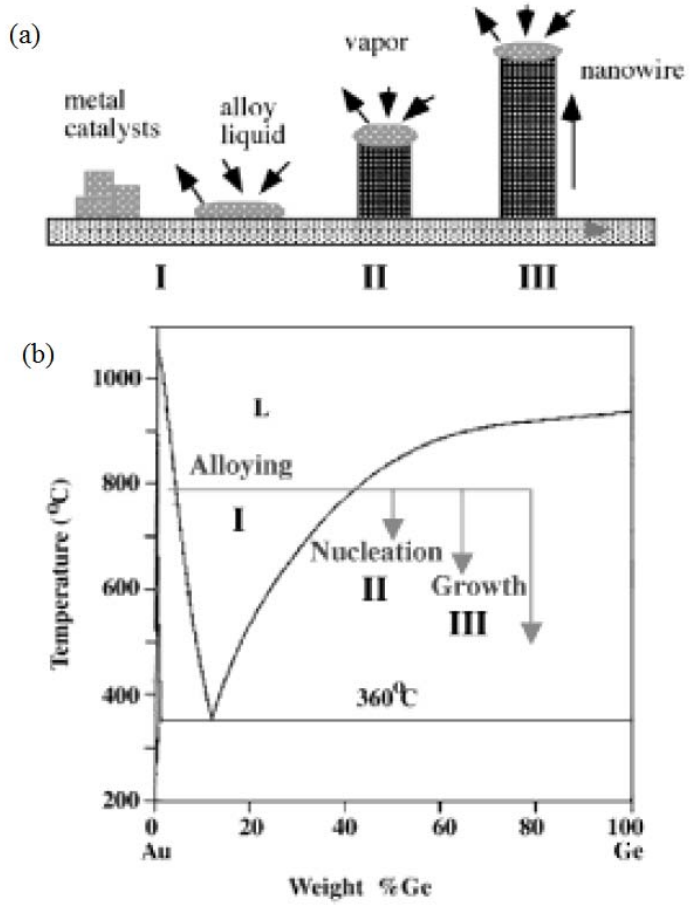

Figure 2-2: Three stages in VLS nanowire growth mechanism shown in (a) a schematic illustration; (b) conventional Au-Ge binary phase diagram [3].

The $Si_{1-x}Ge_x$ and GaP nanowires studied in this thesis were all grown by the VLS growth mechanism and I will discuss the detailed growth methods for each of them.

2.2 Chemical Vapor Deposition (CVD) Growth Method for $Si_{1-x}Ge_x$ Nanowires

The growth procedure of $Si_{1-x}Ge_x$ nanowires follows the method described in Ref. [4]. Commercial anodic alumina membranes with nominal 200 nm diameter pores were used as a platform. A 5 micron long segment of Ag was deposited in the pores, and afterwards, a 0.25 micron long Au segment was deposited in those pores. The Ag segment was removed by etching in 8.0M HNO_3 so that only the thin Au segment near the top of the membrane was left to serve as the catalyst.

However, because of low growth rate of $Si_{1-x}Ge_x$ nanowires with x greater than 0.8, those nanowires were grown on Si(111) substrate coated with a 200 nm thick Au film instead of on the anodic alumina membranes.

Figure 2-3 illustrates the CVD setup of $Si_{1-x}Ge_x$ nanowire growth. The alumina membranes or the Si(111) substrates were placed at the center of an isothermal quartz reactor tube. The growth temperature was maintained as a constant between 325 °C to 500 °C. $Si_{1-x}Ge_x$ nanowires grown under different growth temperature have different Ge concentration x.

SiH_4 and GeH_4 were used as gaseous precursor sources for the growth of $Si_{1-x}Ge_x$ nanowires growth. The total pressure within the quartz reactor was held constant at 13 Torr using 10% mixture of SiH_4 in H_2 and 1% or 2% GeH_4 in H_2. The total gas rate was held constant as 100 sccm. The flow rate of each source gas was adjusted to control the inlet gas ratio of GeH_4 / (SiH_4 + GeH_4) from 0.01 to 0.67. The difference in the inlet gas ratio also had influence over the Ge composition in $Si_{1-x}Ge_x$ nanowires.

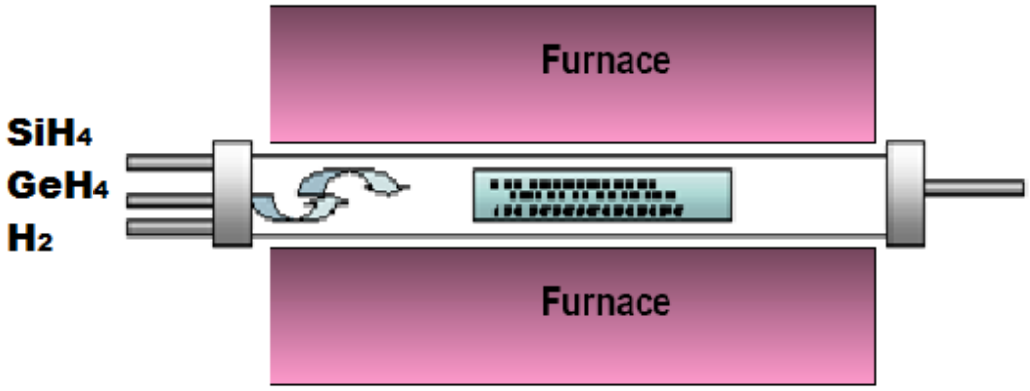

Figure 2-3: $Si_{1-x}Ge_x$ nanowire growth by CVD.

2.3 Pulsed Laser Vaporization (PLV) Growth Method for GaP Nanowires

GaP crystals were first mixed with micron size Au particles (catalyst) at the weight ratio of 95% GaP to 5% Au. The mixture was ground into a powder and further milled in a ball miller for several hours. The fine powders were placed inside a pellet press as illustrated by the cartoons in Figure 2-4 (a)-(c) [5], and this pellet was applied uni-axial pressure at 5 metric tons for half day. After this treatment, GaP-Au powders became a deeply-pressed compact cylindrical tablet similar as the one shown in Figure 2-4 (d). This tablet is called a target because it is ablated by a laser in subsequent PLV growth method. The GaP-Au target was held by a target holder, such as the one in Figure 2-4 (e), and put into a quartz reactor tube at place "A" in Figure 2-5. Argon flowed through the quartz reactor tube at 100 sccm to carry the GaP vapor plume downstream and at a pressure inside the tube of 200 torr. The temperature of the furnace was maintained to be 880-920 °C.

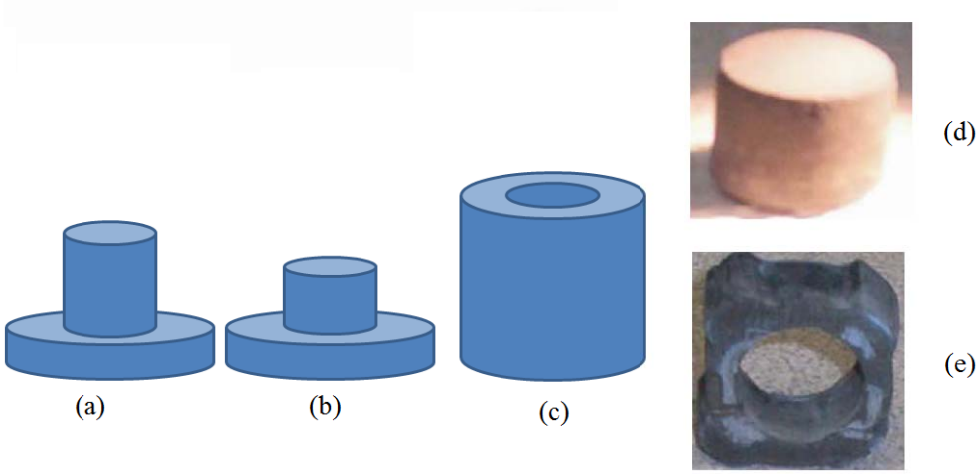

Figure 2-4: PLV target preparation. schematic illustration of (a) top of a pellet press; (b) bottom of a pellet press; (c) barrel of a pellet press; picture of (d) fresh prepared target taken out from a pullet press; (e) target holder [5].

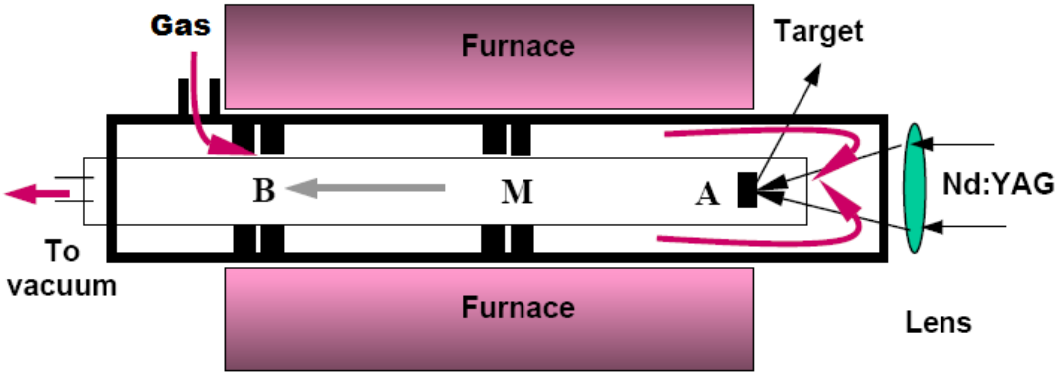

Figure 2-5: GaP Nanowire growth by PLV.

In Figure 2-5, the lens was connected to a computer-controlled motor and moved along a zigzag path as depicted in Figure 2-6, so that the laser ablated evenly on the target tablet. The small green solid circle in Figure 2-6 represents the laser spot. Though the green circles are discrete in the figure, the actual movement of laser spot was continuous

without any stop as indicated by the red lines. Odd runs and even runs were following different directions for the purpose of even laser ablation.

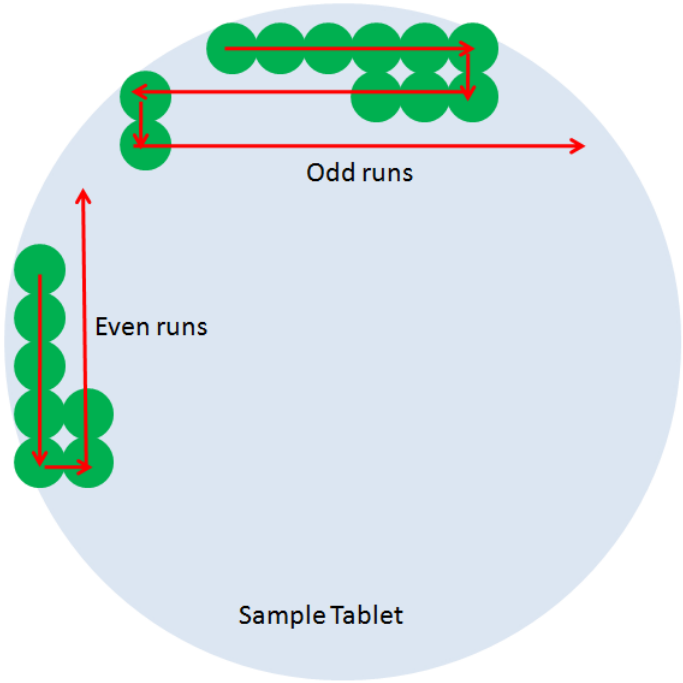

Figure 2-6: Illustration of laser spot movement in PLV.

A narrow quartz collection tube was placed between position “B” and “M” in Figure 2-5 to harvest GaP nanowires grown by this method.

2.4 Chemical Vapor Deposition (CVD) Growth Method for GaP Nanowires

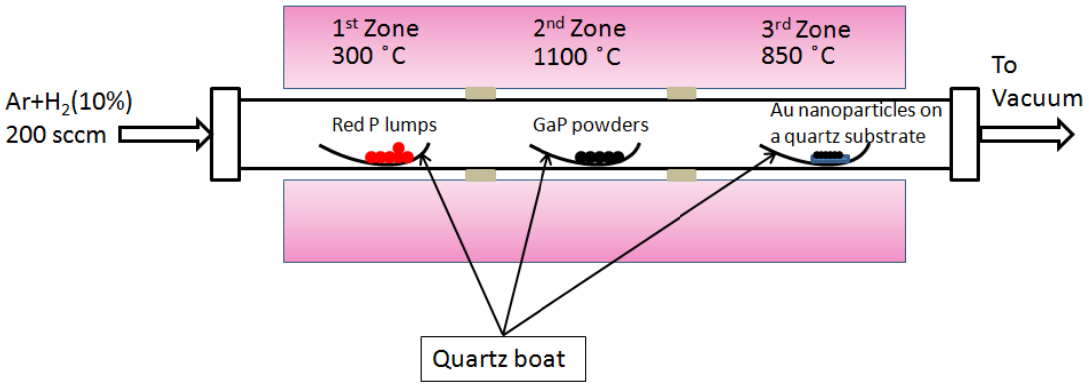

Figure 2-7: GaP nanowire growth by CVD.

For CVD growth of GaP nanowires, a three-zone furnace was used. The temperature of each zone can be controlled independently and was set to 300 °C, 1100 °C and 850 °C for the 1st, 2nd, and 3rd zone, respectively. As illustrated in Figure 2-1, we placed one quartz boat in each zone, and have red phosphorous lumps, GaP powders, and a quartz substrate with Au nanoparticles with diameters around 20nm on it in each quartz boat. A 200 sccm Ar+H^2(10%) kept flowing to maintain a 300torr pressure inside the quartz reaction tube during the synthesis. GaP nanowires were grown both on the quartz substrate and on the quartz boat in the third zone. While the GaP nanowires grown on the substrate have Au particles on the tips, the nanowires harvested from the quartz boat do not have gold particles with them.

Chapter 3

Rayleigh and Raman Scattering

3.1 Introduction to Rayleigh and Raman Scattering

When monochromatic light is incident on systems smaller than its wavelength such as nanowires, most of it will be scattered without change in frequency. This is called "Rayleigh Scattering" after the English physicist Lard Rayleigh. However, a weaker part of the scattering is inelastic and is called Raman scattering.

The scattering with change of frequency was predicted theoretically by Smekal in 1923 and was discovered by Sir C.V. Raman in February 1928. Raman was awarded the Nobel Prize for Physics in 1930 for this discovery. The Raman effect is important in several ways. The difference in wavenumber between the incident radiation and scattered light carries with it information about the vibrational and rotational energy levels of the molecules and atoms in a condensed matter system. This makes Raman spectroscopy a powerful method to study energy level in such systems. Furthermore, in some cases, certain lines or transitions may be entirely forbidden in the infrared spectroscopy by selection rules. So Raman spectra are needed to provide us with the maximum information about molecules and condensed matter systems.

3.2 Classical Theory of Rayleigh and Raman Scattering

The normal Raman effect is the result of a double photon transition involving three energy levels. The classical theory is intuitive and provides much insight into this effect. When light of frequency ω is incident onto a system, it induces a dipole moment p, which is given by the following equation in the first order approximation [6]:

$$\vec{p}^{(1)} = \boldsymbol{\alpha} \cdot \vec{E}, \tag{3.1}$$

where $\vec{p}^{(1)}$ is the frequency-dependent linearly induced electric dipole vector, $\boldsymbol{\alpha}$ is the polarizability tensor of the molecule and $\vec{E}$ is the electric field of the incident monochromatic light.

The electric field of the incident light is given by:

$$\vec{E} = \vec{E}_0 \, cos(\omega t). \tag{3.2}$$

This electromagnetic wave is scattered by the molecule/atom in a condensed matter system which is free to vibrate but not rotate. Thus, the molecule/atom is fixed in its equilibrium position and may vibrate about this position. The variation of the polarizability due to the vibration can be expressed by expanding each component $\alpha_{\rho\sigma}$ of polarizability tensor $\boldsymbol{\alpha}$ in a Taylor series with respect to the normal coordinates as:

$$\alpha_{\rho\sigma} = (\alpha_{\rho\sigma})_0 + \sum_k (\frac{\partial \alpha_{\rho\sigma}}{\partial Q_k})_0 Q_k + \frac{1}{2} \sum_{k,l} (\frac{\partial^2 \alpha_{\rho\sigma}}{\partial Q_k \partial Q_l})_0 Q_k Q_l \ldots, \tag{3.3}$$

where $(\alpha_{\rho\sigma})_0$ is the value of $\alpha_{\rho\sigma}$ at the equilibrium position, $Q_k, Q_l \ldots$ are normal coordinates of vibration associated with the molecular vibrational frequencies $\omega_k, \omega_l \ldots$, and the summations are over all normal coordinates. The subscript "0" on the derivatives indicates that these values are taken at the equilibrium position. Here, we neglect the

terms involving powers of Q higher than the first. This is often called electrical harmonic approximation. For simplicity, we limit ourselves to only one normal mode of the vibration Q_k. We can rewrite Eq. (3.3) as:

$$(\alpha_{\rho\sigma})_k = (\alpha_{\rho\sigma})_0 + (\alpha'_{\rho\sigma})_k Q_k, \tag{3.4}$$

where

$$(\alpha'_{\rho\sigma})_k = (\frac{\partial \alpha_{\rho\sigma}}{\partial Q_k})_0. \tag{3.5}$$

The $(\alpha'_{\rho\sigma})_k$ are components of a new tensor $\boldsymbol{\alpha'_k}$ whose components are polarizability derivatives with respect to the normal coordinates Q_k.

As Eq. (3.4) is valid for all tensor components, we can write:

$$\boldsymbol{\alpha_k} = \boldsymbol{\alpha_0} + \boldsymbol{\alpha'_k} Q_k, \tag{3.6}$$

where $\boldsymbol{\alpha_k}$ is a tensor with components $(\alpha_{\rho\sigma})_k$ and Q_k, a scalar quantity, multiplies all components of $\boldsymbol{\alpha'_k}$. Assuming simple harmonic motion, Q_k can be put as:

$$Q_k = Q_{k_0} cos\,(\omega_k t + \delta_k), \tag{3.7}$$

where Q_{k_0} is the normal coordinate amplitude and δ_k is a phase factor. Putting (3.7) into (3.6), we obtain:

$$\boldsymbol{\alpha_k} = \boldsymbol{\alpha_0} + \boldsymbol{\alpha'_k} Q_{k_0} cos\,(\omega_k t + \delta_k). \tag{3.8}$$

Combining Eq. (3.8) with (3.1) and (3.2), we obtain:

$$\vec{p}^{(1)} = \boldsymbol{\alpha_0} \cdot \vec{E}_0\, cos(\omega t) + \boldsymbol{\alpha'_k} \vec{E}_0 Q_{k_0} cos\,(\omega_k t + \delta_k)\, cos(\omega t). \tag{3.9}$$

Using the relation:

$$cos(A)\, cos(B) = \frac{1}{2}[cos(A+B) + cos(A-B)], \tag{3.10}$$

Eq. (3.9) can be written as:

$$\vec{p}^{(1)} = \vec{p}^{(1)}(\omega) + \vec{p}^{(1)}(\omega - \omega_k) + \vec{p}^{(1)}(\omega + \omega_k), \tag{3.11}$$

where

$$\vec{p}^{(1)}(\omega) = \vec{p}_0^{Ray} cos\,(\omega t), \tag{3.12}$$

$$\vec{p}^{(1)}(\omega \pm \omega_k) = \vec{p}_{k_0}^{Ram} cos\,[(\omega \pm \omega_k \pm \delta_k)t], \tag{3.13}$$

with

$$\vec{p}_0^{Ray} = \boldsymbol{\alpha^{Ray}} \cdot \overrightarrow{E_0}\,, \tag{3.14}$$

$$\vec{p}_{k_0}^{Ram} = \boldsymbol{\alpha_k^{Ram}} \cdot \overrightarrow{E_0}, \tag{3.15}$$

$$\boldsymbol{\alpha^{Ray}} = \boldsymbol{\alpha_0}, \tag{3.16}$$

$$\boldsymbol{\alpha_k^{Ram}} = \frac{1}{2}\boldsymbol{\alpha'_k} Q_k. \tag{3.17}$$

The superscripts ‘Ray’ and ‘Ram’ are abbreviations for ‘Rayleigh’ and ‘Raman’ respectively. The cosine functions in Eq. (3.12) and (3.13) define the frequencies of the induced dipoles. Eq. (3.16) and (3.17) define the classical Rayleigh and Raman scattering tensor.

Based on eq. (3.11), we reach one of the most important conclusions concerning Rayleigh and Raman scattering. After the incident light, the condensed matter system emits light in three frequencies, ω (Rayleigh scattering), $(\omega + \omega_k)$ (Anti Stokes scattering) and $(\omega - \omega_k)$ (Stokes scattering). Qualitatively, this also illustrates that Rayleigh scatterings are much stronger than Raman scatterings because of their different dependence on the polarizability tensor.

However, the classical treatment does not ascribe specific discrete rotational frequencies to molecules and the result for the vibrational Raman scattering tensor given

by Eq. (3.17) is partly correct. We need to refer to the quantum theory for more detailed understanding of Rayleigh and Raman scattering.

3.3 Quantum Theory of Rayleigh and Raman Scattering

Our treatment is based on time-dependent perturbation theory. The first-order induced transition electric dipole moment is given by [6]:

$$(\vec{p}^{(1)})_{fi} = \langle \varphi_f^{(1)} | \hat{\vec{p}} | \varphi_i^{(0)} \rangle + \langle \varphi_f^{(0)} | \hat{\vec{p}} | \varphi_i^{(1)} \rangle, \tag{3.18}$$

where $\varphi_i^{(0)}$ and $\varphi_f^{(0)}$ are the unperturbed time-dependent wave functions of the initial state *i* and the final state *f*, $\varphi_i^{(1)}$ and $\varphi_f^{(1)}$ are the corresponding first-order perturbed time-dependent wave functions, and $\hat{\vec{p}}$ is the electric dipole moment operator.

To evaluate Eq. (3.18), we make the following assumptions: the perturbation is first order, the interaction Hamiltonian for the perturbation is entirely electric dipole in nature and the perturbation is produced by the time-dependent electric field associated with a plane monochromatic electromagnetic wave of frequency ω. Besides, due to the complex nature of Eq. (3.18), we rewrite it as:

$$(\vec{\tilde{p}}^{(1)})_{fi} = \langle \varphi_f^{(1)} | \hat{\vec{p}} | \varphi_i^{(0)} \rangle + \langle \varphi_f^{(0)} | \hat{\vec{p}} | \varphi_i^{(1)} \rangle, \tag{3.19}$$

and define the real induced transition electric dipole moment $(\vec{p}^{(1)})_{fi}$ as

$$(\vec{p}^{(1)})_{fi} = (\vec{\tilde{p}}^{(1)})_{fi} + (\vec{\tilde{p}}^{(1)})_{fi}^{*}, \tag{3.20}$$

where $(\vec{\tilde{p}}^{(1)})_{fi}^{*}$ is the complex conjugate of $(\vec{\tilde{p}}^{(1)})_{fi}$. This definition in Eq. (3.20) follows the way generally used in the literature and does not involve the factor 1/2.

Based on the assumptions we made, we can obtain the expression for the real induced transition electric dipole moment as:

$$(\vec{p}^{(1)})_{fi} = \frac{2\pi}{2h}\sum_{r\neq i}\{\frac{\langle\varphi_f|\hat{\vec{p}}_\rho|\varphi_r\rangle\langle\varphi_r|\hat{\vec{p}}_\sigma|\varphi_i\rangle}{\omega_{ri}-\omega-i\Gamma_{\mathrm{r}}}\tilde{E}_{\sigma 0}\exp\left[-i(\omega-\omega_{fi})t\right]$$

$$+\{\frac{\langle\varphi_f|\hat{\vec{p}}_\rho|\varphi_r\rangle\langle\varphi_r|\hat{\vec{p}}_\sigma|\varphi_i\rangle}{\omega_{ri}+\omega+i\Gamma_{\mathrm{r}}}\tilde{E}^*_{\sigma 0}\exp\left[i(\omega+\omega_{fi})t\right]\}$$

$$+\frac{2\pi}{2h}\sum_{r\neq f}\{\frac{\langle\varphi_f|\hat{\vec{p}}_\sigma|\varphi_r\rangle\langle\varphi_r|\hat{\vec{p}}_\rho|\varphi_i\rangle}{\omega_{rf}-\omega-i\Gamma_{\mathrm{r}}}\tilde{E}^*_{\sigma 0}\exp\left[i(\omega+\omega_{fi})t\right]$$

$$+\{\frac{\langle\varphi_f|\hat{\vec{p}}_\sigma|\varphi_r\rangle\langle\varphi_r|\hat{\vec{p}}_\rho|\varphi_i\rangle}{\omega_{rf}+\omega+i\Gamma_{\mathrm{r}}}\tilde{E}_{\sigma 0}\exp\left[-i(\omega-\omega_{fi})t\right]\}$$

$$+\,complex\ conjugate.$$

(3.21)

The wave functions φ_i, φ_f, φ_r are time-dependent unperturbed wave functions of the state *i*, *j* and *r*, respectively.

$$\varphi_r = \varphi_{r_0} exp\,[-i(\omega_r - i\Gamma_r)t], \tag{3.22}$$

where

$$\omega_r = \frac{2\pi E_r}{h}. \tag{3.23}$$

E_r is the energy (unit: J) of the state r, and $2\Gamma_{\mathrm{r}}$ (unit: rad/s) relates to the full width of the level r. For the initial and final states *i* and *f*, we assume their lifetimes are infinite so that $\Gamma_i = \Gamma_f = 0$. The double subscript on ω means a frequency difference such as:

$$\omega_{ri} = \omega_r - \omega_i. \tag{3.24}$$

$\hat{\vec{p}}_\rho$ and $\hat{\vec{p}}_\sigma$ are the ρ and σ components of the electric dipole moment operator. $\tilde{E}_{\sigma 0}$ is the σ component of the complex amplitude of the incident plane wave with frequency ω.

The terms in Eq. (3.21) contain two type of frequency dependence, namely frequency of $(\omega - \omega_{fi})$ and frequency of $(\omega + \omega_{fi})$. The terms involving $(\omega + \omega_{fi})$ describe induced emission of two quanta, $(\omega + \omega_{fi})$ and ω, from an initial state which is an excited level ω_i to a lower level ω_f. These will not be considered here.

If ω_{fi} is negative, which means the energy of final state is lower than the initial state, this is anti-Stokes Raman scattering. If ω_{fi} is zero, the final state has the same energy as the initial state and this is Rayleigh scattering. When ω_{fi} is greater than zero, the energy of final state is greater than the initial state, and this is Stokes Raman scattering.

Here we write Stokes and anti-Stokes Raman part of the ρ component of the real induced transition electric dipole moment as:

$$(p_\rho{}^{(1)})_{fi} = \frac{2\pi}{2h} \sum_{r \neq i,f} \left\{ \frac{\langle \varphi_f | \hat{\vec{p}}_\rho | \varphi_r \rangle \langle \varphi_r | \hat{\vec{p}}_\sigma | \varphi_i \rangle}{\omega_{ri} - \omega - i\Gamma_r} + \frac{\langle \varphi_f | \hat{\vec{p}}_\sigma | \varphi_r \rangle \langle \varphi_r | \hat{\vec{p}}_\rho | \varphi_i \rangle}{\omega_{rf} + \omega + i\Gamma_r} \right\} \tilde{E}_{\sigma 0}\, exp\left[-i(\omega - \omega_{fi})t\right] + complex\ conjugate. \tag{3.25}$$

We now introduce general transition polarizability $(\boldsymbol{\alpha})_{fi}$ with component $(\alpha_{\rho\sigma})_{fi}$ defined as:

$$(\alpha_{\rho\sigma})_{fi} = \frac{2\pi}{h} \sum_{r \neq i,f} \{ \frac{\langle f|\hat{\vec{p}}_\rho|r\rangle\langle r|\hat{\vec{p}}_\sigma|i\rangle}{\omega_{ri} - \omega - i\Gamma_r} + \frac{\langle f|\hat{\vec{p}}_\rho|r\rangle\langle r|\hat{\vec{p}}_\sigma|i\rangle}{\omega_{ri} + \omega + i\Gamma_r} \}. \tag{3.26}$$

Here $|i\rangle$ is the abbreviation for $|\varphi_i\rangle$, and so are $|f\rangle$ and $|r\rangle$.

The energy of the state *r*, in principle, can lie above the initial and final state, between the final and initial state, or below both final and initial states. However, we will conduct the discussion assuming that $|r\rangle$ is above $|i\rangle$ and $|f\rangle$ which is normally the case.

When the frequency of the exciting radiation ω is much lower than any absorption frequency ω_{ri} of the molecule, then $\omega_{ri} - \omega \approx \omega_{ri}$ for all states $|r\rangle$ and $i\Gamma_r$ can be neglected because it is small relative to ω_{ri}. Another case is when ω is close to one or more absorption frequencies ω_{ri} of the molecule, then $\omega_{ri} - \omega - i\Gamma_r \approx -i\Gamma_r$ for a particular state $|r\rangle$. Terms with such denominators will dominate in the sum over r.

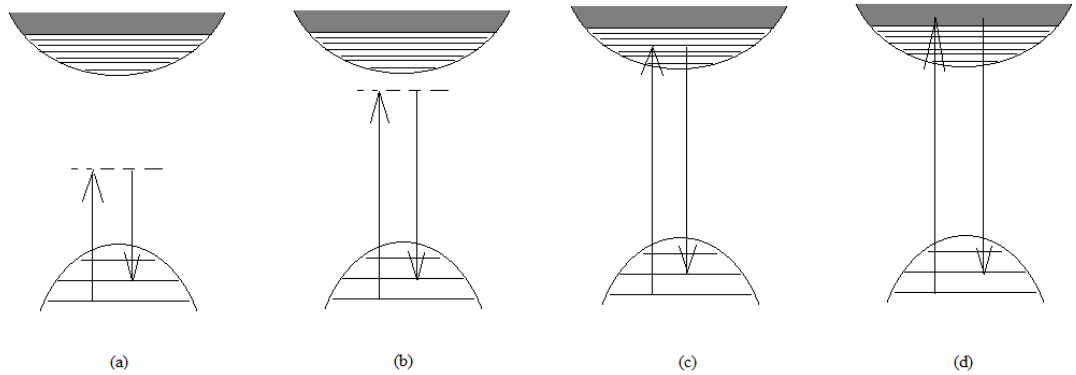

Figure 3-1: Four types of Raman scattering: (a) normal (b) pre-resonance (c) discrete resonance (d) continuum resonance Raman scattering.

When $\omega \ll \omega_{ri}$, the Raman scattering is illustrated by the energy level diagram in Figure 3-1 (a). The molecule interacts with the incident photon and makes a transition to

a virtual state $|r\rangle$ as illustrated by a broken line in Figure 3-1 (a). The virtual state is not a stationary state of the system and is not a solution of a time-dependent Schrödinger equation. This process of absorption without energy conservation is called virtual absorption.

As ω approaches a molecular transition frequency ω_{ri} the Raman scattering is illustrated by Figure 3-1 (b). When $\omega \approx \omega_{ri}$, the Raman process is illustrated in Figure 3-1 (c) and is called discrete resonance Raman scattering. If ω is large enough to reach the continuum energy level of the system, the Raman process is illustrated in Figure 3-1 (d) and is termed continuum resonance Raman scattering.

As we discussed, when certain frequency conditions can be satisfied $i\Gamma_r$ can be neglected, and eq. (3.26) becomes:

$$(\alpha_{\rho\sigma})_{fi} = \frac{2\pi}{h} \sum_{r \neq i,f} \{ \frac{\langle f|\hat{\tilde{p}}_\rho|r\rangle\langle r|\hat{\tilde{p}}_\sigma|i\rangle}{\omega_{ri} - \omega} + \frac{\langle f|\hat{\tilde{p}}_\sigma|r\rangle\langle r|\hat{\tilde{p}}_\rho|i\rangle}{\omega_{ri} + \omega} \}. \tag{3.27}$$

Using this real transition polarizability, we obtain:

$$(p_\rho{}^{(1)})_{fi} = \frac{1}{2}(\alpha_{\rho\sigma})_{fi}[\tilde{E}_{\sigma 0}(\omega)\exp(-\mathrm{i}\omega_s t) + \tilde{E}^*_{\sigma 0}(\omega)\exp(\mathrm{i}\omega_s t)], \tag{3.28}$$

where

$$\omega_s = \omega - \omega_{fi}. \tag{3.29}$$

Eq. (3.28) can be further rewritten as:

$$(p_\rho{}^{(1)})_{fi} = \frac{1}{2}\{(\tilde{p}_{\rho 0}{}^{(1)})_{fi}\exp(-\mathrm{i}\omega_s t) + (\tilde{p}_{\rho 0}{}^{(1)})^*_{fi}\exp(\mathrm{i}\omega_s t)], \tag{3.30}$$

where

$$(\tilde{p}_{\rho 0}{}^{(1)})_{fi} = (\alpha_{\rho\sigma})_{fi}\tilde{E}_{\sigma 0}(\omega), \tag{3.31}$$

$$(\tilde{p}_{\rho 0}{}^{(1)})^{*}_{fi} = (\alpha_{\rho\sigma})_{fi}\tilde{E}^{*}_{\sigma 0}(\omega). \quad (3.32)$$

When the electric field amplitude is real, $\tilde{E}_{\sigma 0}(\omega) = \tilde{E}^{*}_{\sigma 0}(\omega) = E_{\sigma 0}(\omega)$, then $(\tilde{p}_{\rho 0}{}^{(1)})_{fi} = (\tilde{p}_{\rho 0}{}^{(1)})^{*}_{fi} = (p_{\rho 0}{}^{(1)})_{fi}$ and eq. (3.30) becomes:

$$(p_{\rho}{}^{(1)})_{fi} = \frac{1}{2}(p_{\rho 0}{}^{(1)})_{fi}[\exp(-\mathrm{i}\omega_s t) + \exp(\mathrm{i}\omega_s t)], \quad (3.33)$$

where

$$(p_{\rho 0}{}^{(1)})_{fi} = (\alpha_{\rho\sigma})_{fi}\, E_{\sigma 0}(\omega). \quad (3.34)$$

These results from quantum theory are similar to those obtained from classical theory, but oscillating electric dipole and polarizability in classical theory are replaced with transition electric dipole and polarizability. Besides, the transition polarizability is defined in terms of the wave functions and energy levels of the system which make it possible to associate the characteristics of scattering with the properties of the scattering molecules as we discussed in Figure 3-1.

3.4 Raman Instrumentation

In this section, I will introduce the instrumentation on which the Raman and Rayleigh measurements in this thesis were performed.

3.4.1 Horiba Jobin Yvon T64000 Raman System

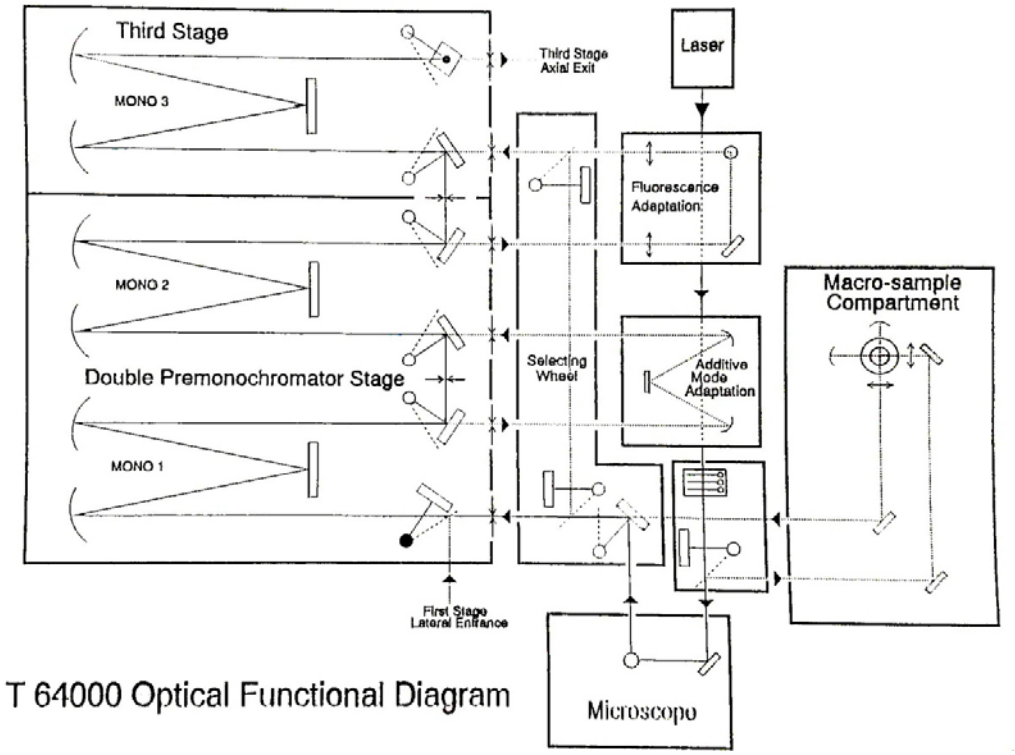

Figure 3-2: a schematic diagram of Horiba Jobin Yvon T64000 spectrometer internal optics [7].

Figure 3-2 is an overall T64000 spectrometer functional diagram [7], and it shows the optical path for macro- and micro-Raman as well as the different modes of operations. These modes include: (1) single spectrograph; (2) double subtractive; (3) triple additive mode. The single spectrograph mode uses only the third stage monochromator and can get the highest optical throughput on weak scattering samples. The double subtractive mode is used for the measurement of low frequency band close to the laser line. Ultra high spectral resolution ($<0.15 cm^{-1}$) can be obtained by use of the

triple additive mode. The ray diagrams for double subtractive and triple additive mode are illustrated in Figure 3-3.

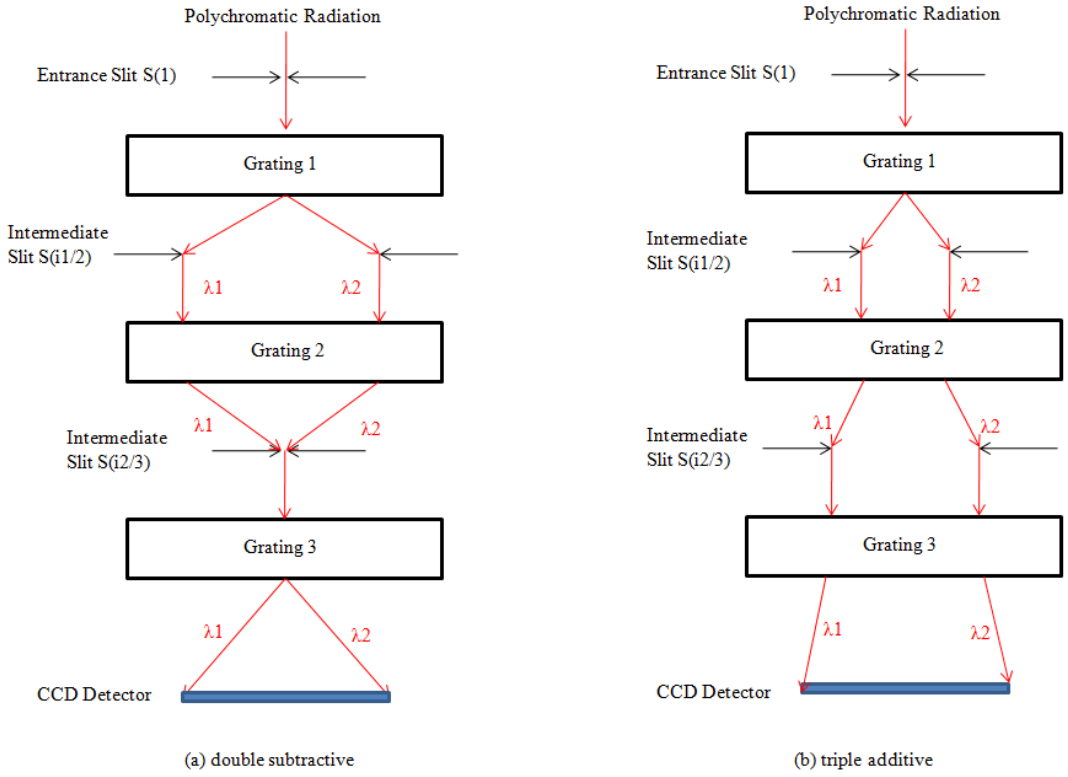

Figure 3-3: optical diagram for (a) double subtractive (b) triple additive mode in Horiba Jobin Yvon T64000 spectrometer [7].

The single spectrograph mode in Horiba Jobin Yvon T64000 spectrometer was used for the studying acoustic modes in $Si_{1-x}Ge_x$ alloy nanowires (Chapter 4).

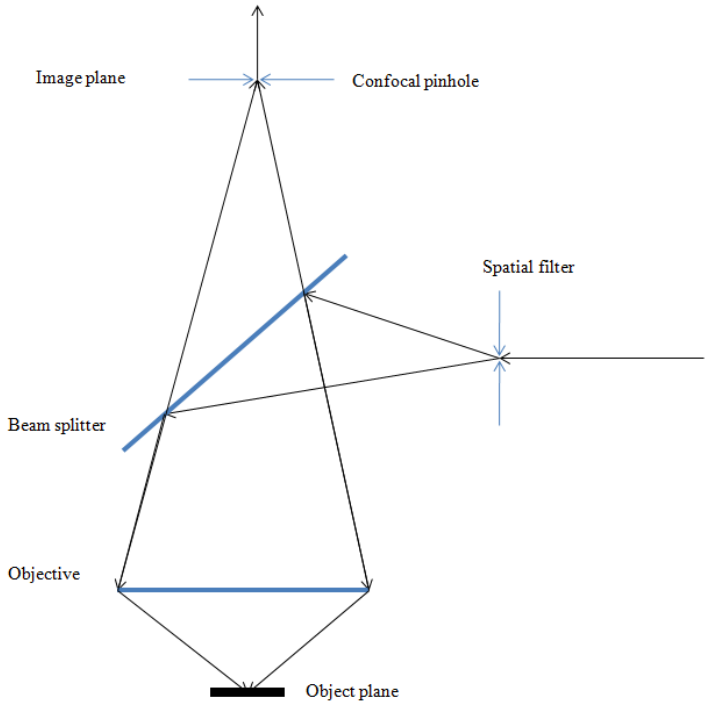

Figure 3-4: Optical diagram of confocal microscope [7].

This spectrometer was equipped with an Olympus BX40 confocal microscope system. A confocal microscope consists of two spatial filters as illustrated in Figure 3-4. The first filter is placed on the incident laser beam to purify the laser, and the second filter is placed right on the image plane of the microscope to limit the analyzed surface of the sample as well as the depth focus. Therefore, by adjusting the size of the pinhole at the image plane, we are able to collect scattering only from the illuminated part of a sample.

3.4.2 Renishaw InVia Micro-Raman System

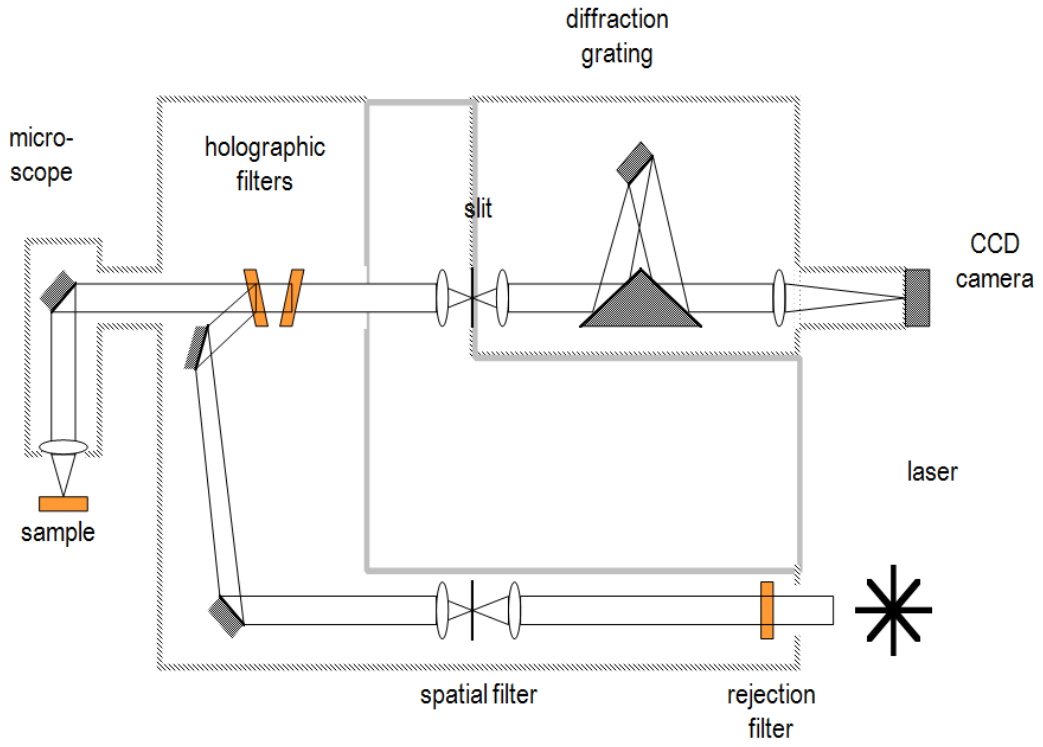

Figure 3-5: A schematic diagram of Renishaw InVia Micro-Raman System internal optics [8].

Figure 3-5 illustrates the optical diagram in a Renishaw InVia Micro-Raman system [8]. The incident laser beam originates from the right bottom corner, going through a spatial filter as the first spatial filter we discussed in Figure 3-4. The slit at the center of Figure 3-5 serves as the pinhole in Figure 3-4, and thus makes the whole system a confocal Raman system. Figure 3-6 shows how a linear slit and a CCD eliminate the need of a square or round pinhole in a confocal system. The use of a slit also has an advantage in optical alignment before taking any measurement in the confocal system.

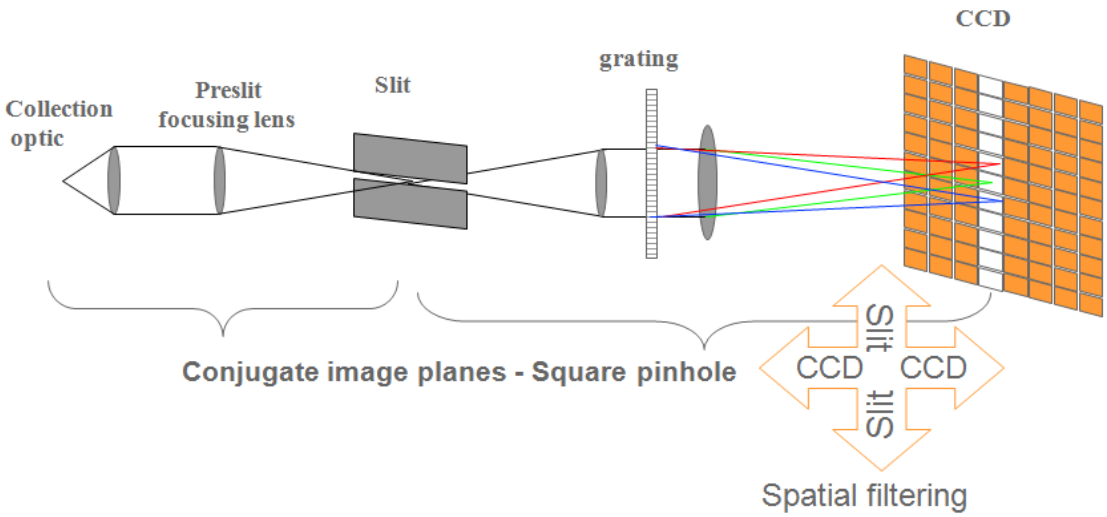

Figure 3-6: Optical diagram of confocal Raman microscopy without pinhole optics [8].

The microscope in Figure 3-5 can accommodate one additional optical component at a time, such as a half wave plate. The sample under the microscope is placed on a rotational stage and this rotational stage is mounted on a computer-controlled XYZ stage. All the details for this microscope and stage are given in Chapter 6 and Chapter 7.

Chapter 4

Raman Scattering from $Si_{1-x}Ge_x$ Alloy Nanowires

4.1 Introduction

Semiconductor alloy nanowires have attracted increasing interest for bandgap tunable electronic devices [9,10]. Si-Ge represents an example of such a system, even though it has an indirect bandgap. Studies of $Si_{1-x}Ge_x$ bulk material over the range $0 \leq x \leq 1$ reveal continuous bandgap tunability from 0.7eV to 1.1eV [11] and they may provide an opportunity for nanoscale electronic and optoelectronic devices. This binary system is also suitable for optical fiber communication [12,13].

Electrical transport in nanowires is influenced by phonon scattering and Raman scattering provides an important probe of the phonon properties of $Si_{1-x}Ge_x$ nanowires and their crystalline quality. The phonon properties of bulk Si and Ge [14], SiGe mixed crystals [15,16], Si/Ge superlattices [17,18] and $Si_{1-x}Ge_x$ nanoparticles [19,20] and films [20] have been studied via Raman scattering [21,22,23]. To the best of our knowledge, no Raman results had been reported on $Si_{1-x}Ge_x$ alloy nanowires when this work was published in 2008.

Here, I discuss the results of such studies on $Si_{1-x}Ge_x$ alloy nanowires and our experimental results will be compared to recent theoretical calculations [19] and previously published results for crystalline bulk $Si_{1-x}Ge_x$ samples and thin films [20].

4.2 Experimental Details

$Si_{1-x}Ge_x$ NWs were grown by the VLS mechanism using CVD as discussed in Chapter 2.2. Scanning electron microscopy (SEM, Philips XL20) was used for plan-view imaging of the $Si_{1-x}Ge_x$ nanowires showing the length of the nanowires in the range of 15 - 40 microns. Structural and chemical characterization of the NWs were carried out using a JEOL 2010F field-emission TEM/STEM equipped with an X-ray energy dispersive spectroscopy (EDS) system for elemental analysis. Chemical compositions of $Si_{1-x}Ge_x$ nanowires were quantified from the EDS data by the ζ method [24]. The ζ factor, absorption corrections, and K-factors of Si and Ge K_α lines were calibrated using a standard SiGe thin film sample. The minimum detectable limit of Ge in Si was measured to be 0.8 at.%. For TEM characterization, $Si_{1-x}Ge_x$ nanowires were released from the substrate surface by sonication and then suspended in semiconductor-grade isopropanol. A drop of the nanowire suspension was then placed onto a lacey carbon coated copper grid for TEM observation.

Figure 4-1 (a) shows a low-magnification bright-field TEM image of the $Si_{1-x}Ge_x$ nanowires. The Au nanoparticle responsible for the VLS growth can be observed with darker contrast at the tip of the wires. The crystalline growth direction of the nanowires was mostly <111>. Inset in Figure 4-1 (a) shows the selected area electron diffraction (SAD) pattern from an individual nanowire, this pattern is consistent with the reciprocal lattice of the diamond structure observed along the $[\bar{1}12]$ zone axis; the corresponding nanowire growth direction (white arrow) is also indicated. Nevertheless, other growth directions were also found, as shown in the inset of Figure 4-1 (b). The HRTEM image in

Figure 4-1 (b) shows the crystalline nature of these nanowires; the lattice fringes corresponding to the [111] crystalline direction can be easily observed. A uniform amorphous oxide coating of about 3 nm thick was typically observed on the outer surface of the $Si_{1-x}Ge_x$ nanowires. The Ge concentration in the outer oxide layer was very small; i.e., the layer was found to be essentially silicon oxide by EDS. Many TEM images similar to Figure 4-1 (a) were used to estimate the diameter distribution of these nanowires. Typical nanowires exhibit a reasonably uniform diameter along the entire length, i.e., without tapering. We could also observe a small modulation in the nanowire diameter along the length, as we have reported in other VLS nanowire systems [25,26]. This modulation was not studied here. However, in polar semiconductors, e.g., GaP, ZnO, etc., the modulation has been proposed to activate Raman scattering from surface optic (SO) modes that lie between the transverse optic (TO) and longitudinal optic (LO) modes.

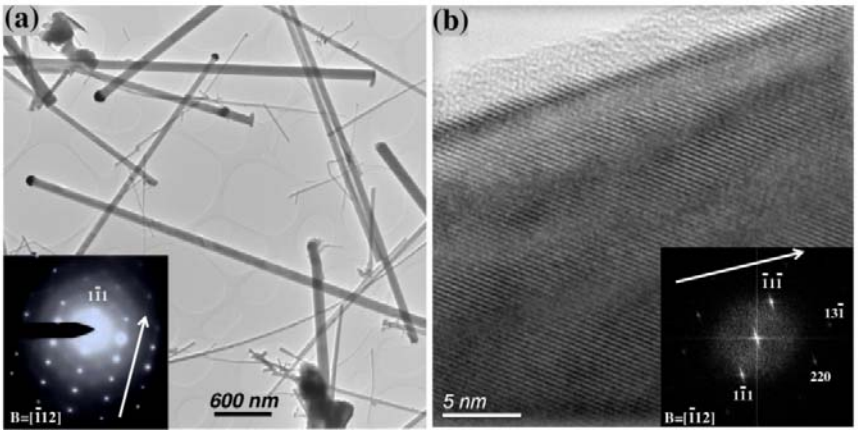

Figure 4-1: (a) Low magnification bright-field TEM image of the $Si_{1-x}Ge_x$ nanowires, the inset shows a SAD pattern from an individual nanowire with growth direction along the [111]. (b) High-resolution TEM image showing the crystalline nature of the $Si_{1-x}Ge_x$ nanowires, the inset is the corresponding Fourier Transform and the white arrow indicates the growth direction ([$13\bar{1}$]) of this particular nanowire. Most nanowires were observed to grow in the [111] direction.

Sample	T (ºC)	Substrate	MP Diameter (nm)	Ge (at.%)
1	325	Si	88 ± 1	95±0.2
2	325	Si	85 ±1	84±1.6
3	400	Al_2O_3	107 ± 1	61±2.8
4	375	Al_2O_3	101 ±1	61±3.0
5	400	Al_2O_3	107 ± 1	42±3.3
6	425	Si	81 ± 1	31±2.7
7	500	Si	76 ± 1	12±1.1

Table 4-1: Summary of $Si_{1-x}Ge_x$ nanowire growth conditions, most probable (MP) diameter and Ge at.%.

Table 4-1 summarizes the growth conditions and composition (x) for seven batches of $Si_{1-x}Ge_x$ nanowire samples studied in the present work. Within each batch, the diameter distribution of the nanowires is reasonably broad, i.e., from 20 nm to 160 nm. A typical diameter distribution is shown in Figure 4-2.

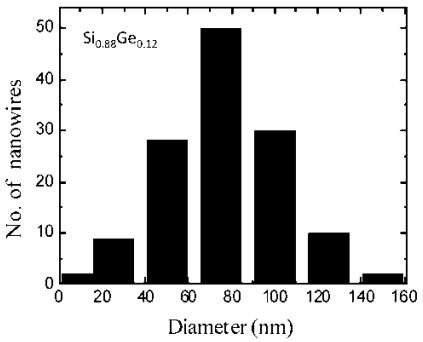

Figure 4-2: Diameter distribution for $Si_{0.88}Ge_{0.12}$ nanowires. This distribution is typical of all the samples studied here.

The compositional homogeneity along the length of our nanowires was studied by EDS. The Si/Ge ratio was found to be homogeneous along the nanowire to better than 1at.%. It was found that smaller diameter nanowires from the same batch showed a small decrease of the Ge concentration (e.g. when d<50nm) [27]. For each batch, we averaged the Ge concentration in 10 nanowires, all of which had a diameter very near to the most probable diameter (~90-100nm) of the batch (c.f. Table 4-1).

4.3 Results and Discussions

Ge% (x)	Peak Position					
	TA Band (cm^{-1})	Ge-Ge (cm^{-1})	Si-Ge (cm^{-1})	Weak Peak (cm^{-1})	Shoulder (cm^{-1})	Si-Si (cm^{-1})
0.12	107		401	433	489	510
0.31	93	290	404	428, 451	478	497
0.42	97	282	396	423, 451	474	489
0.61	87	281	395	421, 443	459	472
0.61	87	281	390	430		457
0.84	84	295	391			450
0.95	81	299	387			

Table 4-2: Experimental Raman band positions for $Si_{1-x}Ge_x$ nanowires. Data collected with 514.5 nm excitation at room temperature.

Micro-Raman spectra were collected at room temperature on the seven batches of $Si_{1-x}Ge_x$ alloy nanowire samples using a Renishaw Invia Micro-Raman Spectrometer and 514.5 nm laser excitation. The spectrometer was calibrated with Hg lines and returned the value of 520 cm^{-1} for the LO-TO mode of Si at q = 0 cm^{-1}, in agreement with experiments on the bulk. For all Raman spectra, the power of the laser was measured to be ~ 0.7 mW

with a hand-held radiometer at the sample. The nanowires were studied on the growth substrate. Hundreds of nanowires were estimated to be illuminated within the 1 μm spot size created by the objective lens (100x). In Si nanowires, it has been shown that phonon confinement distortion of the otherwise Lorentzian LO-TO Raman band occurs for $d \leq 10$ nm [28]. The present SiGe nanowires are too large in diameter ($20 \leq d \leq 100$ nm) to exhibit phonon confinement. Although the spectra were collected under identical optical conditions, the absolute intensity scales for each spectrum shown in Figure 4-3 through Figure 4-6 should not be compared, since different numbers of wires were sampled in each spectrum.

In Figure 4-3 we show the Raman spectra collected for the seven Si_xGe_{1-x} nanowire samples summarized in Table 4-1. The nanowires were dense enough on the substrate that the Raman spectra do not exhibit the sharp band at 520 cm^{-1} from the underlying Si (111) substrate. Each Raman spectrum is therefore the collective response of many nanowires, representing the average x listed in Table 4-1. Three prominent Raman bands can be observed in the figure whose intensity and position depend on x. The lowest frequency band is located near ~300 cm^{-1} and is close in frequency to the q = 0 LO-TO phonon mode in pure Ge. It is therefore called the Ge-Ge band in the literature (q is the wavevector of the phonon; the Raman selection rule in periodic systems requires that only q = 0 phonons are observed). The highest frequency band in Figure 4-3 occurs near 500 cm^{-1} and is close in frequency to the q = 0 LO-TO phonon mode in pure Si. Therefore, it is called the Si-Si band. The Raman band in the middle of the spectrum ~ 400 cm^{-1} is called the Si-Ge band. Theory has shown that the ~ 400 cm^{-1} band is a local mode resulting from the vibration of Si atoms surrounded by 2 or more Ge atoms [19].

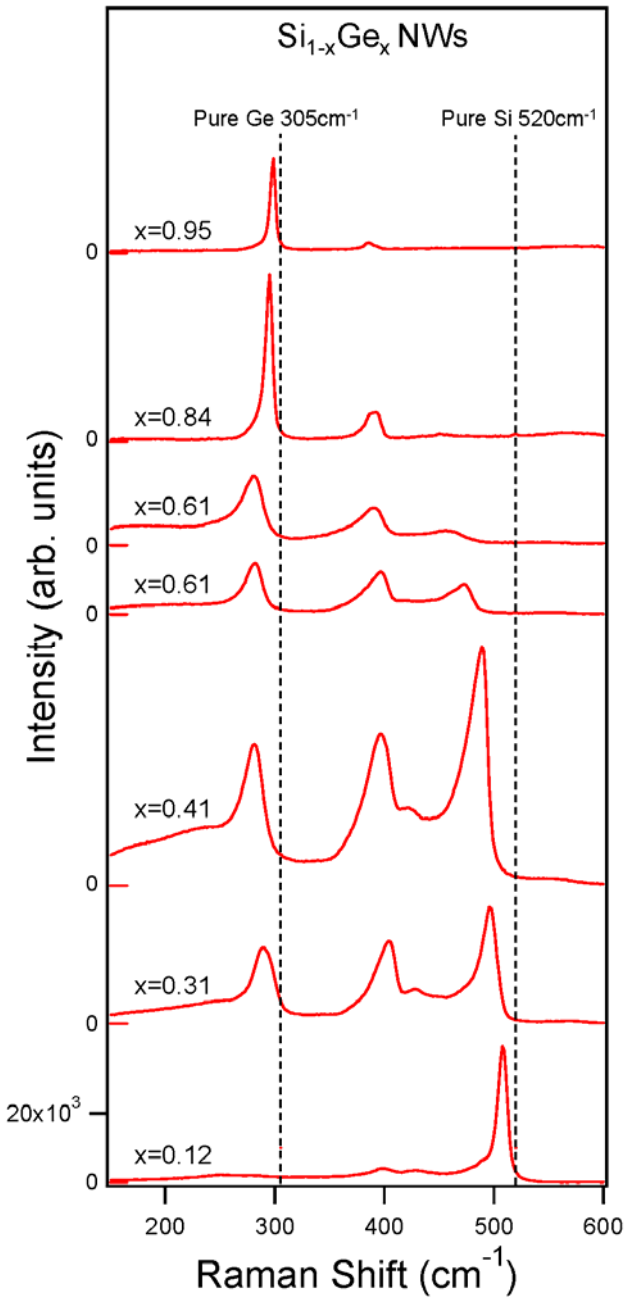

Figure 4-3: Micro-Raman spectra from seven batches of crystalline $Si_{1-x}Ge_x$ alloy nanowires collected at room temperature with 514.5 nm excitation. The spectra were collected from wires remaining on the growth substrate and contain contributions from ~ 100 nanowires with random orientation relative to the incident polarization. Three prominent bands are observed and are referred to in the text and Table 4-2 as: (1) the Ge-Ge band (~ 300 cm^{-1}); (2) the Si-Ge band (~ 400 cm^{-1}); and (3) the Si-Si band (~ 500 cm^{-1}). The dashed vertical lines refer to the position of the q = 0 LO-TO Raman band in pure crystalline Ge and Si.

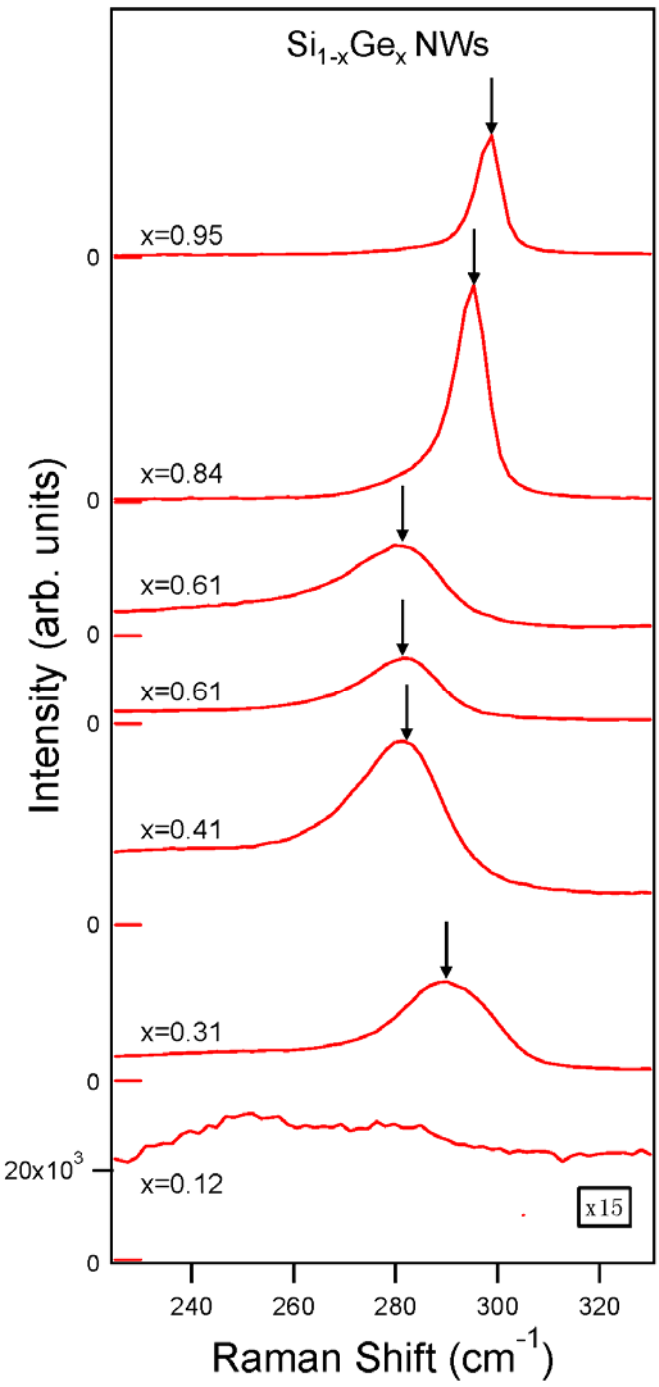

Figure 4-4: Micro-Raman spectra (225 - 330 cm^{-1}) for $Si_{1-x}Ge_x$ alloy nanowires. The arrows indicate the Ge-Ge band position as listed in Table 4-2. The number in the box to the right of each spectrum refers to the scale factor used to multiply spectra appearing in Figure 4-3. Spectra were collected at room temperature using 514.5 nm excitation.

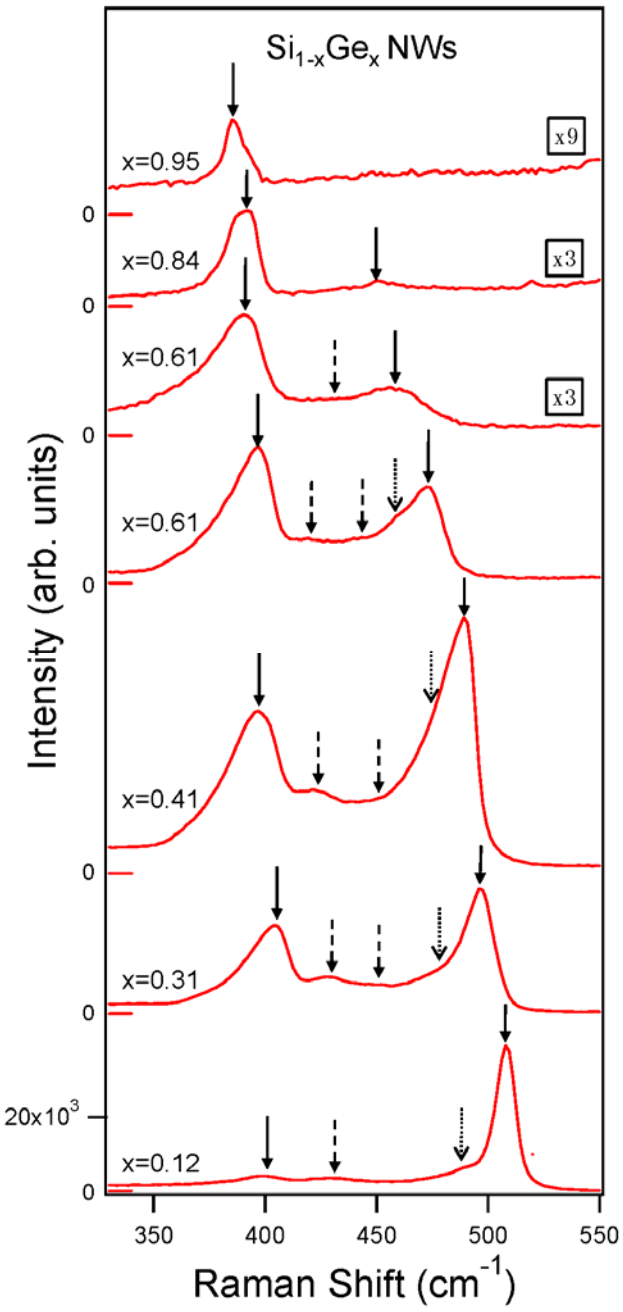

Figure 4-5: Micro-Raman spectra (330 - 550 cm^{-1}) for $Si_{1-x}Ge_x$ alloy nanowires collected by a Renishaw Invia Micro-Raman Spectrometer. The solid and dashed arrows refer, respectively, to strong and weak bands. The dotted arrows indicate the position of a shoulder (unresolved band) on the low frequency side of the Si-Si band. Their positions are listed in Table 4-2. The number in the box to the right of each spectrum refers to the scale factor used to multiply spectra appearing in Figure 4-3. Spectra collected at room temperature using 514.5 nm excitation.

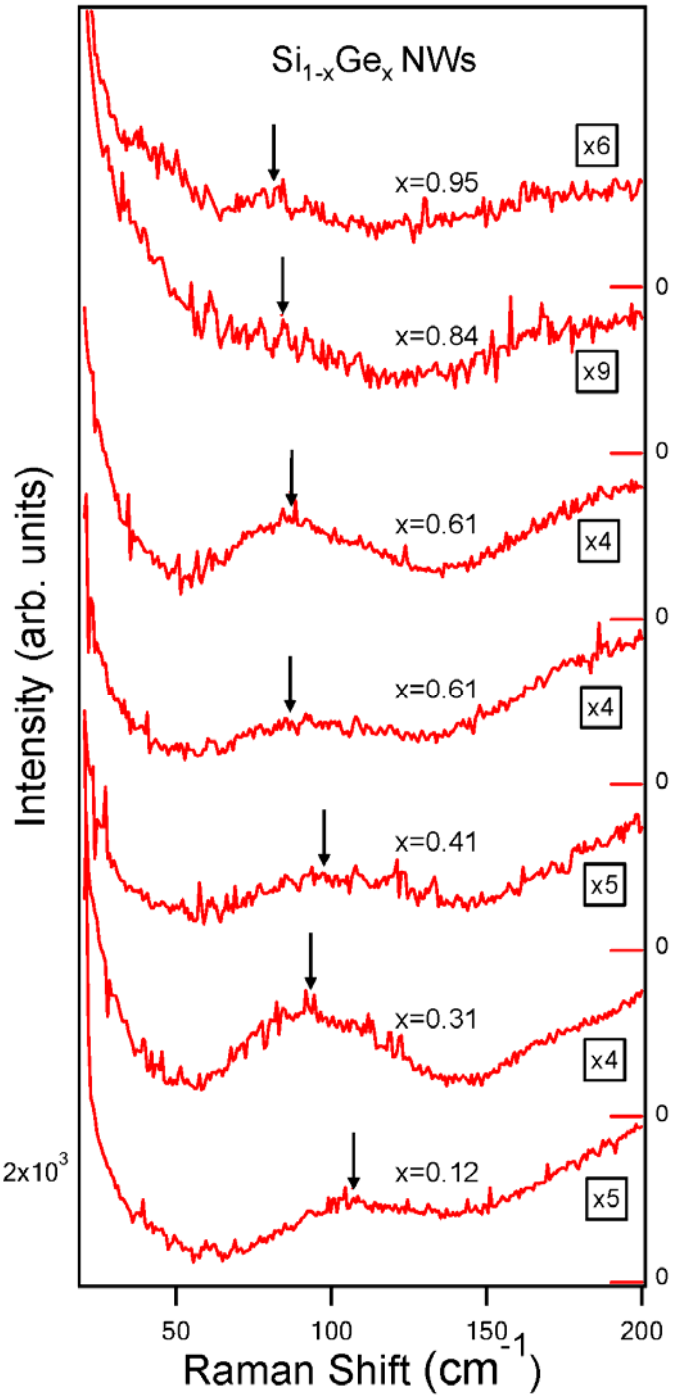

Figure 4-6: Low frequency Micro-Raman spectra (20 – 200 cm^{-1}) for crystalline $Si_{1-x}Ge_x$ alloy nanowires. The solid arrows indicate the band maximum as obtained from a Lorentzian fit. The band is identified with a TA band, c.f., Table 4-2. The number in the box is the relative scale factor used to expand the raw spectrum. Spectra were collected at room temperature using 514.5 nm excitation.

Figure 4-3 shows that the Si-Si band position is the most sensitive to the Ge concentration (x) and downshifts rapidly with increasing x. The peak position can therefore be valuable for estimating x by Raman scattering. The behavior of the Ge-Ge band, on the other hand, is a little more complicated. For clarity, we divide the spectra in Figure 4-3 into low and high frequency regions: 225 - 330 cm^{-1} (Figure 4-4) and 330 – 550 cm^{-1} (Figure 4-5). As shown in Figure 4-4, the Ge-Ge band first downshifts slightly with increasing x to its lowest frequency where the ratio Si/Ge ~ 1, and then upshifts. This behavior is more evident in a plot of the Ge-Ge band position vs. x, as discussed below. Figure 4-5 reveals more details about Raman spectra in the high frequency (330 – 550 cm^{-1}) region. It shows that in addition to the Si-Ge and Si-Si band, there are one or two weak features between 420 – 455 cm^{-1} and also a shoulder at the low frequency side of the Si-Si band. The weak peaks (dashed arrows) appear for x = 0.12 ~ 0.61 and become harder to resolve for $x \geq 0.84$. The shoulder (dotted arrows) to the low frequency side of the Si-Si band can be recognized for x = 0.12 ~ 0.61. The nanowire Raman peak features will be compared to their counterparts in SiGe alloy bulk and liquid-phase-epitaxy (LPE) films.

The structure in the Raman spectra for $Si_{1-x}Ge_x$ shown in Figure 4-3 is strongly correlated with the calculated vibrational density of states (VDOS) by Yu and co-workers [19]. In Figure 4-7 we show their theoretical VDOS for crystalline $Si_{1-x}Ge_x$ nanoparticles. They used a valence force field model for a nearly spherical particle containing 1147 atoms (~ 3.5 nm) and the "mass-difference-only" approximation for the lattice dynamics. In the mass-difference-only model, a universal set of stretching and bending force constants are used for Si-Si, Ge-Ge and Si-Ge bonds to calculate the normal vibrational

modes of the particle. In this approximation, their model yields 502 cm^{-1} for the Si-Si peak in a Si nanoparticle, whereas 520 cm^{-1} is the experimental result for the q = 0 optical phonon in bulk Si. Therefore, their universal force constants are a little soft. We therefore expect their calculated frequencies to be ~10 - 20cm^{-1} lower than experiment, particularly for the higher frequency Si-Si modes.

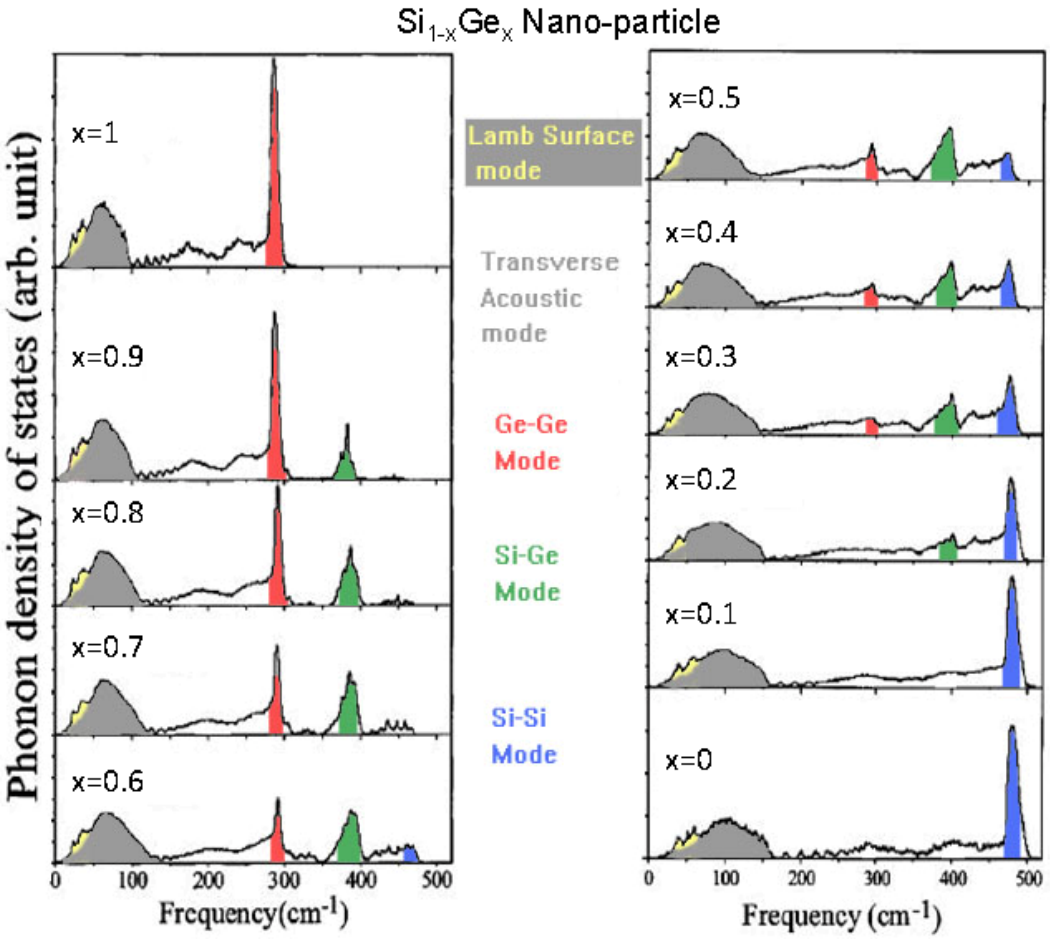

Figure 4-7: Vibrational density of states (VDOS) calculated for $Si_{1-x}Ge_x$ nanoparticles using the "mass difference only" approximation for the lattice dynamics [19]. Color coding added to aid in the band identification.

As indicated schematically by the color code in Figure 4-7 for their calculated VDOS, they find a broad VDOS band centered near ~ 75 – 100 cm^{-1} that they have identified with nanoparticle modes analogous to the transverse acoustic (TA) modes in the infinite solid. This TA VDOS band upshifts with decreasing x as the heavier Ge atoms are replaced by the lighter Si atoms. The sharp peaks on the low frequency side of the TA VDOS band are surface modes. Experimental difficulties (stray light rejection) prevented us from collecting the Raman spectrum below ~ 100 cm^{-1} from the Renishaw Invia Micro-Raman spectrometer. We therefore used a Jobin-Yvon T64000 Raman triple grating spectrometer for spectra below 100 cm^{-1}. The results are shown in Figure 4-6. The TA band shows an overall trend to downshift as x increases. However, compared to the calculated TA VDOS band, the experimental downshift (~ 30 cm^{-1}) is lower than their predicted value (~ 50 cm^{-1}). The higher frequency theoretical VDOS bands associated with the Ge-Ge, Si-Ge and Si-Si modes were easily observed by the Renishaw Invia Micro-Raman Spectrometer. Figure 4-8 shows a detailed comparison between our Raman spectrum for $Si_{0.69}Ge_{0.31}$ nanowires and the VDOS for $Si_{0.7}Ge_{0.3}$ nanoparticles calculated by Yu and co-workers [19]. The agreement between our Raman spectra and the calculated VDOS is very good. This suggests that the Raman scattering matrix element is not a strong function of mode frequency. Recall that the theoretical calculation involves only the VDOS and does not include the Raman matrix element. As we have discussed, the force constants used in the calculations are slightly soft and we do observe a 20 – 30 cm^{-1} difference between theory and experiment for the highest frequency Si-Si band. It is also noteworthy that several of the weaker calculated VDOS features, such as the small peaks labeled (A, B) and a shoulder labeled C in Figure 4-8, are reproduced in our Raman

spectrum. However, a small peak predicted at ~ 340 cm^{-1} in the calculated VDOS does not appear in the Raman spectrum. This might be explained by the fact that: (1) the 340 cm^{-1} VDOS feature was assigned theoretically to Si-Si surface modes [19]; and (2) our nanowires are coated with a thin oxide layer which might eliminate or suppress the activity of surface modes.

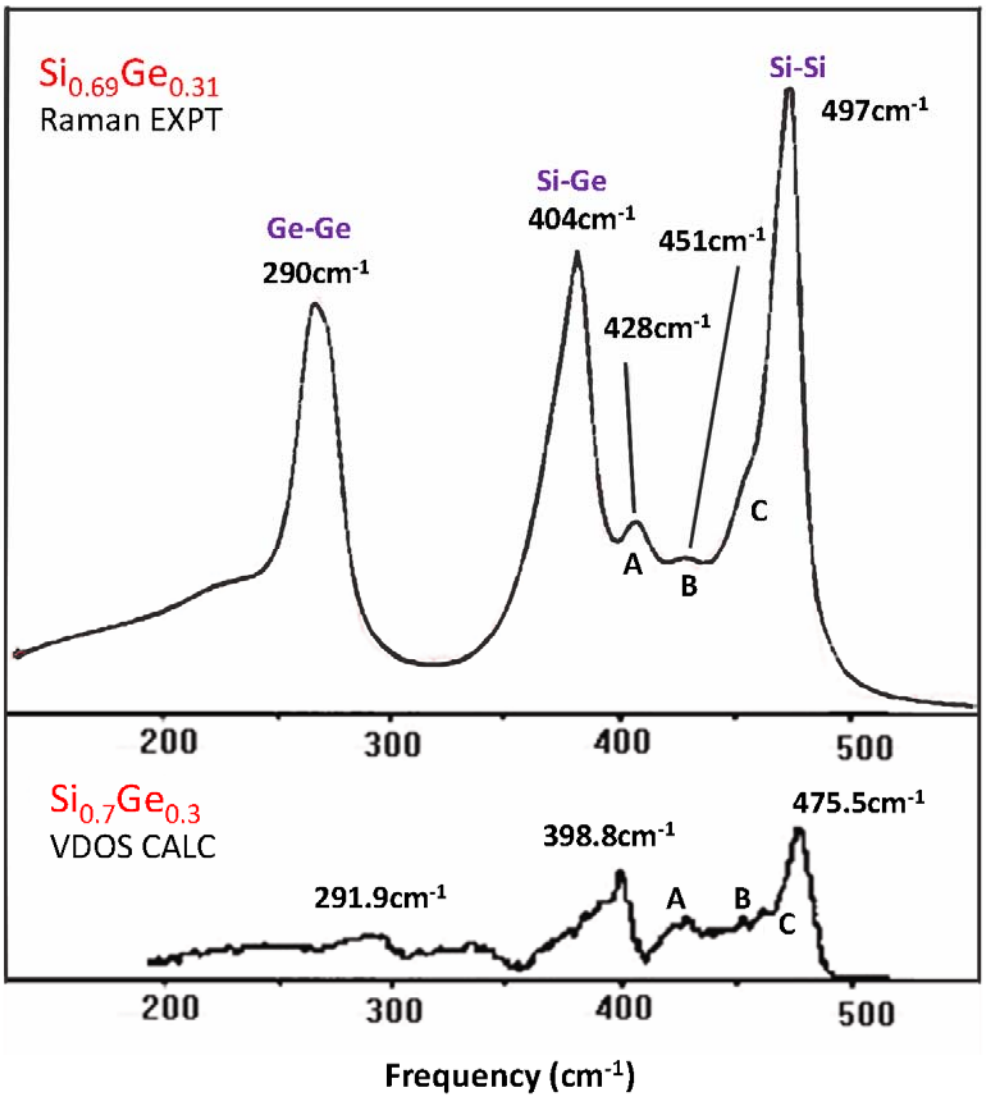

Figure 4-8: Comparison of the experimental Raman spectrum for $Si_{0.7}Ge_{0.3}$ to the calculated VDOS [19].

A noteworthy point here is that the computed VDOS from a spherical nanoparticle containing 1147 atoms should represent a Raman profile of a comparable size $Si_{1-x}Ge_x$ nanowire. Since the size of the nanoparticle used in computation is about 13 atoms and 3.5nm in diameter which means lack of translational symmetry, we expect our Raman spectra from our 70 – 100 nm diameter nanowires to have sharper and more symmetric peaks than the peaks in the computed VDOS. The fact that our Raman peaks show asymmetric features indicates that: (1) in most of the $Si_{1-x}Ge_x$ alloy nanowires, there is no long range translational symmetry, and this can be proved by increasing asymmetry in Si-Si peaks as the Ge concentration increases (Figure 4-5); (2) the asymmetric features in Si-Ge peaks come from the mixture of modes in Si-2Ge2Si, Si-3Ge1Si and Si-4Ge [19]; (3) the nanowires might be heated from the laser and thus Raman peaks become broad, downshifted and asymmetric.

To further compare experiment and theory for the vibrational modes of $Si_{1-x}Ge_x$, we compare the frequency of the Raman and VDOS band maxima vs. x in Figure 4-9 (a). For the Si-Si band, both theory and experiment exhibit a softening with increasing x; both also exhibit a dip although the theory predicts a deeper dip and at higher x. The offset in frequency between the position of the Raman band and VDOS band (Si-Si) is partially due to the slightly soft theoretical force constants. However, our experimental nanowire results are also slightly lower in frequency than obtained in bulk solids and films (we discuss this below). A small but interesting discrepancy in the experimental nanowire and theoretical behavior of the Ge-Ge band is also evident in Figure 4-9 (a). Our data exhibit a shallow minimum near x~0.5 which is not seen in the calculated VDOS behavior or in

the bulk Raman spectra, Figure 4-9 (b). On the other hand, experiment and theory are in very good agreement regarding the x-dependence of the Si-Ge local modes near 400 cm^{-1}.

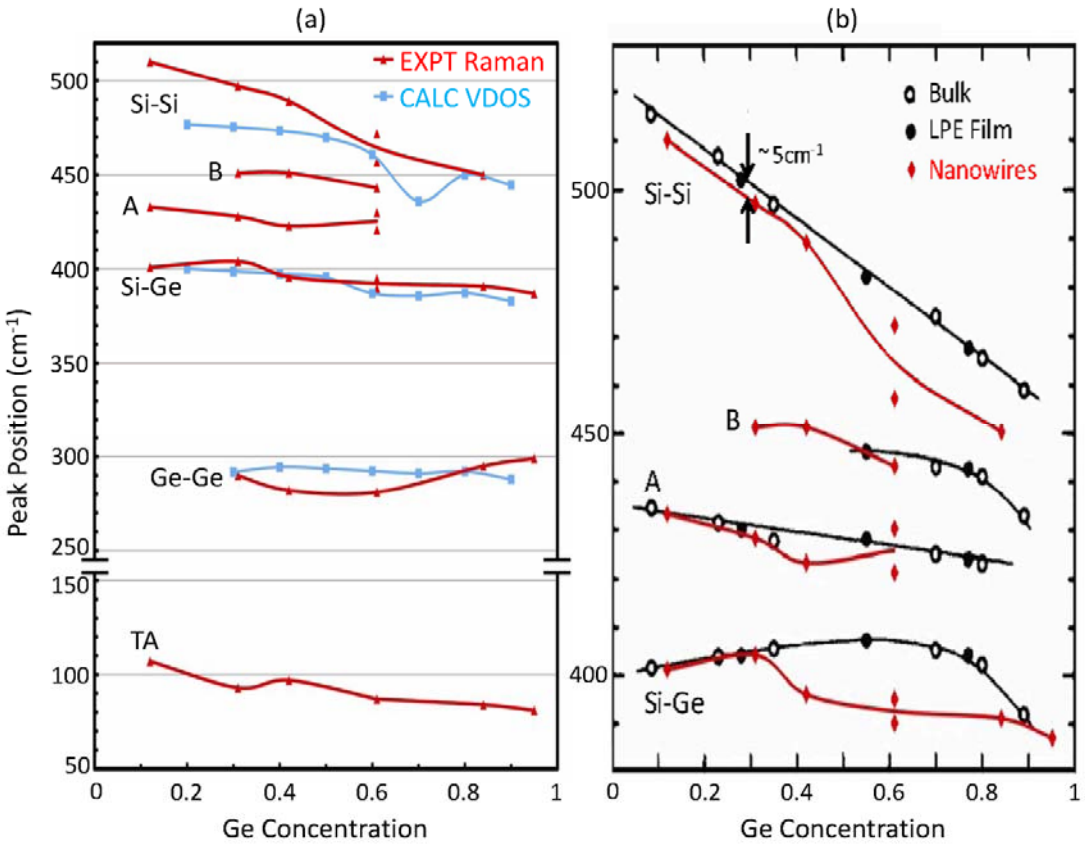

Figure 4-9: Comparison of our experimental Raman band maxima for $Si_{1-x}Ge_x$ nanowires to (a) VDOS band maxima calculated for nanoparticles in Ref. [19]; and to (b) experimental Raman peak positions (excluding shoulders) for $Si_{1-x}Ge_x$ bulk and LPE films as reported in Ref. [20].

In Figure 4-9 (b), we compare our experimental Raman results in $Si_{1-x}Ge_x$ nanowires to previous Raman results for $Si_{1-x}Ge_x$ bulk material and bulk thin film samples prepared by liquid-phase-epitaxy (LPE) [20]. We observe some interesting differences in the x behavior of the various Raman bands. For the Si-Si band, both the

nanowire, the bulk and the LPE film samples exhibit an initial linear softening of the band frequency with increasing x. Unlike the nanowires, the experimental bulk and LPE film Si-Si band exhibits this linear behavior over the entire range of composition. Furthermore, for $x<0.5$, the Si-Si band frequencies for the nanowires exhibit a rigid downshift by ~5 cm^{-1} relative to the data for bulk and for LPE film samples. Since the Ge-Ge, Si-Ge and Si-Si band position data from the bulk (open diamonds) and LPE films (closed diamonds) are in such good agreement as shown in Figure 4-9 (b), it would appear that the x behavior of the Raman bands for bulk Si-Ge alloys is fairly certain. We will examine possible reasons for this downshift.

We can rule out the possibility of strain and phonon confinement. Oxide induced compressive strain would be expected to upshift the band instead of downshifting it. Our nanowires are large in diameter (~ 80 – 100 nm) and should exhibit bulk behavior. Therefore, the difference in experimental nanowire and bulk results cannot be due to phonon confinement effects. Elevated nanowire temperatures due to laser heating would be expected to lower the band frequencies as the lattice undergoes thermal expansion. However, the laser power we used here was about 0.7 mW at a 1 μm size spot, the typical laser power we worked with for micro-Raman on nanowire bundles and single nanowires. Though we did not carry out experiments under different laser powers to definitely exclude the possibility of heating induced downshifting, our other experiments of micro-Raman on single GaP nanowires with the same laser power did not show significant peak shifting compared to other published Raman peak positions from GaP nanoparticles [25, 29]. Therefore, heating should not be the main factor to downshift the

peak position so much as observed in the Si-Si peak, especially for nanowires with Ge concentration (x) greater than 0.6.

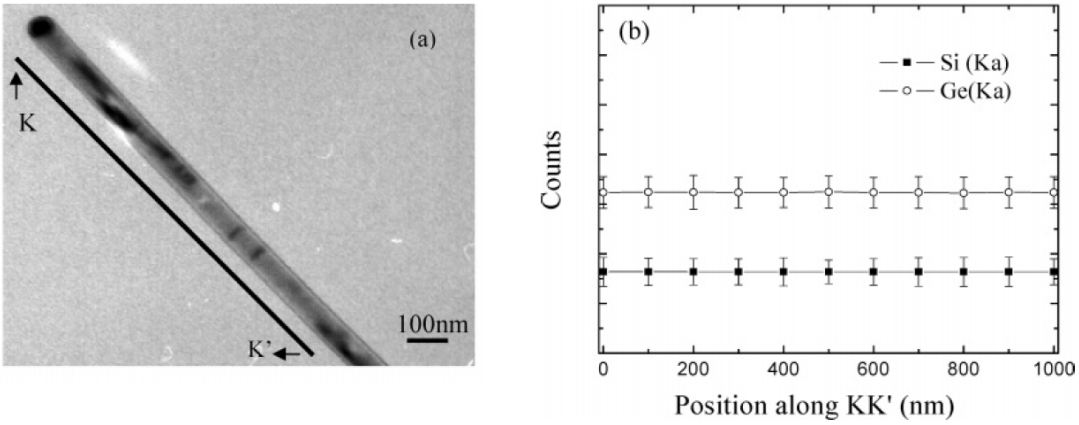

Figure 4-10: (a) TEM image of one $Si_{1-x}Ge_x$ nanowire; (b) The EDS profiles taken along the line KK' in (a), and the EDS results indicates Si/Ge ratio is nearly homogeneous along the $Si_{1-x}Ge_x$ nanowire [27].

A Ge coating on the outside of the $Si_{1-x}Ge_x$ nanowire may offer an explanation for this Si-Si band downshift compared to bulk or LPE film. Unfortunately, we haven't analyzed Ge concentration change across the nanowires in EDS for our $Si_{1-x}Ge_x$ nanowires. We only know our samples have uniform Si/Ge concentration ratio along the nanowire [27] as shown in Figure 4-10 and that concentration ratio is used to label our sample (we shared the same samples with the author in Ref. [27]). However, in Ref. [30] whose author fabricated the $Si_{1-x}Ge_x$ nanowires studied in this thesis, the author points out that it is possible to have a thin Ge coating over the $Si_{1-x}Ge_x$ nanowires, if the inlet gas ratio of GeH_4 / (SiH_4 + GeH_4) falls into a certain range during fabrication. It is also mentioned in Ref. [31] that $Si_{1-x}Ge_x$ nanowires prepared by VLS process exhibit a core-

shell structure with a low Ge concentration in core and high Ge concentration in shell. Here, I make the assumption that our $Si_{1-x}Ge_x$ nanowires have a Ge-rich shell and a Si-rich core.

Later in Chapter 6.4, I will present simulation results to support the conclusion that for certain diameter of GaP nanowires, measured Raman intensities are dominated by two regions of the nanowire. These two regions are both near the surface. As for the simulation, $Si_{1-x}Ge_x$ and GaP are only different in their dielectric constants. Therefore, we expect the simulation results and conclusions from GaP to be suitable also for our $Si_{1-x}Ge_x$ nanowires. From this simulation result and the assumption of the Ge rich shell, we conclude that our sample is mislabeled for Raman purpose. They should have been labeled according to the Si/Ge ratio in the shell instead of the overall ratio, and these new labels x would be greater than the existing labels. This currently underestimated labels x leads to the Si-Si band's left-shift. However, all these are based on assumptions, and require our further investigation.

4.4 Conclusion

We have grown $Si_{1-x}Ge_x$ nanowires by the CVD approach with gold particle using gas mixtures of silane, germane and hydrogen. Nanowires with most probable diameter in the range ~ 80-100 nm could be produced almost over the entire range $0<x<1$. The nanowires were found to have uniform Si to Ge ratio along their axis. The Raman spectra of these $Si_{1-x}Ge_x$ nanowires show three main bands (Si-Si, Si-Ge, Ge-Ge). The x dependence of the prominent frequencies is in good agreement with the recent VDOS

calculations of SiGe nanoparticles by Ren, Cheng and Yu in Ref. [19]. We also observed several weaker Raman features (e.g. peak A, B and shoulder C in Figure 4-8) also in good agreement with their theoretical results. The Raman spectra strongly resemble the calculated VDOS, indicating the Raman matrix element is a weak function of frequency. As previously found in the bulk, the Si-Si peak in our nanowires is the most sensitive to Ge concentration, exhibiting a linear downshift with increasing x for $x \leq 0.5$. Raman scattering can therefore be used to estimate the Ge concentration in single $Si_{1-x}Ge_x$ nanowire. The nanowire's Raman bands appear downshifted by 5 ~ 15 cm^{-1} (depending on x) relative to those observed previously in bulk $Si_{1-x}Ge_x$ samples or LPE films. We also find a slightly different x dependence for the strongest intensity band frequencies than observed in bulk and LPE films. The reason for these small discrepancies between bulk and nanowire SiGe is not yet clear.

Chapter 5

Computational Methods for E field Scattered by Single Nanowire

In this chapter, I will present three different methods to calculate the electric field scattered by a single nanowire and the electric field distribution within that nanowire. These computations are all based on the classical theory, with no quantum theory involved. We start with Maxwell's equations:

$$\nabla \cdot \vec{D} = \rho_F, \tag{5.1}$$

$$\nabla \times \vec{E} + \frac{\partial \vec{B}}{\partial t} = 0, \tag{5.2}$$

$$\nabla \cdot \vec{B} = 0, \tag{5.3}$$

$$\nabla \times \vec{H} = \overrightarrow{J_F} + \frac{\partial \vec{D}}{\partial t}, \tag{5.4}$$

where $\vec{E}$ is the electric field, $\vec{B}$ is the magnetic field, ρ_F and J_F are the free charge density and current density, respectively. The definitions of $\vec{D}$ and $\vec{\mathrm{H}}$ are:

$$\vec{D} = \varepsilon_0 \vec{E} + \vec{P}, \tag{5.5}$$

$$\vec{H} = \frac{1}{\mu_0}\vec{B} - \vec{M}. \tag{5.6}$$

Eq. (5.1) - (5.6) are not sufficient, and we need the following relations:

$$\overrightarrow{J_F} = \sigma \vec{E}, \tag{5.7}$$

$$\vec{B} = \mu \vec{H}, \tag{5.8}$$

$$\vec{P} = \varepsilon_0 \mathcal{X} \vec{E}, \tag{5.9}$$

where σ is the conductivity, μ is the permeability, and $\mathcal{X}$ is the electric susceptibility.

5.1 Mie Scattering from an Infinitely Long Cylinder

Mie theory is an analytical solution to Maxwell's equations. It was first developed by German physicist Gustav Mie, to study the scattering of electromagnetic wave by spherical particles. The theory was later developed to analytically solve the scattering problems by stratified spheres and infinite cylinders.

One of the limitations of Mie scattering is that it can only deal with an incident plane wave, while in our experiments we use Gaussian wave excitations. I will follow the symbols and derivations in Ref. [32].

We can easily write down a plane electromagnetic wave as:

$$\vec{E}_i = \vec{E}_0 exp\,(i\vec{k}\cdot\vec{x} - i\omega t), \tag{5.10}$$

$$\vec{H}_i = \vec{H}_0 exp\,(i\vec{k}\cdot\vec{x} - i\omega t), \tag{5.11}$$

and we are able to obtain the following:

$$\nabla^2\vec{E} + k^2\vec{E} = 0, \tag{5.12}$$

$$\nabla^2\vec{H} + k^2\vec{H} = 0, \tag{5.13}$$

where $k^2 = \omega^2\varepsilon\mu$. In addition, $\vec{E}$ and $\vec{H}$ are not independent, they must satisfy:

$$\nabla\times\vec{E} = i\omega\mu\vec{H}, \tag{5.14}$$

$$\nabla\times\vec{H} = -i\omega\varepsilon\vec{E}. \tag{5.15}$$

Suppose that, given a scalar function φ and an arbitrary constant vector $\vec{c}$, we construct a vector $\vec{M}$:

$$\vec{M} = \nabla\times(\vec{c}\varphi). \tag{5.16}$$

This vector $\vec{M}$ satisfies:

$$\nabla \cdot \vec{M} = 0, \tag{5.17}$$

$$\nabla^2 \vec{M} + k^2 \vec{M} = \nabla \times [\vec{c}(\nabla^2 \varphi + k^2 \varphi)]. \tag{5.18}$$

Therefore, M satisfies the vector wave equation (5.12) if φ is a solution to the scalar wave equation:

$$\nabla^2 \varphi + k^2 \varphi = 0. \tag{5.19}$$

We may rewrite Eq. (5.16) as $\vec{M} = -\vec{c} \times (\nabla \varphi)$, which clearly shows $\vec{M}$ is perpendicular to vector $\vec{c}$. Now let us construct another vector:

$$\vec{N} = \frac{\nabla \times \vec{M}}{k}. \tag{5.20}$$

This vector $\vec{N}$ has zero divergence and satisfies the vector wave equation:

$$\nabla^2 \vec{N} + k^2 \vec{N} = 0 \tag{5.21}$$

and

$$\nabla \times \vec{N} = k\vec{M}. \tag{5.22}$$

Therefore, $\vec{M}$ and $\vec{N}$ have all the properties of an electromagnetic wave: they satisfy vector wave equation, they are divergence free, curl of $\vec{M}$ is proportional $\vec{N}$, and curl $\vec{N}$ of is proportional to $\vec{M}$.

To obtain the analytical results for scattering from an infinitely long cylinder as depicted by Figure 5-1, we start with the scalar wave equation (5.19). In the following derivations, we use subscripts “i”, “l”, and “s” for incident wave, E or H field inside cylinder, and scattered wave respectively.

In a cylindrical polar coordinate system (Figure 5-2), Eq. (5.19) can be rewritten as:

$$\frac{1}{r}\frac{\partial}{\partial r}\left(r\frac{\partial \varphi}{\partial r}\right)+\frac{1}{r^2}\frac{\partial^2 r}{\partial \phi^2}+\frac{\partial^2 \varphi}{\partial z^2}+k^2\varphi=0. \tag{5.23}$$

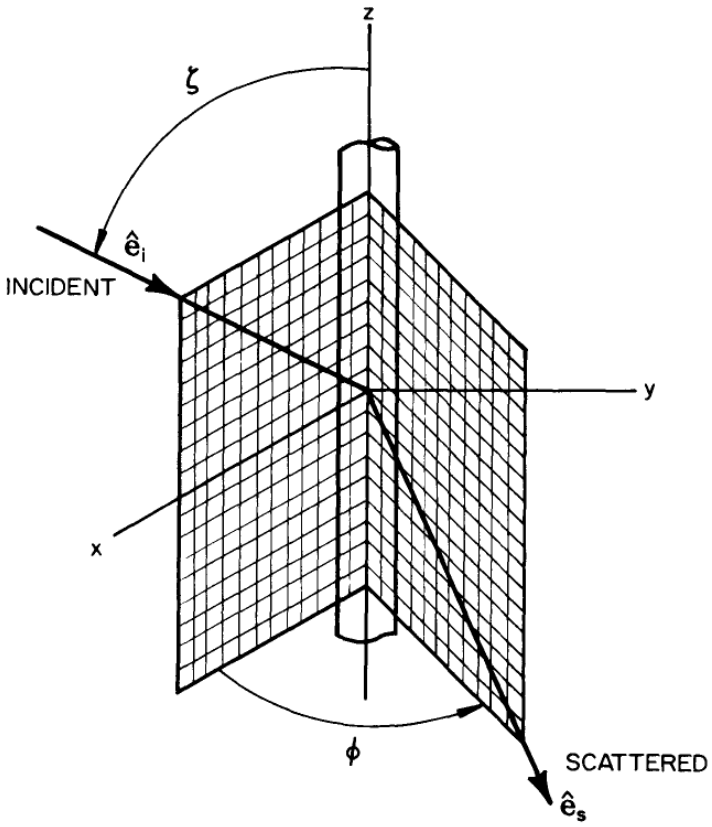

Figure 5-1: Infinitely long cylinder illuminated by a plane wave [32].

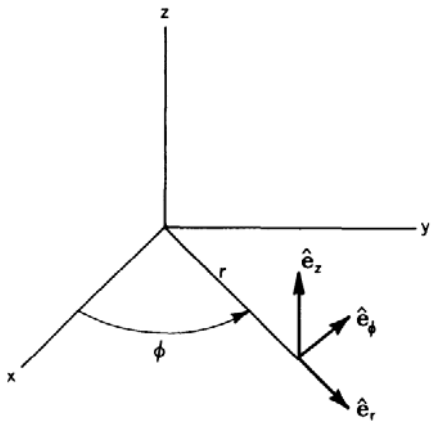

Figure 5-2: Cylindrical polar coordinate system. Cylinder axis is along z.

The solution to Eq. (5.23) takes the following form:

$$\varphi_n(r,\phi,z) = Z_n(\rho)e^{in\phi}e^{ihz} \qquad (n = 0, \pm 1, \dots), \tag{5.24}$$

where $\rho = r\sqrt{k^2 - h^2}$ and Z_n is a solution to the Bessel equation:

$$\rho\frac{\partial}{\partial\rho}\left(\rho\frac{\partial}{\partial\rho}Z_n\right) + (\rho^2 - n^2)Z_n = 0. \tag{5.25}$$

The linearly independent solutions to Eq. (5.25) are the Bessel functions of the first and second kind, J_n and Y_n with integer n. The constant h is dictated by the form of incident radiation and boundary conditions at the interface of the cylinder and surrounding medium.

The vector cylindrical harmonics generated by Eq. (5.24) are:

$$\vec{M}_n = \nabla \times \left(\hat{\vec{e}}_z\varphi_n\right) = \sqrt{k^2 - h^2}\left(in\frac{Z_n(\rho)}{\rho}\hat{\vec{e}}_r - Z_n'(\rho)\hat{\vec{e}}_\phi\right)e^{i(n\phi+hz)}, \tag{5.26}$$

$$\vec{N}_n = \frac{\nabla\times\vec{M}_n}{\mathrm{k}} = \frac{\sqrt{k^2-h^2}}{k}(ihZ_n'(\rho)\hat{\vec{e}}_r - hn\frac{Z_n(\rho)}{\rho}\hat{\vec{e}}_\phi + \sqrt{k^2 - h^2}Z_n(\rho)\hat{\vec{e}}_z)e^{i(n\phi+hz)}. \tag{5.27}$$

5.1.1 Incident Electric Field Parallel to the xz Plane

When the polarization of the incident light is parallel to the xz plane in Figure 5-1, we can express the incident electric field:

$$\vec{E}_i = E_0\left(sin\zeta\hat{\vec{e}}_z - cos\zeta\hat{\vec{e}}_x\right)e^{-ik(rsin\zeta cos\phi + zcos\zeta)} \tag{5.28}$$

in vector cylindrical harmonics as:

$$\vec{E}_i = \sum_{n=-\infty}^{\infty}[A_n\vec{M}_n^{(1)} + B_n\vec{N}_n^{(1)}]. \tag{5.29}$$

The superscript (1) in eq. (5.29) means we only use Bessel functions of the first kind in order to have a finite value at $r = 0$. To determine the coefficients A_n and B_n, we use the orthogonality of the vector harmonics, and can finally conclude:

$$A_n = 0, \tag{5.20}$$

$$B_n = \frac{E_0(-i)^n}{ksin\zeta}. \tag{5.21}$$

Therefore, we can write the incident electromagnetic field as:

$$\vec{E}_i = \sum_{n=-\infty}^{\infty} E_n \vec{N}_n^{(1)}, \tag{5.22}$$

$$\vec{H}_i = \frac{-ik}{\omega\mu} \sum_{n=-\infty}^{\infty} E_n \vec{M}_n^{(1)}, \tag{5.23}$$

where

$$E_n = E_0 \frac{(-i)^n}{ksin\zeta}. \tag{5.24}$$

Next, we express the electromagnetic field in terms of Bessel functions of the first kind due to the finiteness requirement at the origin:

$$\vec{E}_l = \sum_{n=-\infty}^{\infty} E_n [g_n \vec{M}_n^{(1)} + f_n \vec{N}_n^{(1)}], \tag{5.25}$$

$$\vec{H}_l = \frac{-ik}{\omega\mu} \sum_{n=-\infty}^{\infty} E_n [g_n \vec{N}_n^{(1)} + f_n \vec{M}_n^{(1)}]. \tag{5.26}$$

The scattered electromagnetic field should be expressed in terms of Bessel functions of the third kind, an outgoing wave:

$$\vec{E}_s = -\sum_{n=-\infty}^{\infty} E_n [b_{nI} \vec{N}_n^{(3)} + i a_{nI} \vec{M}_n^{(3)}], \tag{5.27}$$

$$\vec{H}_s = \frac{ik}{\omega\mu} \sum_{n=-\infty}^{\infty} E_n [b_{nI} \vec{M}_n^{(3)} + i a_{nI} \vec{N}_n^{(3)}]. \tag{5.28}$$

If we apply the boundary conditions at $r = a$, we can obtain the coefficients:

$$a_{nI} = \frac{C_n V_n - B_n D_n}{W_n V_n + i D_n^2}, \tag{5.29}$$

$$b_{nI} = \frac{W_n B_n + iC_n D_n}{W_n V_n + iD_n^2}, \tag{5.30}$$

$$D_n = n\cos\zeta\eta J_n(\eta) H_n^{(1)}(\xi)\left(\frac{\xi^2}{\eta^2} - 1\right), \tag{5.31}$$

$$C_n = n\cos\zeta\eta J_n(\eta) J_n(\xi)\left(\frac{\xi^2}{\eta^2} - 1\right), \tag{5.32}$$

$$B_n = \xi[m^2 \xi J_n'(\eta) J_n(\xi) - \eta J_n'(\xi) J_n(\eta)], \tag{5.33}$$

$$V_n = \xi[m^2 \xi J_n'(\eta) H_n^{(1)}(\xi) - \eta J_n(\eta) H_n^{(1)\prime}(\xi)], \tag{5.34}$$

$$W_n = i\xi[\eta J_n(\eta) H_n^{(1)\prime}(\xi) - \xi J_n'(\eta) H_n^{(1)}(\xi)], \tag{5.35}$$

where m is refractive index of the cylinder relative to the surrounding medium, and

$$\xi = x\sin\zeta, \tag{5.36}$$

$$\eta = x\sqrt{m^2 - \cos^2\zeta}, \tag{5.37}$$

$$x = ka. \tag{5.38}$$

When the incident light is perpendicular to the cylinder axis ($\zeta = 90°$):

$$a_{nI} = 0, \tag{5.39}$$

$$b_{nI} = \frac{J_n(mx) J_n'(x) - m J_n'(mx) J_n(x)}{J_n(mx) H_n^{(1)\prime}(x) - m J_n'(mx) H_n^{(1)}(x)}, \tag{5.40}$$

$$f_n = \frac{J_n(x) - b_{nI} H_n^{(1)}(x)}{J_n(mx)}, \tag{5.41}$$

$$g_n = 0. \tag{5.42}$$

5.1.2 Incident Electric Field Perpendicular to the xz Plane

In this case, the incident electric field is:

$$\vec{E}_i = E_0 \hat{\vec{e}}_y e^{-ik(r\sin\zeta\cos\phi + z\cos\zeta)} = -i\sum_{n=-\infty}^{\infty} E_n \vec{M}_n^{(1)}. \tag{5.43}$$

The scattered field can be written as:

$$\vec{E}_s = \sum_{n=-\infty}^{\infty} E_n[b_{nI}\vec{N}_n^{(3)} + ia_{nII}\vec{M}_n^{(3)}], \tag{5.44}$$

$$a_{nII} = \frac{A_n V_n - iC_n D_n}{W_n V_n + iD_n^2}, \tag{5.45}$$

$$b_{nII} = -i\frac{C_n W_n + A_n D_n}{W_n V_n + iD_n^2}, \tag{5.46}$$

where C_n, D_n, W_n and V_n are defined in the previous section, and

$$A_n = i\xi[\xi J_n'(\eta)J_n(\xi) - \eta J_n'(\xi)J_n(\eta)]. \tag{5.47}$$

When the incident light is perpendicular to the cylinder axis ($\zeta = 90°$):

$$a_{nII} = \frac{mJ_n(mx)J_n'(x) - J_n'(mx)J_n(x)}{mJ_n(mx)H_n^{(1)\prime}(x) - J_n'(mx)H_n^{(1)}(x)}, \tag{5.48}$$

$$b_{nII} = 0, \tag{5.49}$$

$$f_n = 0, \tag{5.50}$$

$$g_n = i\frac{a_{nII}H_n^{(1)}(x) - J_n(x)}{mJ_n(mx)}. \tag{5.51}$$

5.1.3 Conclusion of Mie Scattering

By use of these equations, we are able to numerically calculate both the scattered electromagnetic field (far field and near field) and the field inside the cylinder. Although we have the summations from $-\infty$ to ∞ in these equations, they converge very quickly and we only need to sum from $n = -15$ to $n = 15$ in practice. These are all the advantages of the Mie scattering. However, it also has two main disadvantages: (1) it requires a plane wave incident; (2) it can only deal with spheres and infinite long cylinders, while our real nanowires are finite cylinders.

5.2 Discrete Dipole Approximation (DDA) Method

5.2.1 Introduction to DDA method

The Discrete Dipole Approximation is a finite element method, first proposed by Purcell and Pennypacker in 1973 to calculate scattering and absorption of electromagnetic fields by irregular objects such as interstellar dust. In this method, the continuum target is replaced with an array of discrete dipoles, or more precisely, discrete polarizable points [33].

If we replace an arbitrary object by N dipoles at position r_i with polarizability tensor $\boldsymbol{\alpha_i}$, the polarization is:

$$\vec{P}_i = \boldsymbol{\alpha_i} \cdot \vec{E}_i(\vec{r}_i), \tag{5.52}$$

where $\vec{E}_i(\vec{r}_i)$ is the sum of incident plane wave

$$\vec{E}_{inc,i} = \vec{E}_0 \exp\,(i\vec{k}_0 \cdot \vec{r}_i - i\omega t), \tag{5.53}$$

and contributions from dipoles at other sites

$$\vec{E}_{other,i} = -\sum_{j\neq i} \boldsymbol{A_{ij}} \cdot \vec{P}_j. \tag{5.54}$$

Here $\vec{k}_0$ is the propagation vector in vacuum, $\left|\vec{k}_0\right| = \frac{\omega}{c}$, $\vec{E}$ and $\vec{P}$ are three-dimensional vectors, and matrix $\boldsymbol{A}$ is a $N \times N$ array of 3×3 tensor.

Combining Eq. (5.52) – (5.54) together, we obtain:

$$(\boldsymbol{\alpha_i})^{-1} \cdot \vec{P}_i + \sum_{j\neq i} \boldsymbol{A_{ij}} \cdot \vec{P}_j = \vec{E}_{inc,i}. \tag{5.55}$$

Now the scattering problem for an array of point dipoles has become a system of linear equations (5.55) and can be solved to arbitrary accuracy. The technique of Fast

Fourier Transform (FFT) can be applied to solve the system of linear equations with $N > 10^5$ [34].

Representing a continuum object with a array of dipoles requires us to specify (1) the locations of each dipole $\vec{r}_i$; and (2) the polarizability tensor of individual dipole $\boldsymbol{\alpha_i}$. We will need to first set up lattice grids and then determine the occupied grid sites. In the simplest case, a cubic lattice, we want to represent our target by N dipoles and suppose that the volume of our target is V. The lattice spacing can be determined as $d = (\frac{V}{N})^{1/3}$. The continuum target is characterized by its complex dielectric function ε and complex refractive index $m = \varepsilon^{1/2}$, in the limit of $k_0 d \to 0$, $\boldsymbol{\alpha_i}$ is the Clausius-Mossotti polarizability [33]:

$$\alpha_i^{CM} = \frac{3d^3}{4\pi}\left(\frac{m_i^2-1}{m_i^2+2}\right). \tag{5.56}$$

But with a finite $k_0 d$, the polarizability α_i should include a radiative-reaction correction [33]:

$$\alpha_i = \frac{\alpha_i^{CM}}{1-\frac{2}{3}i\frac{\alpha_i^{CM}}{d^3}(k_0 d)^3}. \tag{5.57}$$

5.2.2 Software for DDA Simulation in This Thesis

For the numerical study of electric field inside nanowire by implementation of DDA method in this thesis, I obtain the results by use of shared DDA software, "DDSCAT 6.1" coded by B. T. Draine in FORTRAN.

The principle advantage of DDA method is its flexibility in the geometry of the target which is only limited by two requirements for the lattice spacing d: (1) d should be smaller than any structural length in the target; (2) d should be smaller than wavelength. This software is able to generate a dipole array for a variety of geometries, such as finite length cylinder, and also accepts user-defined array of point dipoles.

The main drawbacks of this DDSCAT 6.1 software are that: (1) we can only use a monochromatic plane wave as the incident field; (2) for fixed $|m|k_0 d$, the accuracy decreases with increasing $|m|$, and with this software, the best accuracy can be achieved with $|m-1| < 2$. However, the refractive index of the material of interest – GaP – is around 3.54.

Other than the electric field inside our target, this software is also capable of computing absorption efficiency factor, scattering efficiency factor, extinction efficiency factor, phase lag efficiency factor, Mueller scattering intensity matrix, radiation force efficiency vector and radiation torque efficiency vector [35].

5.3 Finite Different Time Domain (FDTD) Method

5.3.1 Algorithm of FDTD method

The "Finite Different Time Domain" method is based on a direct numerical approach of time dependent Maxwell's curl equations (5.2) and (5.4). The general idea is that given an initial electromagnetic field, we are able to update the electromagnetic field at the next time step by using the field value at the current step.

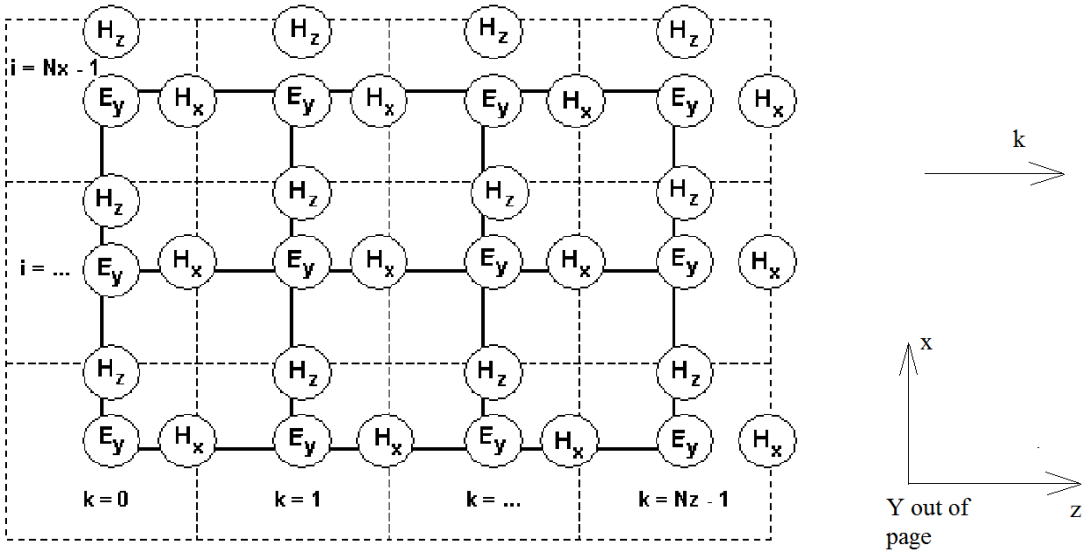

Figure 5-3: Location of 2D TE field in computational domain [36].

The main difference between FDTD and DDA is the setup of grid points. In DDA, electric fields from TE wave and TM wave are on the same grid point, but that is not the case in FDTD. Let us investigate the 2D TE and TM wave in FDTD first [36].

Figure 5-3 illustrates how to put electric and magnetic field onto the grid points. We have a 2D TE field propagating along z direction in a lossless medium and the non-zero components of the electromagnetic wave are E_y, H_x and H_z. Each dashed square is one space cell. E_y sits at the center of cell (i, k), but H_x of that cell is located at $(i, k + \frac{1}{2})$, and H_z of that cell is located at $(i + \frac{1}{2}, k)$.

The Maxwell's curl equations are:

$$\frac{\partial E_y}{\partial t} = \frac{1}{\varepsilon}\left(\frac{\partial H_x}{\partial z} - \frac{\partial H_z}{\partial x}\right), \tag{5.58}$$

$$\frac{\partial H_x}{\partial t} = \frac{1}{\mu}\frac{\partial E_y}{\partial z}, \tag{5.59}$$

$$\frac{\partial H_z}{\partial t} = -\frac{1}{\mu}\frac{\partial E_y}{\partial x}, \tag{5.60}$$

where ε is the dielectric permittivity and μ is the magnetic permeability. With the locations of E_y, H_x and H_z in Figure 5-3, Eq. (5.58) can be written as:

$$\frac{E_y^n(i,k)-E_y^{n-1}(i,k)}{\Delta t} = \frac{1}{\varepsilon}\left(\frac{H_x^{n-\frac{1}{2}}\left(i,k+\frac{1}{2}\right)-H_x^{n-\frac{1}{2}}\left(i,k-\frac{1}{2}\right)}{\Delta z} - \frac{H_z^{n-\frac{1}{2}}(i+1/2,k)-H_z^{n-\frac{1}{2}}(i-1/2,k)}{\Delta x}\right). \tag{5.61}$$

The eq. (5.58) – (5.60) will take the forms:

$$E_y^n(i,k) = E_y^{n-1}(i,k) + \frac{\Delta t}{\varepsilon \Delta z}\left[H_x^{n-\frac{1}{2}}\left(i,k+\frac{1}{2}\right) - H_x^{n-\frac{1}{2}}\left(i,k-\frac{1}{2}\right)\right] - \frac{\Delta t}{\varepsilon \Delta x}\left[H_z^{n-\frac{1}{2}}\left(i+\frac{1}{2},k\right) - H_z^{n-\frac{1}{2}}\left(i-\frac{1}{2},k\right)\right], \tag{5.62}$$

$$H_x^{n+1/2}(i,k+1/2) = H_x^{n-1/2}(i,k+1/2) + \frac{\Delta t}{\mu \Delta z}[E_y^n(i,k+1) - E_y^n(i,k)], \tag{5.63}$$

$$H_z^{n+1/2}(i+1/2,k) = H_z^{n-1/2}(i+1/2,k) + \frac{\Delta t}{\mu \Delta x}[E_y^n(i+1,k) - E_y^n(i,k)]. \tag{5.64}$$

The superscript n labels the time steps and the indices i, k label space steps. Eq. (5.62) – (5.64) use central difference approximations for numerical derivatives in space and time. We typically need to use 10 - 20 space steps per wavelength and the time step is determined by the Courant limit:

$$\Delta t \leq 1/(c\sqrt{1/(\Delta x)^2 + 1/(\Delta z)^2}). \tag{5.65}$$

For a 2D TM wave travelling along z axis, it will have non-zero H_y, E_x and E_z and these non-zero components are located on the computational domain as depicted in Figure 5-4. The magnetic field is centered in each space cell (i, k), but E_x of that cell locates at $(i, k+\frac{1}{2})$, and E_z of that cell locates at $(i+\frac{1}{2}, k)$.

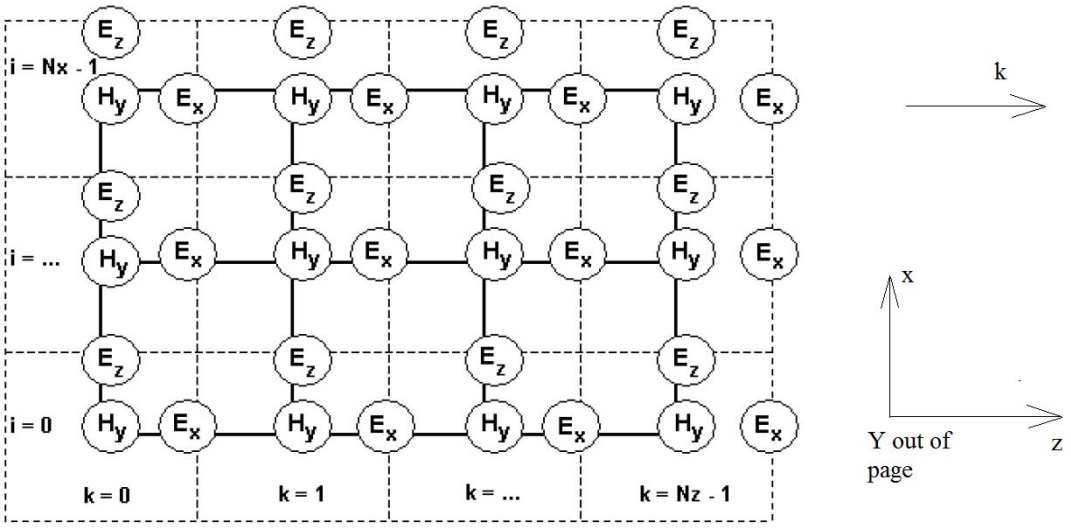

Figure 5-4: Location of 2D TM field in computational domain [36].

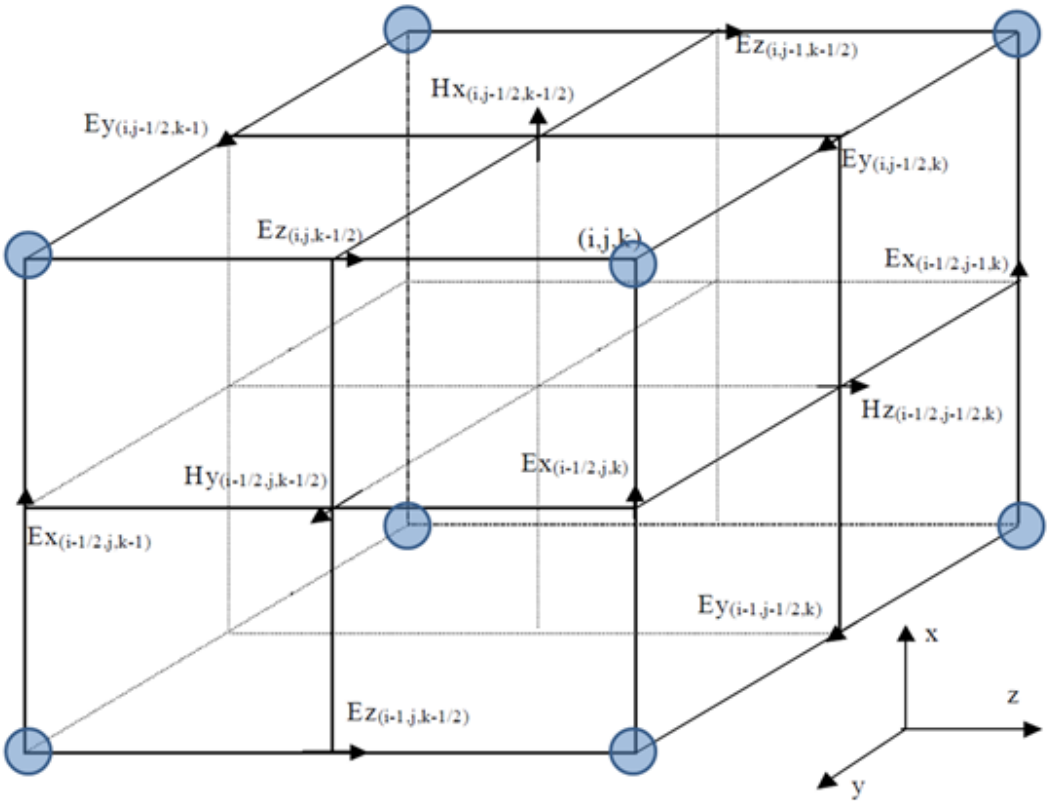

Figure 5-5: Displacement of electric and magnetic vector about a cubic unit cell [36].

Figure 5-5 shows the displacement of electromagnetic field in the general 3D case. The eight circles at the corners are integer grid points, and from the figure, it clearly shows the electric and magnetic components are interleaved for the purpose of applying a leapfrog algorithm. Similar to Eq. (5.62) – (5.64), we can update the electromagnetic field in the following way:

$$H_{x,i,j-\frac{1}{2},k-\frac{1}{2}}^{n+1/2} = H_{x,i,j-\frac{1}{2},k-\frac{1}{2}}^{n-1/2} + \frac{\Delta t}{\mu\Delta z}\left(E_{y,i,j-\frac{1}{2},k}^{n} - E_{y,i,j-\frac{1}{2},k-1}^{n}\right) - \frac{\Delta t}{\mu\Delta y}(E_{z,i,j,k-\frac{1}{2}}^{n} - E_{z,i,j-1,k-\frac{1}{2}}^{n}), \tag{5.66}$$

$$H_{y,i-\frac{1}{2},j,k-\frac{1}{2}}^{n+1/2} = H_{y,i-\frac{1}{2},j,k-\frac{1}{2}}^{n-1/2} + \frac{\Delta t}{\mu\Delta x}\left(E_{z,i,j,k-\frac{1}{2}}^{n} - E_{z,i-1,j,k-\frac{1}{2}}^{n}\right) - \frac{\Delta t}{\mu\Delta z}(E_{x,i-\frac{1}{2},j,k}^{n} - E_{x,i-\frac{1}{2},j,k-1}^{n}), \tag{5.67}$$

$$H_{z,i-\frac{1}{2},j-\frac{1}{2},k}^{n+1/2} = H_{z,i-\frac{1}{2},j-\frac{1}{2},k}^{n-1/2} + \frac{\Delta t}{\mu\Delta y}\left(E_{x,i-\frac{1}{2},j,k}^{n} - E_{x,i-\frac{1}{2},j-1,k}^{n}\right) - \frac{\Delta t}{\mu\Delta x}(E_{y,i,j-\frac{1}{2},k}^{n} - E_{y,i-1,j-\frac{1}{2},k-1}^{n}), \tag{5.68}$$

$$E_{x,i-\frac{1}{2},j,k}^{n+1} = \frac{2\varepsilon-\sigma\Delta t}{2\varepsilon+\sigma\Delta t}E_{x,i-\frac{1}{2},j,k}^{n} + \frac{2\Delta t}{(2\varepsilon+\sigma\Delta t)\Delta y}\left(H_{z,i-\frac{1}{2},j+\frac{1}{2},k}^{n+1/2} - H_{z,i-\frac{1}{2},j-\frac{1}{2},k}^{n+1/2}\right) - \frac{2\Delta t}{(2\varepsilon+\sigma\Delta t)\Delta z}(H_{y,i-\frac{1}{2},j,k+\frac{1}{2}}^{n+1/2} - H_{y,i-\frac{1}{2},j,k-\frac{1}{2}}^{n+1/2}), \tag{5.69}$$

$$E_{y,i,j-\frac{1}{2},k}^{n+1} = \frac{2\varepsilon-\sigma\Delta t}{2\varepsilon+\sigma\Delta t}E_{y,i,j-\frac{1}{2},k}^{n} + \frac{2\Delta t}{(2\varepsilon+\sigma\Delta t)\Delta z}\left(H_{x,i,j-\frac{1}{2},k+\frac{1}{2}}^{n+1/2} - H_{x,i,j-\frac{1}{2},k-\frac{1}{2}}^{n+1/2}\right) - \frac{2\Delta t}{(2\varepsilon+\sigma\Delta t)\Delta x}(H_{z,i+\frac{1}{2},j-\frac{1}{2},k}^{n+1/2} - H_{z,i-\frac{1}{2},j-\frac{1}{2},k}^{n+1/2}), \tag{5.70}$$

$$E_{z,i,j,k-\frac{1}{2}}^{n+1} = \frac{2\varepsilon-\sigma\Delta t}{2\varepsilon+\sigma\Delta t}E_{z,i,j,k-\frac{1}{2}}^{n} + \frac{2\Delta t}{(2\varepsilon+\sigma\Delta t)\Delta x}\left(H_{y,i+\frac{1}{2},j,k-\frac{1}{2}}^{n+1/2} - H_{y,i-\frac{1}{2},j,k-\frac{1}{2}}^{n+1/2}\right) - \frac{2\Delta t}{(2\varepsilon+\sigma\Delta t)\Delta y}(H_{x,i,j+\frac{1}{2},k-\frac{1}{2}}^{n+1/2} - H_{x,i,j-\frac{1}{2},k-\frac{1}{2}}^{n+1/2}). \tag{5.71}$$

Similar to Eq. (5.65), the time step should satisfy the Courant-Friedrichs-Levy condition:

$$\Delta t \leq 1/(c\sqrt{1/(\Delta x)^2 + 1/(\Delta y)^2 + 1/(\Delta z)^2}). \tag{5.72}$$

The field propagated by the FDTD algorithm takes the form of:

$$\vec{E}(x, y, z) = \vec{E}_0(x, y, z) sin\ (\omega t + \varphi). \tag{5.73}$$

To obtain the complex field amplitude and phase information, Fourier transform should be performed during the last time period of FDTD simulation.

5.3.2 Boundary Conditions in FDTD method

This FDTD algorithm must be modified at boundaries of the computational region where suitable numerical absorbing boundary conditions (ABC) are applied. There are several choices for the ABC, but the perfectly matched layer (PML) boundary conditions have the best performance [36]. One version of the PML is called anisotropic PML, or un-split PML (UPML). The implementation of the UPML boundary conditions is based on Maxwellian formulation, and their absorbing properties are physically equivalent to those of an absorbing uni-axial anisotropic medium with the following permittivity and permeability tensors:

$$\boldsymbol{\varepsilon} = \varepsilon \boldsymbol{S}, \boldsymbol{\mu} = \mu \boldsymbol{S}, \tag{5.74}$$

where

$$\boldsymbol{S} = \begin{pmatrix} s^{-1} & 0 & 0 \\ 0 & s & 0 \\ 0 & 0 & s \end{pmatrix}, s = \kappa - i\frac{\sigma}{\varepsilon_0 \omega}. \tag{5.75}$$

A plane wave incident on the above uni-axial medium will purely transmit into it. This reflectionless propagation is independent on the angle of incident, polarization and frequency of the wave. However, we need special treatment at the corner regions. For example, the corner in a X-Z plane requires the tensor $\boldsymbol{S}$ in Eq. (5.74) to be:

$$\boldsymbol{S} = \begin{pmatrix} s_x^{-1} & 0 & 0 \\ 0 & s_x & 0 \\ 0 & 0 & s_x \end{pmatrix} \begin{pmatrix} s_z & 0 & 0 \\ 0 & s_z & 0 \\ 0 & 0 & s_z^{-1} \end{pmatrix}, s_x = \kappa_x - i\frac{\sigma_x}{\varepsilon_0 \omega}, s_z = \kappa_z - i\frac{\sigma_z}{\varepsilon_0 \omega}. \quad (5.76)$$

5.3.3 Software for FDTD Method

The simulations by use of FDTD method were performed by Optiwave OptiFDTD 8.0. The main advance in this FDTD software is its ability to use Gaussian wave and a point light source as incident source. This means we are able to simulate the electric field distributions inside a nanowire with laser profile as the incident wave. Besides, we can also use the point light source as the oscillating dipole inside a nanowire to investigate the efficiency of field emission from nanowire. The full picture of classical Rayleigh and Raman scattering is the combination of the above two: (1) distribution of electric field inside nanowire due to incident laser; (2) electric field emitted from oscillating dipoles inside nanowire.

The main disadvantage of FDTD method is its long computational time and it is not practical to calculate far-field emission.

Chapter 6

Antenna Effect in GaP Nanowires

6.1 Introduction to the Antenna Effect

Raman and Rayleigh scattering from nanowires both exhibit characteristics that are quite distinct from bulk materials. One such characteristic is due to the high aspect ratio of nanowires. When a polarized laser illuminates a nanowire, the internal and scattered electric fields are strongly depolarized relative to the incident light when the diameter of the nanowire meets certain conditions.

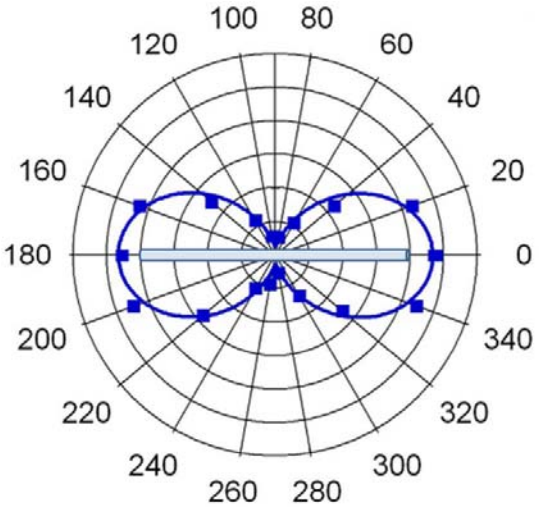

Figure 6-1: Illustration of sample Raman LO mode's Antenna pattern from one GaP nanowire. Collected at room temperature by 514.5 nm excitation.

For example, as depicted in Figure 6-1, the orientation of the subject nanowire is illustrated by a cylinder along 0 – 180 direction. Each square point on this figure has two

coordinates, angle and radius. The angle is the polarization of the incident laser, as well as the polarization of the scattered light which we collect, relative to the nanowire axis. The radius, in this figure, is the Raman intensity of LO mode collected from the GaP nanowire at 514.5 nm excitation. The smooth line is a fit to the pattern which we will discuss later in this chapter. Figure 6-1 indicates that when the incident laser excitation is polarised perpendicular to the nanowire axis, the scattering is largely suppressed compared to the case where the incident polarization is parallel to the nanowire axis. This figure resembles the electric field emission from an antenna, and is therefore called the "antenna effect" with figures like Figure 6-1 called "antenna patterns".

This effect was first observed from nanotubes by Hiroshi Ajiki [37,38]. In this thesis, we systematically study this antenna effect from GaP nanowires, which offer a wider range of diameters than the carbon nanotubes investigated by Hiroshi Ajiki. We propose a model to relate Raman antenna patterns with the Rayleigh antenna pattern from the same nanowire, or with the computed electric field enhancement factors obtained by implementation of the computational methods introduced in the previous chapter.

6.2 Experimental Procedures

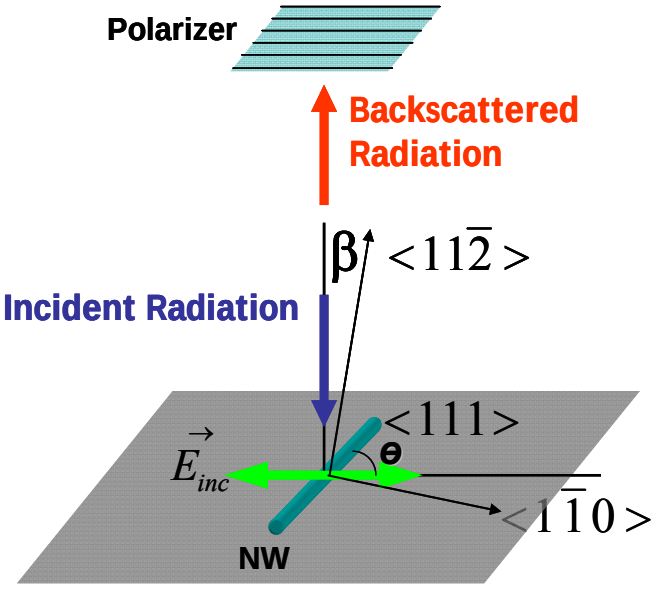

Figure 6-2: Experimental Configuration for Antenna Effect.

Figure 6-2 is the configuration at the microscope and the sample stage. The polarizer was put inside the microscope before the objective lens of the microscope, and was free to rotate. It selected the polarization of both the incident laser and the scattered field. We rotated this polarizer, collected corresponding Rayleigh and Raman scattered fields, and obtained antenna patterns like Figure 6-1.

The GaP nanowires we studied in this chapter were fabricated by the PLV method, using growth conditions discussed in detail in Chapter 2.3. Figure 6-3 shows a TEM image of a typical GaP nanowire studied here. We took some GaP nanowire samples, put them in isopropanol alcohol, mildly sonicated for 30 seconds to break nanowire bundles into isolated nanowires, and dropped solutions on a TEM grid. The

Raman and Rayleigh measurements were performed using the Renishaw InVia Micro-Raman System at room temperature with 514.5nm laser excitation.

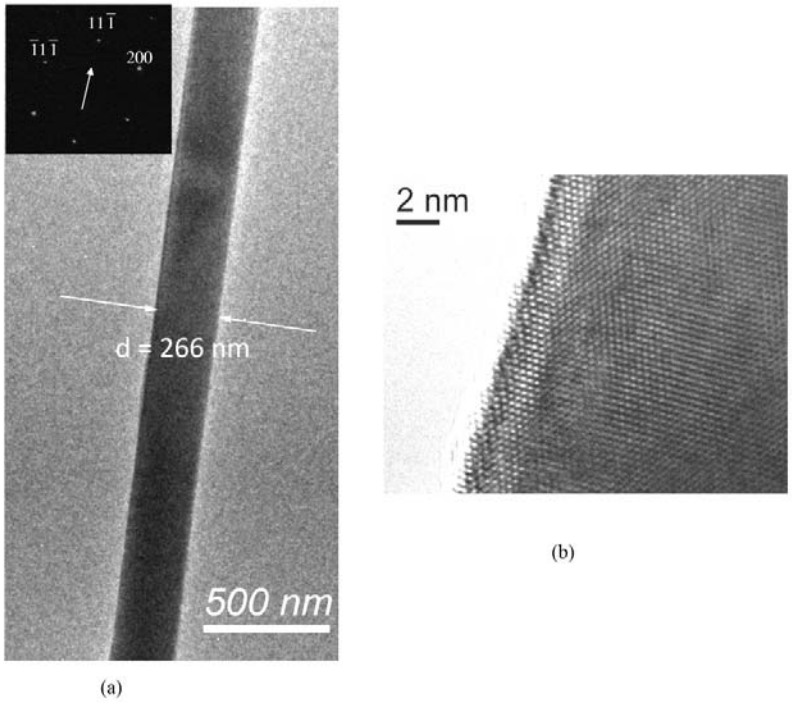

Figure 6-3: (a) Low resolution TEM image of a GaP nanowire with inlet showing the diffraction pattern of this nanowire. (b) High resolution TEM image of the same nanowire showing high quality crystalline structure.

The samples investigated were GaP nanowires suspended over TEM grid holes. The Raman and Rayleigh measurements were taken at the center of the nanowire bridges over the TEM grid. The power of the laser at the sample was around 0.1 mW.

In Figure 6-2, the growth direction of the nanowire can be measured from TEM, which is [111] in this figure. We can take any other two orthogonal directions, such as the $[1\bar{1}0]$ and $[11\bar{2}]$ in the figure, and denote the nanowire's relative orientation to the

incident laser by the angle β which is between the incident laser and axis $[11\bar{2}]$ in Figure 6-2.

6.3 Rayleigh and Raman Antenna Models

Here, I propose the models to explain the Rayleigh and Raman antenna patterns. Since Rayleigh scattering can be treated as a special case of Raman scattering whose Raman tensor is a unit tensor, we will focus on the Raman model.

6.3.1 Introduction to Rayleigh and Raman Antenna Models

As derived in Chapter 3.2, the dipole excited by an incident electromagnetic wave is:

$$\vec{p}^{Ram} \propto \boldsymbol{\alpha'}_{\boldsymbol{k}} Q_k \cdot \overrightarrow{E_0}. \tag{6.1}$$

The intensity of radiation from this oscillating dipole is:

$$I_s \propto |\ddot{\vec{p}}^{Ram} \cdot \hat{e}_s|^2 \propto |\hat{e}_s{}^T \cdot \boldsymbol{\alpha'}_{\boldsymbol{k}} Q_k \cdot \hat{e}_i|^2 I_0 = |\hat{e}_s{}^T \cdot \boldsymbol{R} \cdot \hat{e}_i|^2 I_0, \tag{6.2}$$

where I_0 is the incident light intensity inside sample, and $\boldsymbol{R}$ is the Raman tensor, which is defined as:

$$\boldsymbol{R} = \boldsymbol{\alpha'}_{\boldsymbol{k}} Q_k. \tag{6.3}$$

For zincblende crystals, such as GaP, the Raman tensors for both LO and TO mode are take the following form, but with different constants d:

$$\boldsymbol{R}(x) = \begin{pmatrix} 0 & 0 & 0 \\ 0 & 0 & d \\ 0 & d & 0 \end{pmatrix}, \tag{6.4}$$

$$\boldsymbol{R}(y) = \begin{pmatrix} 0 & 0 & d \\ 0 & 0 & 0 \\ d & 0 & 0 \end{pmatrix}, \tag{6.5}$$

$$\boldsymbol{R}(z) = \begin{pmatrix} 0 & d & 0 \\ d & 0 & 0 \\ 0 & 0 & 0 \end{pmatrix}, \tag{6.6}$$

where $\boldsymbol{R}(x)$, $\boldsymbol{R}(y)$ and $\boldsymbol{R}(z)$ are the Raman tensor when the phonon displacement is along x, y, and z directions, respectively. x, y, and z are along [100], [010] and [001] crystallographic axes. [39].

For Rayleigh scattering, we simply use a unit matrix for the tensor $\boldsymbol{R}$.

In order to obtain the I_0 in eq. (6.2), we need to consider how light with different polarization enters the nanowire.

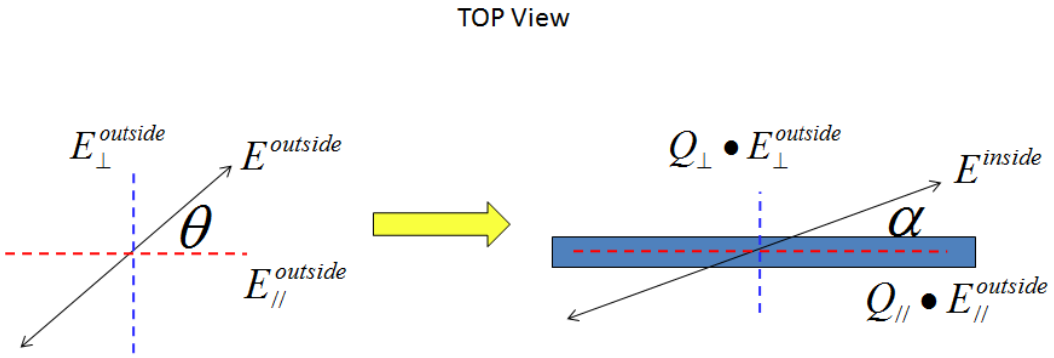

Figure 6-4: Relation of electric field inside nanowire with the field outside nanowire.

In Figure 6-4, the horizontal red dashed lines label the nanowire axis. The electric field at the vicinity outside the nanowire is polarized along a direction which makes an angle θ with the nanowire axis. However, due to the geometry and aspect ratio of the nanowire, usually the electric field inside the nanowire has a different polarization than the field outside. We are able to write:

$$E_{\parallel}^{inside} = Q_{\parallel}^{in} \cdot E_{\parallel}^{outside}, \tag{6.7}$$

$$E_{\perp}^{inside} = Q_{\perp}^{in} \cdot E_{\perp}^{outside}. \tag{6.8}$$

or in a matrix form:

$$\vec{E}^{in} = \boldsymbol{Q}^{in} \cdot \vec{E}^{out}, \tag{6.9}$$

where

$$\boldsymbol{Q}^{in} = \begin{pmatrix} Q_{\parallel}^{in} & 0 & 0 \\ 0 & Q_{\perp}^{in} & 0 \\ 0 & 0 & 0 \end{pmatrix}. \tag{6.10}$$

$\boldsymbol{Q}^{in}$ is the enhancement tensor for light entering into the nanowire. The three orthogonal coordinates for electric fields are along nanowire axis, perpendicular to both nanowire axis and incident laser, along incident laser's direction. Similar to this $\boldsymbol{Q}^{in}$, we define $\boldsymbol{Q}^{out}$, as the enhancement tensor for light coming out from the nanowire:

$$\vec{E}^{out} = \boldsymbol{Q}^{out} \cdot \vec{E}^{in}. \tag{6.11}$$

In our experiments (Figure 6-2), we only collect Raman or Rayleigh scattering outside the nanowire with polarization identical to the incident laser. We write the scattering intensity as:

$$I_s \propto |\hat{e}_s{}^T \cdot \boldsymbol{Q}^{out} \cdot \boldsymbol{R} \cdot \boldsymbol{Q}^{in} \cdot \hat{e}_i|^2, \tag{6.12}$$

where,

$$\hat{e}_s = \hat{e}_i = \begin{pmatrix} cos\theta \\ sin\theta \\ 0 \end{pmatrix}, \tag{6.13}$$

where θ is the angle labeled in Figure 6-2 and Figure 6-4.

In eq. (6.12), the Raman tensor can be determined if we know the nanowire's orientation relative to the incident laser. Therefore, the task left is to find the appropriate enhancement tensor $\boldsymbol{Q}^{in}$ and $\boldsymbol{Q}^{out}$.

6.3.2 Fitting Raman Antenna Patterns with Data from Experimental Rayleigh Antenna Patterns

It is pointed out by Linyou Cao and Bahram Nabet that since the difference in frequency is small between Raman scattering and the incident laser, we can approximately write [40]:

$$\boldsymbol{Q}^{in} = \boldsymbol{Q}^{out} = \boldsymbol{Q} = \begin{pmatrix} Q_{\parallel} & 0 & 0 \\ 0 & Q_{\perp} & 0 \\ 0 & 0 & 0 \end{pmatrix} \tag{6.14}$$

Therefore, the intensity for Rayleigh scattering, by eq. (6.10), is:

$$I_s^{Ray} \propto |\hat{e}_s{}^T \cdot \boldsymbol{Q} \cdot \boldsymbol{Q} \cdot \hat{e}_i|^2 = (Q_{\parallel}{}^2 cos^2\theta + Q_{\perp}{}^2 sin^2\theta)^2 \tag{6.15}$$

Eq. (6.15) points out one way to obtain the enhancement tensor $\boldsymbol{Q}$ – from the experimental Rayleigh antenna patterns. Once we have the enhancement tensor $\boldsymbol{Q}$ and the growth direction of the nanowire, we only have one unknown parameter in the Raman antenna model, the angle β. We are able to find out this angle β by trial and error, i.e., comparing calculated Raman antenna pattern with the experimental pattern. I will elaborate the calculation below.

Referring to Figure 6-2 and Figure 6-4, we are going to introduce two sets of coordinates. The first set, which we call lab coordinates S, has its x along nanowire axis, z along laser incident direction, and y is perpendicular to both x and z. The second set is

the crystal coordinates S', whose x' is along crystallographic axis [100], y' is along [010] and z' is along [001]. We denote, in S', the growth direction as $[A_{x'}, A_{y'}, A_{z'}]$, the axis used to define angle β with laser incident direction as $[C_{x'}, C_{y'}, C_{z'}]$, and the axis perpendicular to the previous two as $[B_{x'}, B_{y'}, B_{z'}]$. All these axis notations are normalized. In Figure 6-2, $[A_{x'}, A_{y'}, A_{z'}]$ is $[1,1,1]/\sqrt{3}$, $[B_{x'}, B_{y'}, B_{z'}]$ is $[1,-1,0]/\sqrt{2}$, and $[C_{x'}, C_{y'}, C_{z'}]$ is $[1,1,-2]/\sqrt{6}$.

In coordinates S', the laser is along:

$$LaserK_{s'} = \begin{pmatrix} LaserK_{x'} \\ LaserK_{y'} \\ LaserK_{z'} \end{pmatrix} = cos\beta \begin{pmatrix} C_{x'} \\ C_{y'} \\ C_{z'} \end{pmatrix} - sin\beta \begin{pmatrix} B_{x'} \\ B_{y'} \\ B_{z'} \end{pmatrix}. \tag{6.16}$$

The y in coordinates S, written in coordinates S', is:

$$y_{s'} = \begin{pmatrix} y_{x'} \\ y_{y'} \\ y_{z'} \end{pmatrix} = sin\beta \begin{pmatrix} C_{x'} \\ C_{y'} \\ C_{z'} \end{pmatrix} + cos\beta \begin{pmatrix} B_{x'} \\ B_{y'} \\ B_{z'} \end{pmatrix}. \tag{6.17}$$

Now, we introduce the transform matrix $\boldsymbol{T}$, for any vertical vector $\vec{V}$, we have:

$$\boldsymbol{T} \cdot \vec{V}_S = \vec{V}_{S'}. \tag{6.18}$$

By picking x, y and z as our V_S, it is easy to obtain:

$$\boldsymbol{T} = \begin{pmatrix} A_{x'} & y_{x'} & LaserK_{x'} \\ A_{y'} & y_{y'} & LaserK_{y'} \\ A_{z'} & y_{z'} & LaserK_{z'} \end{pmatrix}. \tag{6.19}$$

Eq. (6.12) can be written in coordinates S as:

$$I_s^{Ram} \propto \left| \begin{pmatrix} cos\theta \\ sin\theta \\ 0 \end{pmatrix}^T \cdot \begin{pmatrix} Q_{\parallel} & 0 & 0 \\ 0 & Q_{\perp} & 0 \\ 0 & 0 & 0 \end{pmatrix} \cdot \boldsymbol{R}_s \cdot \begin{pmatrix} Q_{\parallel} & 0 & 0 \\ 0 & Q_{\perp} & 0 \\ 0 & 0 & 0 \end{pmatrix} \cdot \begin{pmatrix} cos\theta \\ sin\theta \\ 0 \end{pmatrix} \right|^2. \tag{6.20}$$

Or, if we want to express the Raman tensor in coordinates S':

$$I_s^{Ram} \propto \left| \begin{pmatrix} cos\theta \\ sin\theta \\ 0 \end{pmatrix}^T \cdot \begin{pmatrix} Q_{\parallel} & 0 & 0 \\ 0 & Q_{\perp} & 0 \\ 0 & 0 & 0 \end{pmatrix} \cdot \boldsymbol{T}^{-1} \cdot \boldsymbol{R}_{s'} \cdot \boldsymbol{T} \cdot \begin{pmatrix} Q_{\parallel} & 0 & 0 \\ 0 & Q_{\perp} & 0 \\ 0 & 0 & 0 \end{pmatrix} \cdot \begin{pmatrix} cos\theta \\ sin\theta \\ 0 \end{pmatrix} \right|^2. \tag{6.21}$$

For Raman LO mode, referring to Eq. (6.4) – (6.6), we have the Raman tensor as:

$$\boldsymbol{R}_{s'}^{LO} = \begin{pmatrix} 0 & 0 & 0 \\ 0 & 0 & 1 \\ 0 & 1 & 0 \end{pmatrix} LaserK_{x'} + \begin{pmatrix} 0 & 0 & 1 \\ 0 & 0 & 0 \\ 1 & 0 & 0 \end{pmatrix} LaserK_{y'} + \begin{pmatrix} 0 & 1 & 0 \\ 1 & 0 & 0 \\ 0 & 0 & 0 \end{pmatrix} LaserK_{z'}. \tag{6.22}$$

Since d in Eq. (6.4) – (6.6) is a constant and we are not comparing LO mode intensity with TO mode intensity, we can treat it as "1" to check antenna patterns of LO and TO modes separately, as what we do in Eq. (6.22).

For Raman TO modes, we have two orthogonal directions for TO phonon displacement – along x or y direction.

$$\boldsymbol{R}_{s'}^{TO1} = \begin{pmatrix} 0 & 0 & 0 \\ 0 & 0 & 1 \\ 0 & 1 & 0 \end{pmatrix} A_{x'} + \begin{pmatrix} 0 & 0 & 1 \\ 0 & 0 & 0 \\ 1 & 0 & 0 \end{pmatrix} A_{y'} + \begin{pmatrix} 0 & 1 & 0 \\ 1 & 0 & 0 \\ 0 & 0 & 0 \end{pmatrix} A_{z'}. \tag{6.23}$$

$$\boldsymbol{R}_{s'}^{TO2} = \begin{pmatrix} 0 & 0 & 0 \\ 0 & 0 & 1 \\ 0 & 1 & 0 \end{pmatrix} y_{x'} + \begin{pmatrix} 0 & 0 & 1 \\ 0 & 0 & 0 \\ 1 & 0 & 0 \end{pmatrix} y_{y'} + \begin{pmatrix} 0 & 1 & 0 \\ 1 & 0 & 0 \\ 0 & 0 & 0 \end{pmatrix} y_{z'}. \tag{6.24}$$

Putting Eq. (6.21) – (6.24) together, we obtain the Raman LO and TO antenna models as:

$$I_s^{Ram,LO} \propto \left| \begin{pmatrix} cos\theta \\ sin\theta \\ 0 \end{pmatrix} \cdot \begin{pmatrix} Q_{\parallel} & 0 & 0 \\ 0 & Q_{\perp} & 0 \\ 0 & 0 & 0 \end{pmatrix} \cdot \boldsymbol{T}^{-1} \cdot \boldsymbol{R}_{s'}^{LO} \cdot \boldsymbol{T} \cdot \begin{pmatrix} Q_{\parallel} & 0 & 0 \\ 0 & Q_{\perp} & 0 \\ 0 & 0 & 0 \end{pmatrix} \cdot \begin{pmatrix} cos\theta \\ sin\theta \\ 0 \end{pmatrix} \right|^2, \tag{6.25}$$

$$I_s^{Ram,TO} \propto \left|\begin{pmatrix} cos\theta \\ sin\theta \\ 0 \end{pmatrix} \cdot \begin{pmatrix} Q_{\parallel} & 0 & 0 \\ 0 & Q_{\perp} & 0 \\ 0 & 0 & 0 \end{pmatrix} \cdot \boldsymbol{T}^{-1} \cdot \boldsymbol{R}_{s'}^{TO1} \cdot \boldsymbol{T} \cdot \begin{pmatrix} Q_{\parallel} & 0 & 0 \\ 0 & Q_{\perp} & 0 \\ 0 & 0 & 0 \end{pmatrix} \cdot \begin{pmatrix} cos\theta \\ sin\theta \\ 0 \end{pmatrix}\right|^2 +$$

$$\left|\begin{pmatrix} cos\theta \\ sin\theta \\ 0 \end{pmatrix} \cdot \begin{pmatrix} Q_{\parallel} & 0 & 0 \\ 0 & Q_{\perp} & 0 \\ 0 & 0 & 0 \end{pmatrix} \cdot \boldsymbol{T}^{-1} \cdot \boldsymbol{R}_{s'}^{TO2} \cdot \boldsymbol{T} \cdot \begin{pmatrix} Q_{\parallel} & 0 & 0 \\ 0 & Q_{\perp} & 0 \\ 0 & 0 & 0 \end{pmatrix} \cdot \begin{pmatrix} cos\theta \\ sin\theta \\ 0 \end{pmatrix}\right|^2 \tag{6.26}$$

By applying the $Q_{\parallel}$ and $Q_{\perp}$ obtained from fitting the Rayleigh antenna pattern into Eq. (6.15), and trying different values for angle β, we are able to find the most appropriate parameter β which leads to the best match for the antenna patterns from Eq. (6.25) and (6.26) with the experimental Raman LO and TO antenna patterns.

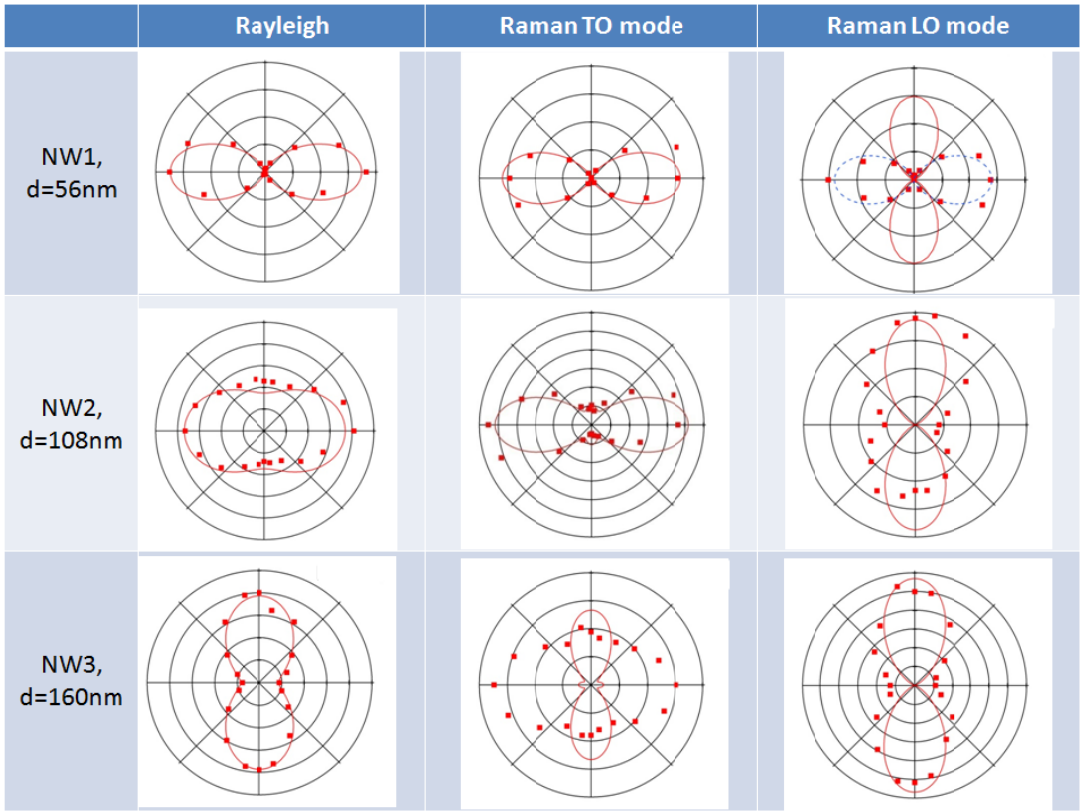

Figure 6-5: Selected results of fitting Raman antenna patterns with experimental Rayleigh antenna patterns' data. All nanowires are grown along [111].

Figure 6-5 selects Rayleigh and Raman antenna patterns from three nanowires. All three nanowires' axes are along the [111] direction. In the first column, we display the Rayleigh antenna patterns and fits to the pattern using Eq. (6.15). In the second and third columns, we show the Raman patterns and the best fits we can obtain by adjusting angle β, and using $Q_{\parallel}$ and $Q_{\perp}$ from Eq. (6.15). For nanowires with diameter smaller than 90 nm, experiments show that Rayleigh, LO and TO Raman antenna patterns are all horizontal dipoles. Our model fails for the Raman LO mode, because it predicts a vertical dipole as long as the nanowire axis is along the [111] direction. With increasing diameter, the Rayleigh antenna pattern gradually changes to a vertical dipole until the diameter becomes 160 nm. The predictions for the Raman LO and TO mode from our model are mostly correct with the exception of the TO mode when the diameter is 160 nm.

6.3.3 Fitting Rayleigh and Raman Antenna Patterns with Computed Enhancement Tensor

In this section, I will discuss how to obtain the computed enhancement tensor $\boldsymbol{Q}$ by DDA, Mie theory and FDTD methods.

In the DDA calculation, a plane electromagnetic wave is incident on a finite cylinder as shown in Figure 6-6 (a). We use the software DDSCAT 6.1 to obtain the electric field distribution $\vec{E}(\vec{r})$ within the cylinder, and define:

$$(Q_{DDA}^{in})^2 = \frac{\int_{Cylinder} |\vec{E}(\vec{r})|^2 dV}{{E_0}^2 V}, \tag{6.27}$$

where E_0 is the amplitude of the incident plane wave, V is the volume of the cylinder.

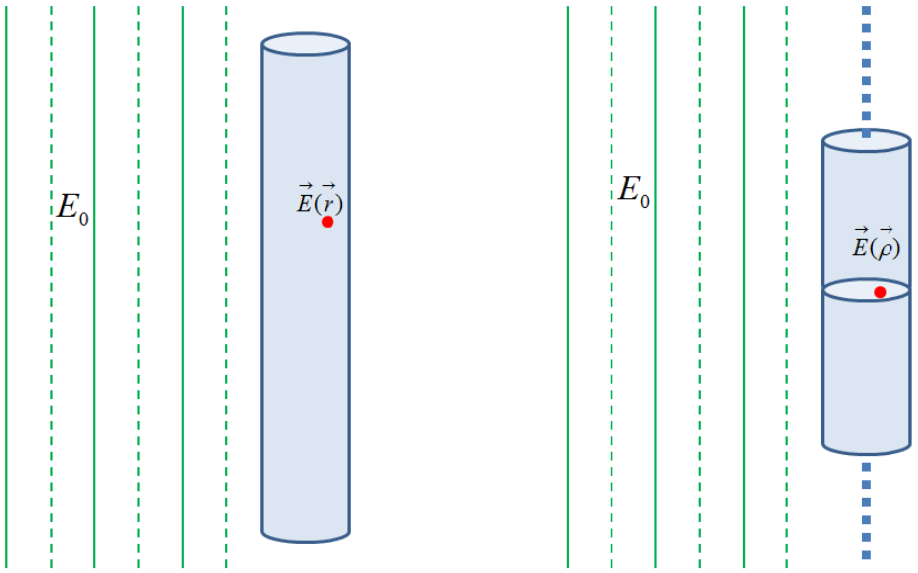

(a) Finite cylinder in DDA

(b) Infinite long cylinder in Mie theory. Cylindrical polar coordinate system.

Figure 6-6: Illustration of setups in (a) DDA and (b) Mie theory for computation of enhancement tensor.

For the Mie theory method, referring to Figure 6-6 (b), we define:

$$(Q_{Mie}^{in})^2 = \frac{\int_{\rho \le R} |\vec{E}(\vec{\rho})|^2 dA}{{E_0}^2 \pi R^2}, \tag{6.28}$$

where R is the radius of the infinitely long cylinder.

With the polarization of the incident wave parallel or perpendicular to the nanowire axis, we can obtain $(Q_{\parallel}^{in})^2$ and $(Q_{\perp}^{in})^2$. Further, we still take the approximation proposed by Linyou Cao and Bahram Nabet in Ref. [40] that $(Q_{\parallel}^{in})^2 = (Q_{\parallel}^{out})^2 = (Q_{\parallel})^2$ and $(Q_{\perp}^{in})^2 = (Q_{\perp}^{out})^2 = (Q_{\perp})^2$. The parameter which determines the shape of an antenna pattern is not $(Q_{\parallel})^2$ or $(Q_{\perp})^2$ alone, but $(Q_{\parallel}/Q_{\perp})^2$ instead. Therefore, we will

focus our discussions on $(\frac{Q_\parallel}{Q_\perp})^2_{DDA}$, $(\frac{Q_\parallel}{Q_\perp})^2_{Mie}$ for DDA and Mie theory method. Eq. (6.15) can be rewritten as:

$$I_s^{Ray} \propto (\frac{{Q_\parallel}^2}{{Q_\perp}^2} cos^2\theta + sin^2\theta)^2 \tag{6.29}$$

In the Mie theory method, we only have one variable – the diameter D and can obtain the relation between $(Q_\parallel/Q_\perp)^2$ and the diameter D. However, in the DDA method, besides the variable D, we also need to make a choice for the length of the cylinder. Should it be the whole length of the nanowire, such as D = 10 microns, or only part of the nanowire illuminated by the incident light, such as D = 1 micron? For the DDA work carried out early in our group [41], research were conducted using 488 nm incident plane wave and 2 microns long cylinder. Due to the uncertainty in choosing the correct length for DDA computation discussed above, we haven't done much DDA work since then and have only limited results for 514 nm incident light. Therefore, for DDA calculation, I cite our published results from the 2 micron long cylinder with 488nm incident excitation. In Ref. [41], we compared the $(\frac{Q_\parallel}{Q_\perp})^2_{DDA}$ to the $(\frac{Q_\parallel}{Q_\perp})^2_{Mie}$ and plotted both in a graph similar as Figure 6-7. The results from DDA and Mie theory share a lot of features, but we have a strong unique peak from DDA when the diameter of the nanowire is around 85 nm. This peak is most likely due to the resonance along nanowire axis when the polarization is parallel to the axis, because from experimental Rayleigh data and Eq. (6.29), $(Q_\parallel/Q_\perp)^2$ for D = 92 nm is about 3.36. All fitted $(Q_\parallel/Q_\perp)^2$ from Eq. (6.29) will be shown later in this chapter, together with $(\frac{Q_\parallel}{Q_\perp})^2_{Mie}$, and $(\frac{Q_\parallel}{Q_\perp})^2_{FDTD}$.

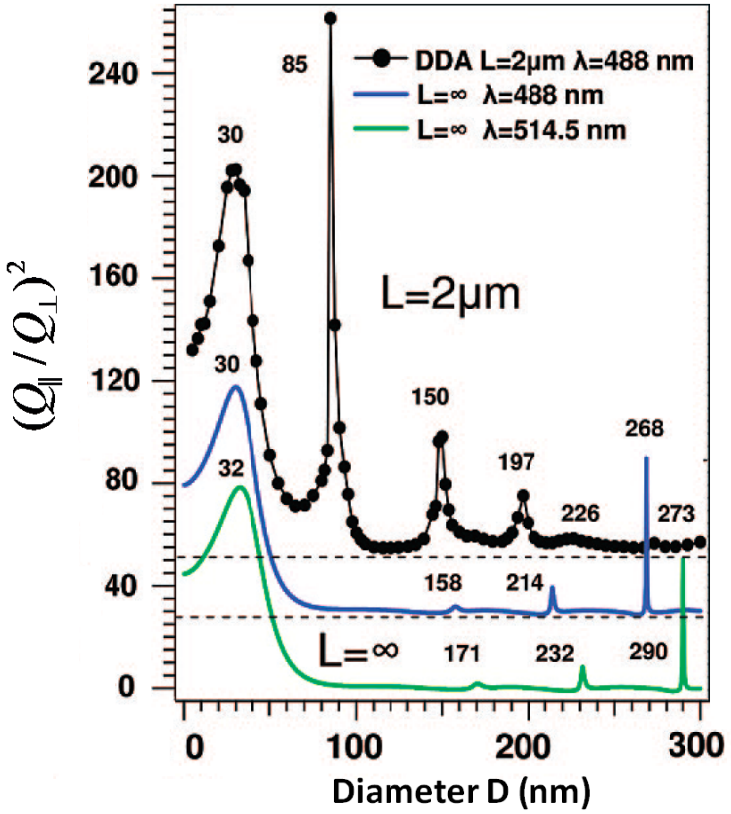

Figure 6-7: Ratio of parallel and perpendicular enhancement factor as a function of nanowire diameter, obtained by DDA and Mie theory. Peak positions are labeled in the graph [41].

To apply the FDTD method, we use setup illustrated in Figure 6-8. In FDTD, it is not necessary to make the assumption that $Q^{in} = Q^{out}$, because we are able to obtain the Q^{out}. To obtain the Q^{in}, referring to Figure 6-8 (a), we have a GaP nanowire with 180nm diameter in the region $\{(x, y, z)| -4000 \leq x \leq 4000, (z-115)^2 + y^2 \leq 90^2\}$. All numerical values are in unit of nm. The incoming 514nm laser is incident at the center of the nanowire, and has the Gaussian form:

$$I(x, y, z) = I_0(\frac{\omega_0}{\omega(z)})^2 \exp\left(-\frac{2(x^2+y^2)}{\omega^2(z)}\right). \tag{6.30}$$

The setup has the laser focused at z = 5nm, and the waist size is

$$\omega_0 = \omega(z = 5nm) = 663nm. \tag{6.31}$$

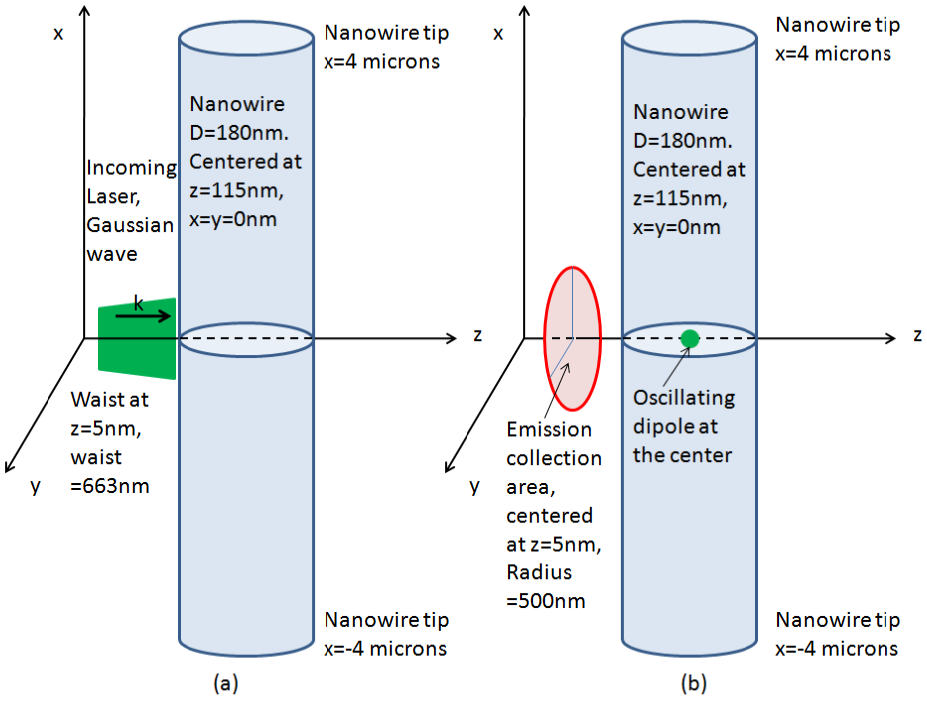

Figure 6-8: One setup in FDTD method to calculate (a) ratio of parallel to perpendicular enhancement factor $Q_{\parallel}^{in}/Q_{\perp}^{in}$ and (b) ratio of parallel to perpendicular enhancement factor $Q_{\parallel}^{out}/Q_{\perp}^{out}$. The graph is not drawn to scale.

The numerical value for the waist size is chosen according to the optical devices we used in experiments and Ref. [8]. We usually refer our micro-Raman experiments having a laser spot around 1 micron in diameter and this statement is close to the laser waist size we used in this FDTD calculation. To simplify this problem, we assume most electric fields are concentrated with the 1 micron diameter spot, and our micro-Raman system is in perfect confocal position so that we only collect Raman scattering from that 1 micron diameter spot's volume. We define this volume inside the nanowire as:

$$VOL = \{(x, y, z) | (z - 115)^2 + y^2 \leq 90^2, x^2 + y^2 \leq 500^2\}. \quad (6.32)$$

Now, the ratio of parallel to perpendicular enhancement factor $Q_{\parallel}^{in}/Q_{\perp}^{in}$ is defined as:

$$(\frac{Q_{\parallel}^{in}}{Q_{\perp}^{in}})^2 = \frac{\int_{VOL} |\vec{E}_{\parallel}|^2 dV}{\int_{VOL} |\vec{E}_{\perp}|^2 dV}. \quad (6.33)$$

We run the FDTD simulation twice, once with the polarization of the incident laser parallel to the nanowire axis and then with the polarization perpendicular to the nanowire axis, and afterwards, we can evaluate Eq. (6.33).

Figure 6-8 (a) is only one of many setups we used to evaluate Eq. (6.33). Nanowires with other diameters have the setups similar to Figure 6-8 (a). The details are listed in Table 6-1. The profile of the incident laser is the same for all the nanowires.

Laser Plane	5	=z	All unites are in nm		
Diameter	NW Center	Simulation Region -- Max Z	Simulation Region ---y ~ +y	grid size in y, z direction	grid size in x direction
50	50	85	45	2.5	10
60	55	95	50	2.5	10
70	60	105	55	2.5	10
80	65	115	60	2.5	10
90	70	125	65	2.5	10
100	75	135	70	2.5	10
110	80	145	75	5	10
120	85	155	80	5	10
130	90	165	85	5	10
140	95	175	90	5	10
150	100	185	95	5	10
160	105	195	100	5	10
170	110	205	105	5	10
180	115	215	110	5	10
190	120	225	115	5	10
200	125	235	120	5	10
	=Laser Plane + 20nm + Radius	=Center + Radius + 20nm	=Radius+20nm		

Table 6-1: Detailed setups for nanowires with different diameters in calculating $Q_{\parallel}^{in}/Q_{\perp}^{in}$ by FDTD.

To obtain the $Q_{\parallel}^{out}/Q_{\perp}^{out}$, we use the setup illustrated in Figure 6-8 (b). The nanowire is at the same position as the nanowire in Figure 6-8 (a). Here, instead of placing an incident Gaussian wave, we have an oscillating point dipole at the center of the nanowire. Since we have already assumed the perfect confocal setup, only emitted field passing through the red circular collection area in Figure 6-8 (b) can propagate further into the CCD. That collection area has a diameter of 1 micron, same as laser spot size, and should be right outside the nanowire. However, in order to avoid any possible computational effect from the nanowire-environment interface, we always place that area 20nm away from the surface of the nanowire, independent on the diameter of that nanowire. Therefore, that area for D = 180nm nanowire as depicted in Figure 6-8 (b) is:

$$ColA = \{(x, y, z)|z = 5, x^2 + y^2 \leq 500^2\}. \tag{6.34}$$

We can define the $Q_{\parallel}^{out}/Q_{\perp}^{out}$ as:

$$(\frac{Q_{\parallel}^{out}}{Q_{\perp}^{out}})^2 = \frac{\int_{ColA}|\vec{E}_{\parallel}|^2 dA}{\int_{ColA}|\vec{E}_{\perp}|^2 dA}. \tag{6.35}$$

By running the simulation twice, once with the dipole source oscillating along nanowire axis, and the other time with the dipole oscillating perpendicular to the nanowire axis, we are able to evaluate Eq. (6.35). Do the same for all other nanowires with different diameter, and we can have the $Q_{\parallel}^{out}/Q_{\perp}^{out}$ as a function of nanowire diameter.

With the computed $Q_{\parallel}/Q_{\perp}$ from Mie theory, we are able to fit Rayleigh and Raman patterns using Eq. (6.29), (6.25) and (6.26). To use FDTD method, we need to

change Eq. (6.29), (6.25) and (6.26) a little to reflect the idea that $Q_{\parallel}^{in}/Q_{\perp}^{in}$ is not the same as $Q_{\parallel}^{out}/Q_{\perp}^{out}$.

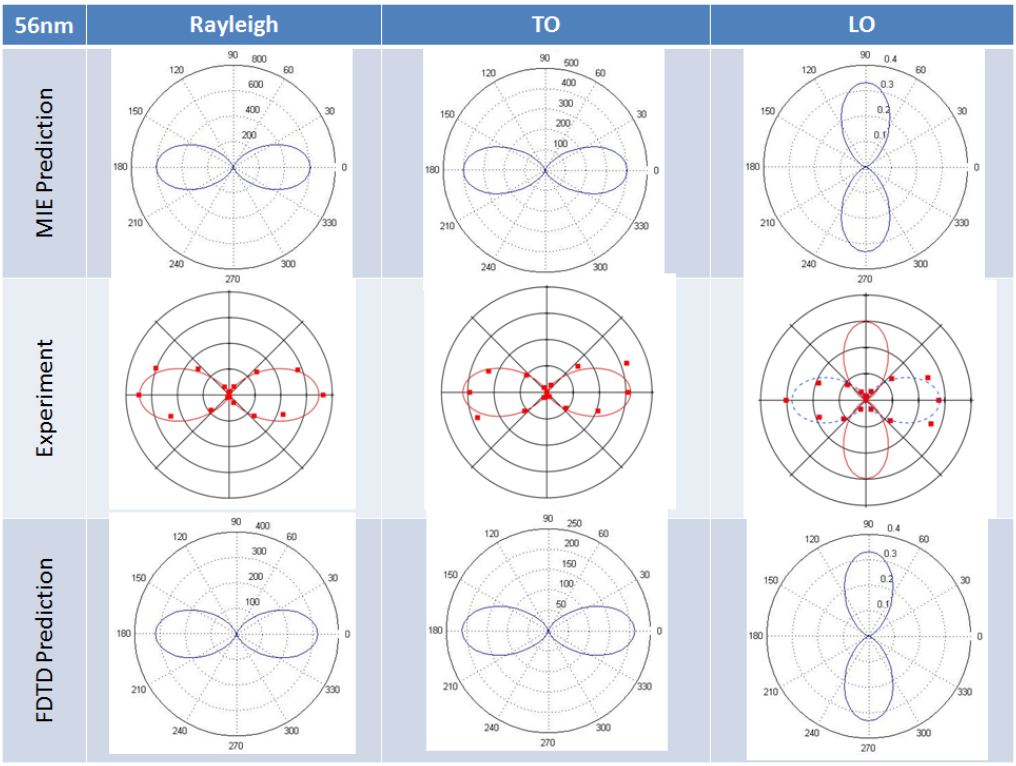

Figure 6-9: Fitting Rayleigh and Raman antenna patterns using computed ratio of parallel to perpendicular enhancement factor for one GaP nanowire with 56nm diameter.

Figure 6-9 to Figure 6-11 depicts fits to Rayleigh and Raman antenna patterns by use of the computed $Q_{\parallel}/Q_{\perp}$ in this section by Mie theory and FDTD method. In each figure, the second row shows experimental results (red dots). The smooth red curves in the second row are the fits using experimental Rayleigh data which we have discussed in the previous section. The first columns in the first and third rows are predictions for Rayleigh antenna patterns from computed $Q_{\parallel}/Q_{\perp}$ by Mie theory and FDTD method,

respectively, without any reference to the experimental Rayleigh antenna patterns. However, in making predictions for Raman LO and TO antenna patterns, we refer to the experimental antenna patterns in order to adjust the angle β so that our prediction will match the experimental pattern to the best extent.

Regarding the nanowire with diameter of 56nm, fitting using the Mie, FDTD and Rayleigh methods gives similar results. All three methods fail for the Raman LO mode. One possible explanation is that for nanowires with extremely high aspect ratio, the Raman tensor has a minor effect in Raman scattering and therefore Raman intensity is determined mainly by electric field inside nanowires.

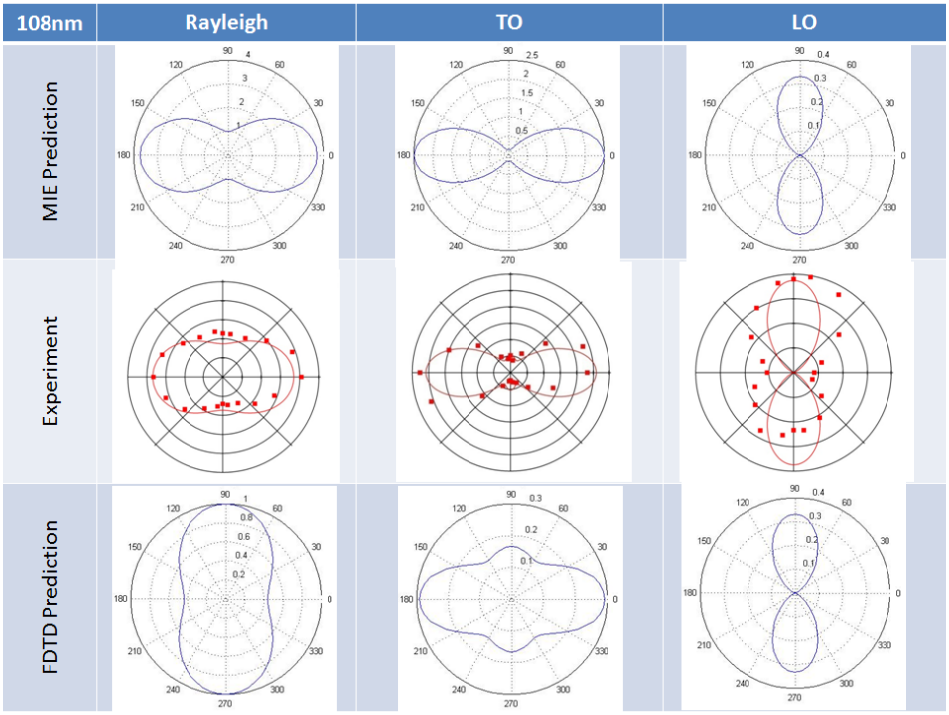

Figure 6-10: Fitting Rayleigh and Raman antenna patterns using computed ratio of parallel to perpendicular enhancement factor for one GaP nanowire with 108nm diameter.

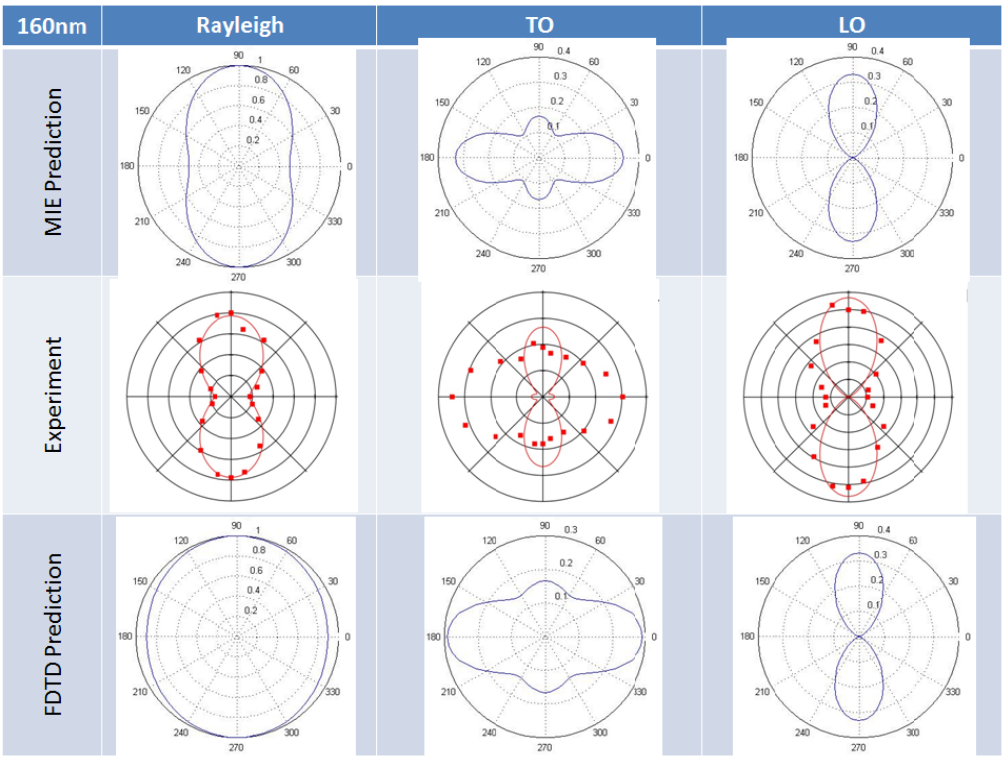

Figure 6-11: Fitting Rayleigh and Raman antenna patterns using computed ratio of parallel to perpendicular enhancement factor for one GaP nanowire with 160nm diameter.

In Figure 6-10, shows the fits using Mie theory and Rayleigh data work equally well, and predictions from the FDTD method are worse than the other two. Figure 6-11 suggests that we have a trade-off between Rayleigh and TO mode in Raman for all three fitting methods, and we cannot reach a firm conclusion which method makes the best predictions for this nanowire.

6.4 Discussion and Conclusion

By checking fits or predictions for three nanowires in the previous section, we find that the FDTD method yields unsatisfactory results. Here, we further investigate the difference among these three methods by focusing on $(\frac{Q_\parallel}{Q_\perp})^2_{Mie}$, $(\frac{Q_\parallel^{in}}{Q_\perp^{in}})^2_{FDTD}$, $(\frac{Q_\parallel^{out}}{Q_\perp^{out}})^2_{FDTD}$, and $(\frac{Q_\parallel}{Q_\perp})^2_{Rayleigh}$ from Eq. (6.28), (6.33), (6.35) and (6.29) respectively.

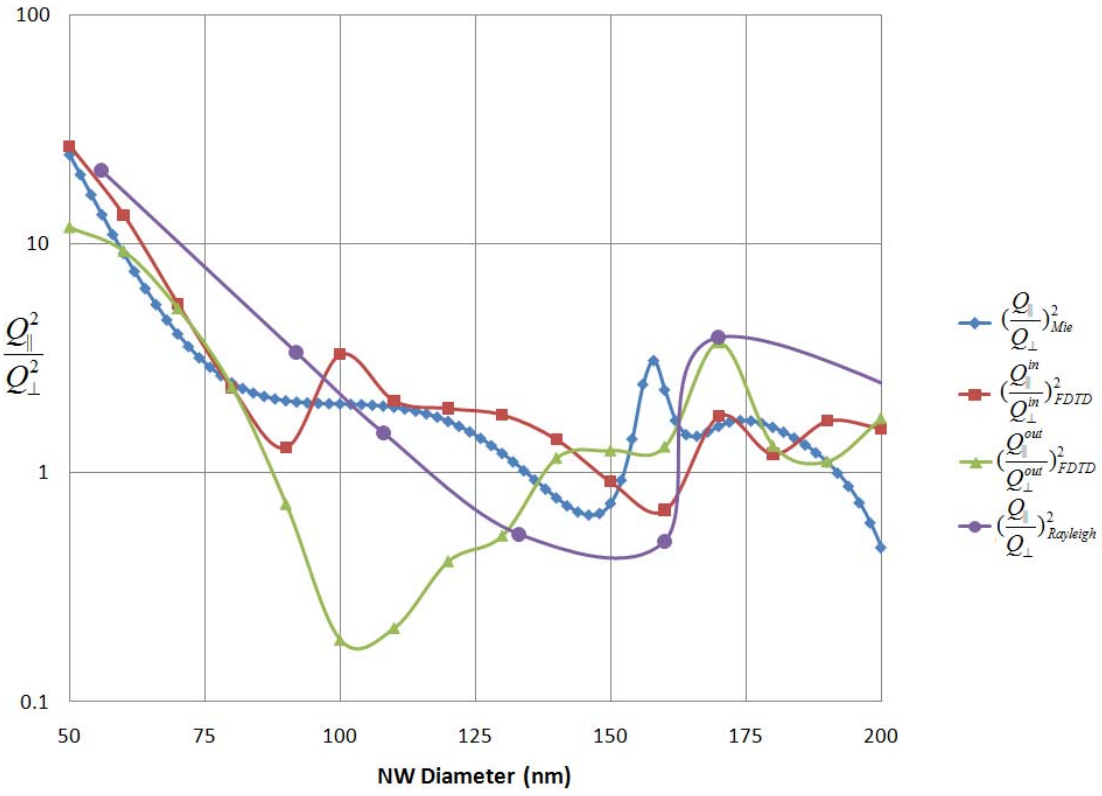

Figure 6-12: Log-linear scale of $(Q_\parallel/Q_\perp)^2$ vs. nanowire diameter, obtained in four different ways.

The four different $(Q_{\parallel}/Q_{\perp})^2$ are plotted in a log-linear scale in Figure 6-12. $(\frac{Q_{\parallel}^{in}}{Q_{\perp}^{in}})^2_{Rayleigh}$ and $(\frac{Q_{\parallel}^{in}}{Q_{\perp}^{in}})^2_{Mie}$ yield the close answers for most of the nanowires measured except the one with diameter of 160nm. This result implies that the large solid collection angle arising from the use of 100x 0.95N.A. lens does not have a significant effect on our polarized Raman experiments, since $(\frac{Q_{\parallel}^{in}}{Q_{\perp}^{in}})^2_{Mie}$ represents the result from considering straight back scattering only while $(\frac{Q_{\parallel}^{in}}{Q_{\perp}^{in}})^2_{Rayleigh}$ contains information from stray scattering collected by the lens. The effect from large collection angle of the lens is limited by the small back aperture of the lens together with restricting CCD collection area to minimize the stray light.

In Figure 6-12, $(\frac{Q_{\parallel}^{out}}{Q_{\perp}^{out}})^2_{FDTD}$ exhibits different behavior than the other three and we find that the greatest discrepancy between $(\frac{Q_{\parallel}^{out}}{Q_{\perp}^{out}})^2_{FDTD}$ and the others occurs when the diameter of the nanowire is around 100nm. This is the case when the FDTD method fails in Figure 6-10. This discrepancy, or this failure, comes from our over-simplified model to compute $(\frac{Q_{\parallel}^{out}}{Q_{\perp}^{out}})^2_{FDTD}$.

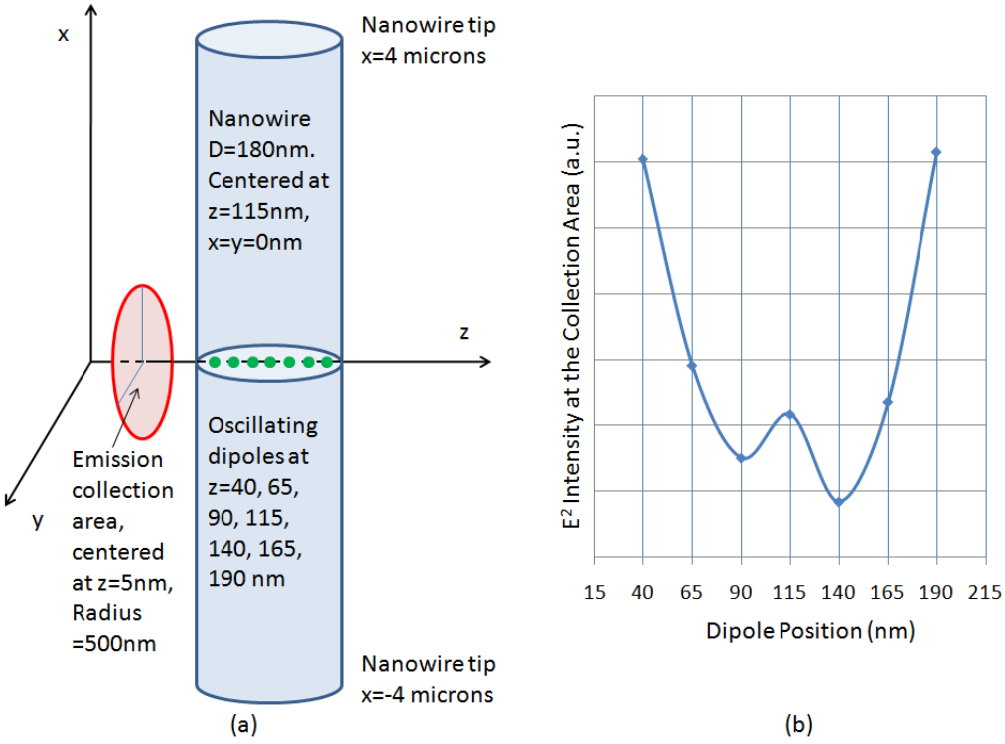

Figure 6-13: (a) configurations to test emission efficiency from 7 oscillating dipoles; (b) emission intensity at collection area from each oscillating dipole alone.

Figure 6-13 (a) has the similar setup as the configuration we use to compute $(\frac{Q_{\parallel}^{out}}{Q_{\perp}^{out}})_{FDTD}^{2}$. However, instead of placing a single point dipole at the center of the nanowire, we use 7 point dipoles now. The 7 dipoles are located all on the z axis and have their z positions labeled on the figure. To evaluate each dipole's contribution to the total emission received at the collection area, we run the simulation with one dipole exists at a time. Afterwards, we obtain the $\int_{ColA} |E_{\parallel}|^2 dA$ at the collection area for each dipole and plot them in Figure 6-13 (b). This figure clearly shows that the dipoles near the surface are more efficient in radiating into the collection area than the dipoles at or near

the nanowire axis, at least for nanowires with this diameter. Therefore, it is inappropriate to simplify emission from the nanowire to the radiation from one single dipole at the center of the nanowire. If we assume $(\frac{Q_{\parallel}^{out}}{Q_{\perp}^{out}})_{FDTD}^{2} \approx (\frac{Q_{\parallel}^{in}}{Q_{\perp}^{in}})_{FDTD}^{2}$ as what we do for Mie and Rayleigh method, we will expect FDTD method yield a close pattern to the other two, because $(\frac{Q_{\parallel}^{in}}{Q_{\perp}^{in}})_{FDTD}^{2}$ is in a reasonable agreement with Mie and Rayleigh method in Figure 6-12.

The FDTD simulation also reveals an interesting fact that Raman or Rayleigh scattering mostly comes from the near surface and far surface of the nanowire. The results in Figure 6-14 (a) and (b) are obtained from setup in Figure 6-8 (a). The polarization of incoming laser is parallel to the nanowire axis and the volume of laser spot is defined in Eq. (6.32). Figure 6-14 (a) illustrates that the average internal electric field is greatest at the near and far surface of the nanowire relative to the incoming laser. Figure 6-14 (b) is the summation of internal electric field according to their z coordinates. Figure 6-14 (c) is the product of Figure 6-13 (b) and 7 points in Figure 6-14 (b), which clearly identifies the far and near surface of the nanowire as two main contributors to the Raman scattering.

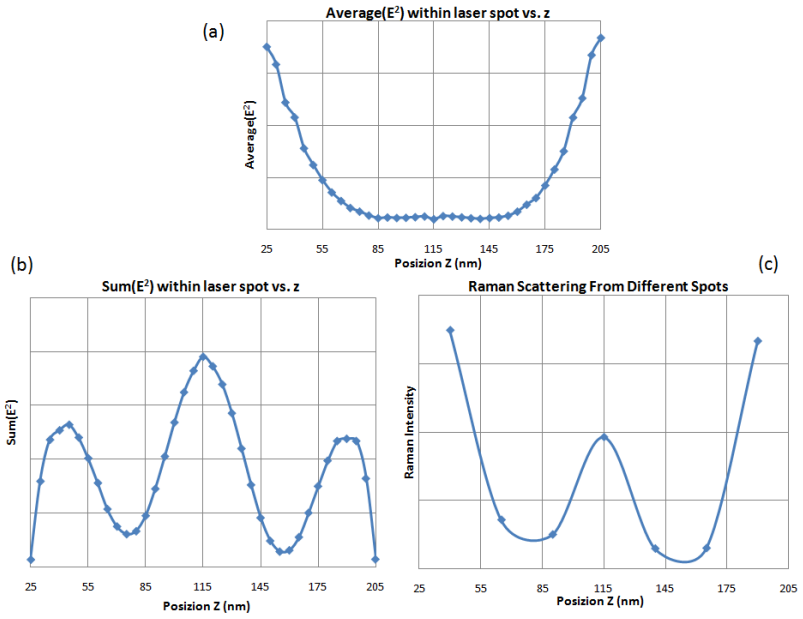

Figure 6-14: (a) Average and (b) sum of E^2 within the laser spot as a function of position z; (c) illustration of strong Raman scattering from near and far surface of the nanowire.

This finding of unequal contribution to Raman and Rayleigh scattering challenges our simplified volume average Q^{in} used in the Mie method. However, FDTD simulation that take into account the different efficiency in Raman scattering from different parts of the nanowire are computationally unrealistic. This chapter ends here with reasonable agreement between the Mie and Rayleigh predictions for Raman antenna patterns and the actual experimental results. The discrepancies might come from using average Q^{in} and assuming $Q^{in} = Q^{out}$.

Chapter 7

Hot Tip Effect in GaP Nanowires

7.1 Introduction to Hot Tip Effect

The so called "Hot Tip Effect" in nanowires was discovered in the Eklund group. When we collect Raman scattering from different parts of a GaP nanowire, in most cases, the scattering intensity is strongest at the two tips of the nanowire.

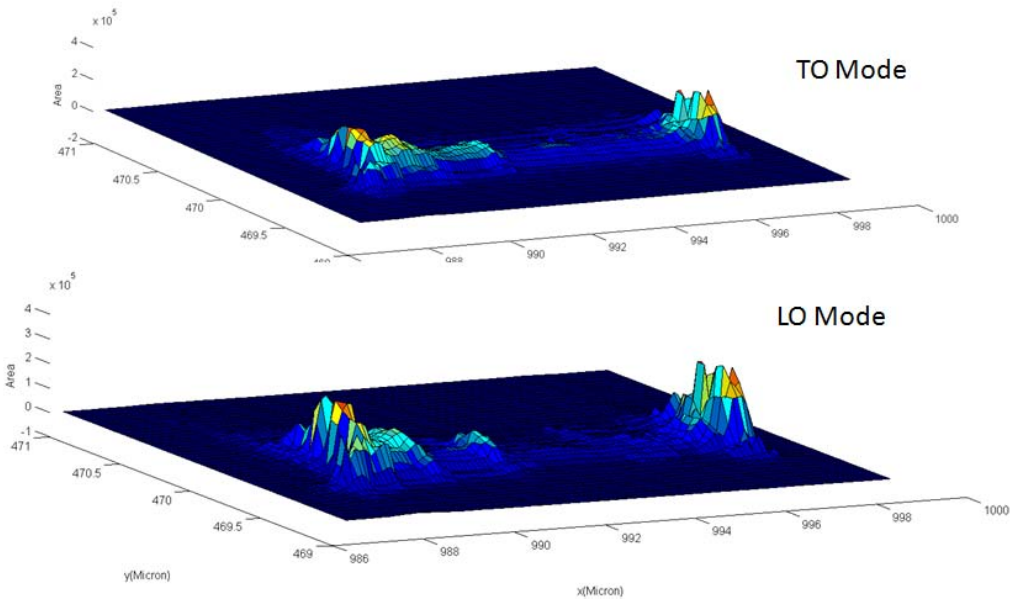

Figure 7-1: Map of Raman scattering intensity from different parts of a GaP nanowire measured on Si substrate with 514.5nm excitation.

Figure 7-1 is a map of Raman LO and TO mode intensity measured from different parts of a GaP nanowire on a Si substrate. The positions for the two peaks in each Raman intensity map coincide with the locations of the two tips of the nanowire. The ratio of

Raman intensity at one tip to the intensity from the center is about 5 ~ 6 from the above figure. Since we have s gold particle only at one tip of the nanowire, this hot tip effect must be due to reasons other than the enhanced Raman scattering near a metal surface. The detailed experimental procedures for such measurements will be discussed below.

7.2 Hot Tip Effect: Experimental Procedures for GaP Nanowires on Si Substrates

The GaP nanowires we studied in this section were fabricated by PLV, and the growth conditions were discussed in detail in Chapter 2.3. We took some GaP nanowire samples, put them in isopropanol alcohol, mildly sonicated for 30 seconds to break nanowire bundles into isolated nanowires, and dropped the solutions onto a Si substrate. The Raman measurements were performed using the Renishaw InVia micro-Raman system.

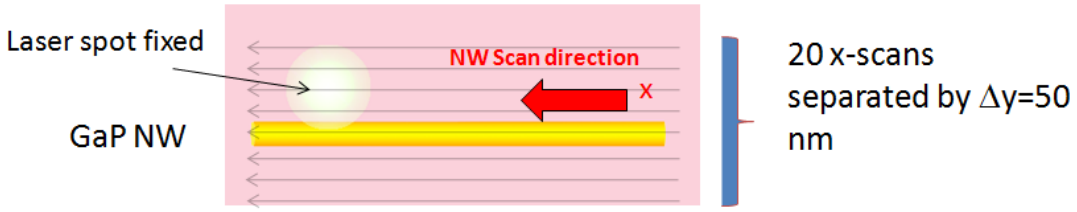

Figure 7-2: 2D map scan setup for tip effect.

The Si substrate containing GaP nanowires is mounted on a computer-controlled sample stage in the Renishaw InVia micro-Raman system. Figure 7-2 illustrates how the sample stage moves to map the Raman scattering intensity. The laser spot is fixed and the

sample stage is free to move in x and y directions. A typical 2D map scan includes 20 x-scans, each separated by 50 nm apart. In each x-scan, the stage moves from right to left as indicated by grey arrows in Figure 7-2, and the step between two positions where we take Raman measurements in one x-scan is 100 nm or 150 nm depending on the nanowire length.

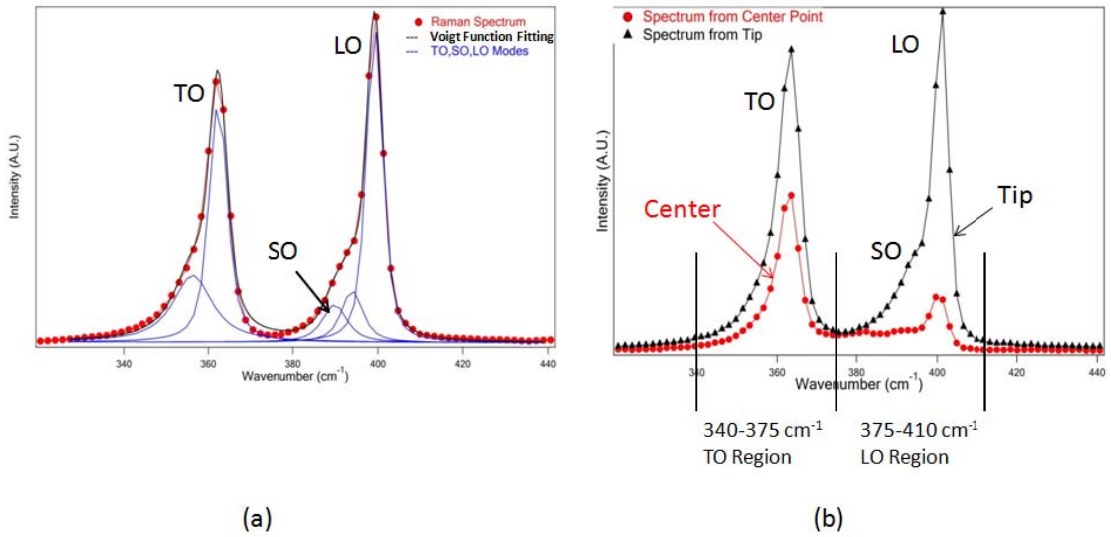

Figure 7-3: (a) Typical Raman spectrum from a GaP nanowire, including splitting LO and TO mode, and a SO mode; (b) Simplified way to obtain the area under TO mode and the area under LO+SO mode.

The overall mapping setup is like a 2D mesh covering the GaP nanowire we want to study. At each grid point of that 2D mesh, we take a Raman spectrum, such as the one shown in Figure 7-3 (a). The Raman spectrum has three modes, one splitting TO mode, one splitting LO mode and one surface optical (SO) mode [42]. However, the intensity of each mode varies a lot among the Raman spectra taken from different positions of the same nanowire. Therefore it is difficult to use auto fitting, and it is impractical to

manually fit all the spectra in a scanning map. For the study in this chapter, we use the term "TO area or LO area" to refer to the area in the TO region and the LO region labeled in Figure 7-3. The formula for the calculation is:

$$Area = \sum_{i_{min}}^{i_{max}-1}[\frac{1}{2}(y_i + y_{i+1}) \cdot |x_i - x_{i+1}|] , \quad (7.1)$$

where, the i_{min} and i_{max} is the lower and upper boundary for the TO or LO region, x is the wavenumber, and y is the intensity. Before applying Eq. (7.1), we first subtract a straight baseline from the raw Raman spectrum. After the subtraction, the Raman intensities for the first wavenumber and the last wavenumber are both zero. The TO area calculated in this way should be close to the area we would obtain if we fit the TO mode by two voigt functions (convolution of Gaussian and Lorentz functions) and then sum the areas under these two voigt curves. However, the LO area calculated in this way is actually the area under the LO mode and SO mode together. Therefore, in this study, we focus our analysis on the TO mode area. This protocol yields Raman intensity maps such as in Figure 7-1.

A simplified version of this experimental procedure is to take a 1D line scan instead of a 2D map scan. This setup is similar to the one in Figure 7-2, but the laser spot is initially on the extended line of the nanowire axis and then scanned along the nanowire axis, as the arrow right on the nanowire indicates in Figure 7-2. The line-scan is much faster than a 2D map, typical taking 20 minutes ~ 1 hour to complete one scan, compared to almost half day for a 2D map scan. However, in a line scan, we need to be assured that the scanning is along the nanowire axis. In addition, we lose information from the side edges of the nanowire.

7.3 Hot Tip Effect Results for GaP on Si Substrates

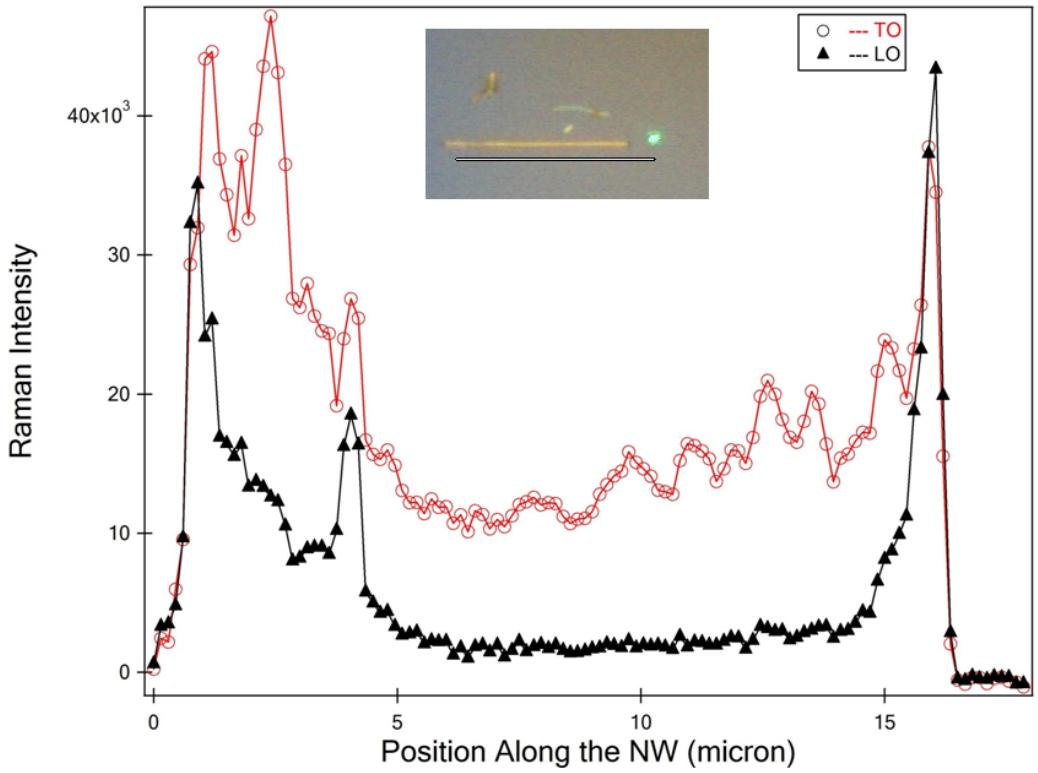

Figure 7-4: Example of hot tip effect of GaP nanowire on Si substrate with 514.5nm excitation. Inlet is microscopic image of the nanowire.

Figure 7-4 ~ Figure 7-6 display three line profile examples of GaP nanowire measured on a Si substrate. The horizontal axis records the position where we take the Raman measurement. Note that zero on the horizontal axis is not the tip of the nanowire. The vertical axis is the LO and TO area calculated as we described in the previous section.

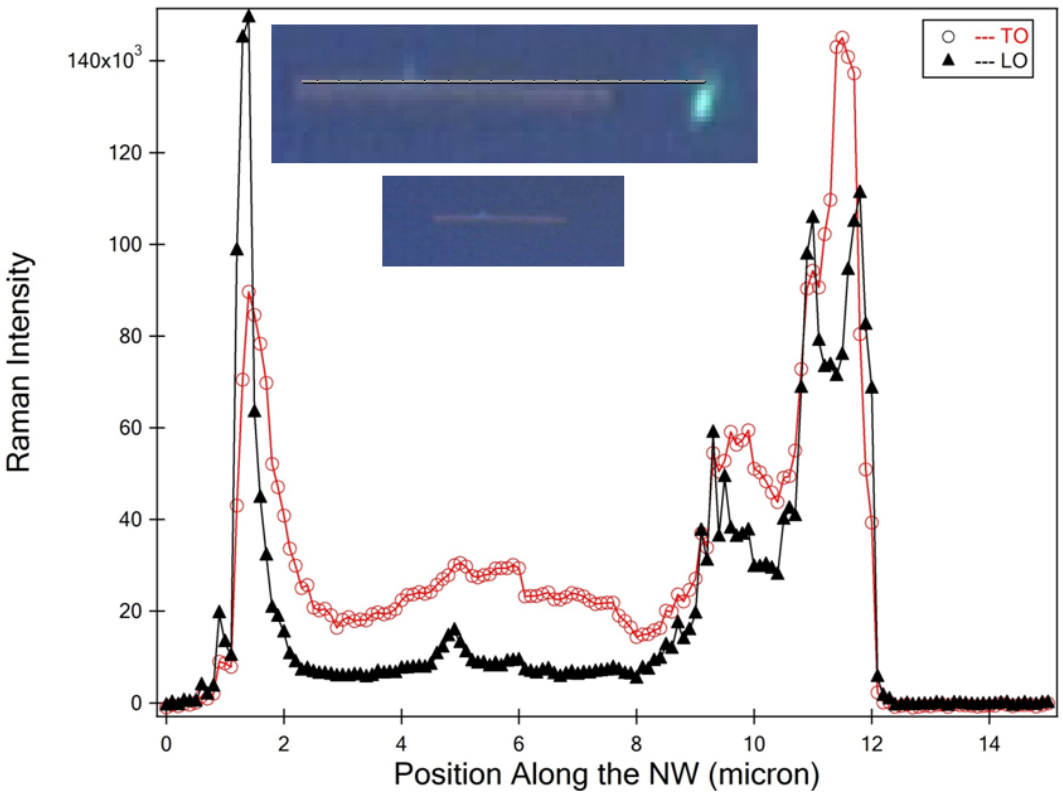

Figure 7-5: Example of hot tip effect of GaP nanowire on Si substrate with 514.5nm excitation. Inlets are microscopic images of the nanowire.

The insets in Figure 7-4 to Figure 7-6 are images taken by the microscope in the Renishaw InVia micro-Raman system. The green dots in those images are laser spots. The straight line in each image should be the scan path, but due to the imperfect calibration of the coordinates for the laser spot, the path shown on these figures are off the nanowire. In each experiment, the laser was always on the nanowire axis.

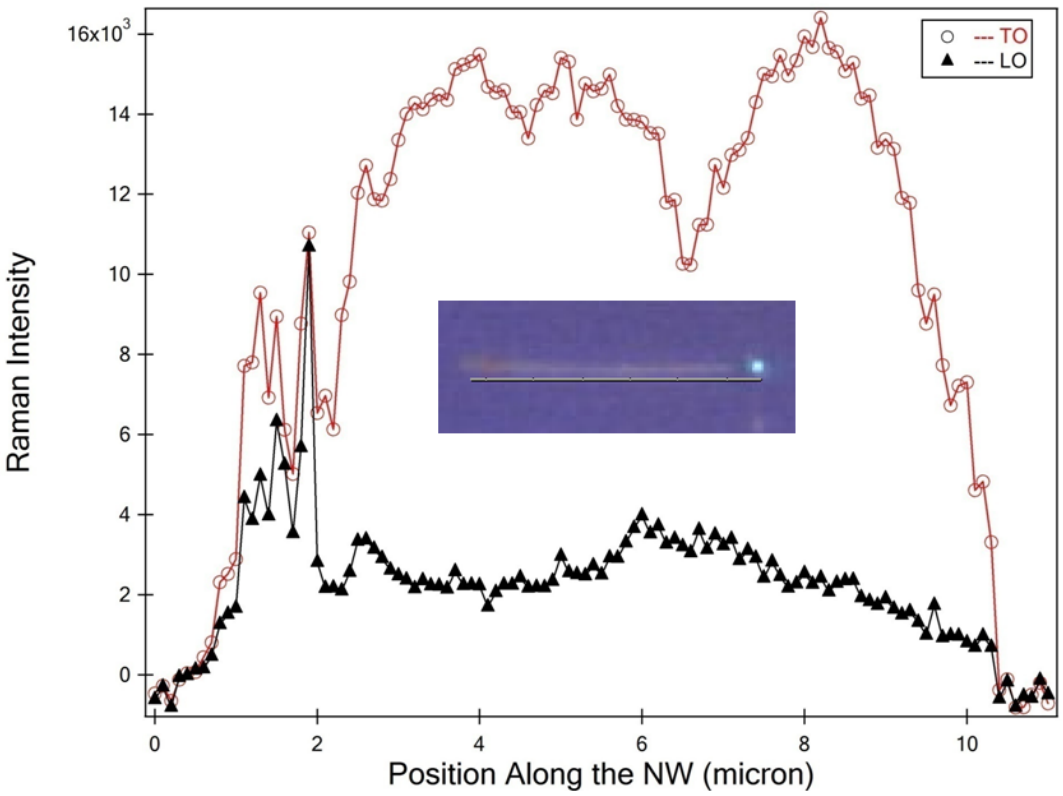

Figure 7-6: Example of non-hot tip effect of GaP nanowire on Si substrate with 514.5nm excitation. Inlets are microscopic images of the nanowire.

Figure 7-4 and Figure 7-5 shows the hot tip effect from a GaP nanowire on Si substrate, while the nanowire in Figure 7-6 does not have hot tips. In fact, for all the nanowires on Si substrate I have studied, about two-thirds of them exhibit hot tip effect. Here, we define the enhancement factor (EF):

$$EF = \frac{Min(Max(I_{tip1}),Max(I_{tip2}))}{Average(I_{center})} \quad , \tag{7.2}$$

where I_{tip1} is the intensity (TO area) around one tip, I_{tip2} is the intensity around the other tip, and I_{center} is the intensity around the nanowire center. We use the $Min()$ function here because a large enhancement may be caused by the gold particle at one tip. For most

GaP nanowires on Si substrate with hot tip effect, the enhancement factor is between 3 and 5.

Until now, we only know hot tip effect exists in most GaP nanowires on Si substrate, and the enhancement factor varies among different nanowires. In the following sections, we will study the GaP nanowires on TEM grid so that we have access to the tip geometry of each nanowire from TEM images and we are able to remove any existing effects from the interaction between the GaP nanowire and Si substrate. We will experimentally study the correlation between the hot tip effect and the profile of the incident laser, i.e., polarization and frequency of the incident laser. Further, we will simulate the hot tip effect in the classical Raman scattering realm by the FDTD method and obtain the expected enhancement factor. Afterwards, we can quantitatively judge whether a nanowire has the hot tip effect or not, by using that expected enhancement factor as a threshold to hot tip effect.

7.4 FDTD Simulation for Hot Tip Effect from GaP Nanowires

We assume that our GaP nanowire is single crystal and therefore the Raman tensors at different parts of the nanowire are the same. To study the Raman intensity in the classical realm, we only need to know how efficiently the laser enters into the nanowire and how efficiently the oscillating dipole emission can emerge from the nanowire and into the collection area.

The FDTD simulations in this chapter are very similar to the FDTD simulations in the Chapter 6. With the incident laser polarization parallel/perpendicular to the nanowire

axis, the electric field inside nanowire is almost parallel/perpendicular to the nanowire axis. When the point dipole is oscillating parallel/perpendicular to the nanowire axis, the electric fields at the collection area are also almost parallel/perpendicular to the nanowire axis. Thus, in this simulation, since the incident laser's polarization is always parallel to the nanowire axis, we only consider electric fields inside the nanowire whose polarizations are parallel to the nanowire axis, we only use point dipoles that are oscillating along the nanowire axis, and we only sum electric fields intensity at the collection area whose polarizations are parallel to the nanowire axis.

7.4.1 GaP Nanowires with Smooth Surface

In this section, our subject is a GaP nanowire with a smooth surface. It is represented by a cylinder with length L = 8 microns and diameter D = 180nm. The setup in Optiwave OptiFDTD software is illustrated in Figure 7-7 (a). The cylinder is along x axis, and the center of the nanowire is at x= y=0, and z = 180nm. The incident laser always has its focal plane at z = 20nm, but the center of the incident beam moves along the x axis. For the tip effect, we have studied the following cases: the center of laser is at x = 0, 4.0, 3.9, 3.8, 3.7, 3.6, 3.5, 3.4, 3.3 microns. Figure 7-7 (a) is the setup for laser center x = 3.4 microns. We treat the classical Raman scattering by (1) setting up internal electric field from incident laser; (2) creating oscillating dipoles from internal field; and (3) collecting electric field emissions from dipoles at the collection area. We have already shown in Chapter 6.4 that it is too simplified to use only one dipole on the nanowire axis to represent all oscillating dipoles in the laser spot, therefore Figure 7-7 (b) illustrate how

we classify electric fields into regions based on x and z coordinates, and later we are going to place one dipole (green dot) for each region.

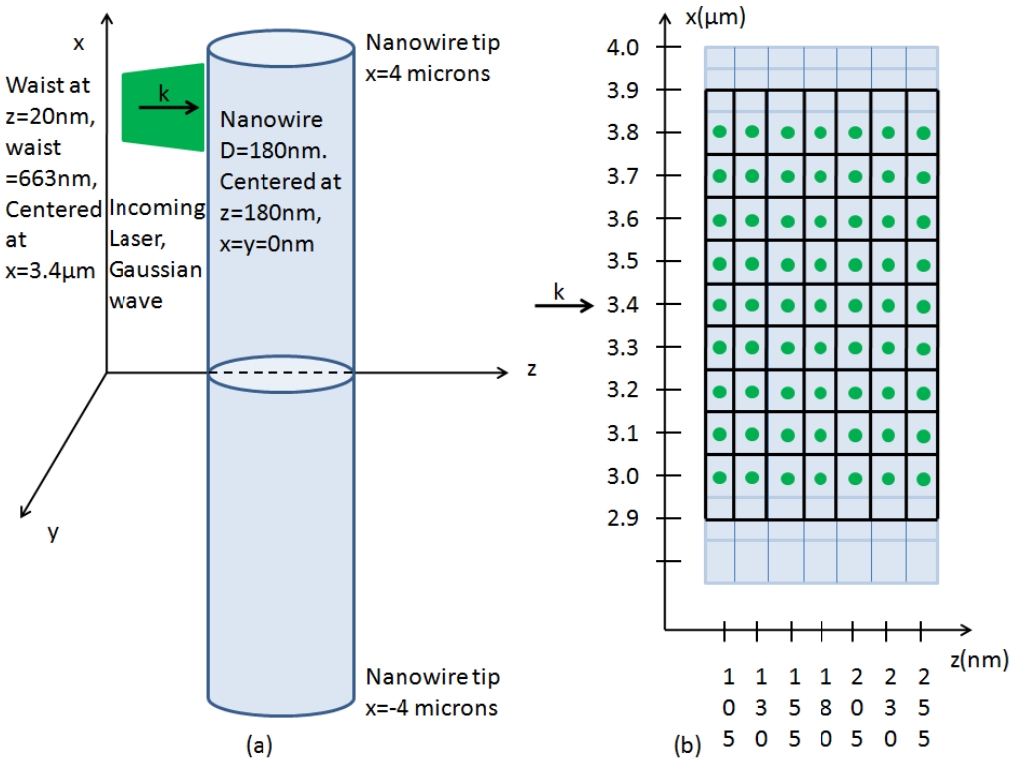

Figure 7-7: (a) one example of setups in FDTD simulation software; (b) post-simulation categorization of electric fields inside nanowire.

The same as in Chapter 6, we assume a perfect confocal condition. For internal electric field, we only investigate those within the 1 micron size laser spot. For electric field emission, we only count those electric field passing through a collection area with diameter D = 1 micron, having the same center x as the incident laser and 20nm away from the nanowire surface. Therefore, with the setup in Figure 7-7 (a), we divide the nanowire into many categories as depicted by each black rectangle in Figure 7-7 (b). The

general categorization rules are as following. First, we define the region within the laser spot:

$$VOL(LaserX) = \{(x,y,z)|(z-180)^2 + y^2 \le 90^2, (x-LaserX)^2 + y^2 \le 500^2, -4000 \le x \le 4000\}, \quad (7.3)$$

where $LaserX$ is the position of laser center x, and all numerical values are in the unit of nm. Afterwards, we only classify points within the above region. The nanowire axis is along z = 180nm, and the z_categories are always:

$$z\_category = \begin{cases} 105, if\ z < 117.5 \\ 130, if\ 117.5 \le z < 142.5 \\ 155, if\ 142.5 \le z < 167.5 \\ 180, if\ 167.5 \le z \le 192.5 \\ 205, if\ 192.5 < z \le 217.5 \\ 230, if\ 217.5 < z \le 242.5 \\ 255, if\ 242.5 < z \end{cases}. \quad (7.4)$$

The categories based on position x are:

$$x\_category = \begin{cases} LaserX - n, if\ LaserX - n - 0.05 \le x < LaserX - n + 0.05 \\ LaserX, if\ LaserX - 0.05 \le x \le LaserX + 0.05 \\ LaserX + n, if\ LaserX + n - 0.05 \le x < LaserX + n + 0.05 \end{cases}, \quad (7.5)$$

where n is any positive integer divided by 10. After Eq. (7.5), we need to modify the x_category by:

$$x\_category = \begin{cases} x - 0.4, if\ x\_category = x - 0.5 \\ 3.9, if\ x\_category = 4 \\ x + 0.4, if\ x\_category = x + 0.5 \end{cases}. \quad (7.6)$$

After the classification, we can sum the $|E_x|^2$ according to each x and z category, and assign the notations $|E_x^{in}|^2(x\_category, z\_category, LaserX)$ to them.

To study the efficiency of emissions from internal oscillating dipoles, we have the configuration depicted in Figure 7-8.

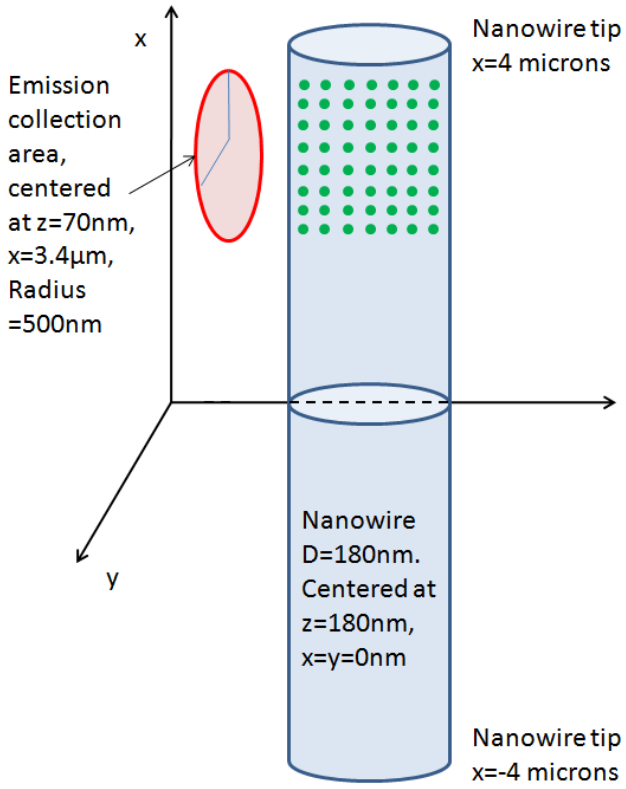

Figure 7-8: setup in FDTD simulation to compute efficiency for dipole emission.

The green dots in Figure 7-8 are oscillating dipoles. Their locations (x, y, z) are at all possible $(x\_category, 0, z\_category)$, where $x\_category$ = -0.4 to 0.4, 2.9 to 3.9 increment by 0.1, and $z\_category$ = 105 to 255 increment by 25. The red circle in the figure is the collection area, having a diameter of 1 micron, and its center is at position $(LaserX, 0, 70)$, 20nm left to the leftmost surface of the nanowire. We define the region within that circle:

$$ColA(LaserX) = \{(x, y, z) | (x - LaserX)^2 + y^2 \leq 500^2, z = 70\} . \quad (7.7)$$

This region is a function of $LaserX$, and all numerical values in Eq. (7.7) are in the unites of nm.

For each simulation run, we only place one oscillating dipole, and the output is electric fields with polarizations parallel to the nanowire axis on the plane z = 70nm. We denote these electric fields as $E_x^{out}(x, y; x\_category, z\_category)$. The Raman intensity from Eq. (6.20) can be rewritten as:

$$I_s^{Ram} \propto \left| \begin{pmatrix} 1 \\ 0 \\ 0 \end{pmatrix}^T \cdot \begin{pmatrix} Q_{\parallel}^{out} & 0 & 0 \\ 0 & Q_{\perp}^{out} & 0 \\ 0 & 0 & 0 \end{pmatrix} \cdot \boldsymbol{R}_s \cdot \begin{pmatrix} Q_{\parallel}^{in} & 0 & 0 \\ 0 & Q_{\perp}^{in} & 0 \\ 0 & 0 & 0 \end{pmatrix} \cdot \begin{pmatrix} 1 \\ 0 \\ 0 \end{pmatrix} \right|^2 . \quad (7.8)$$

Here, since we have assumed Raman tensor $\boldsymbol{R}_s$ is the same everywhere, the Raman intensity should be:

$$I_s^{Ram}(LaserX) = \sum_{x\_category, z\_category} \{ |E_x^{in}|^2 (x\_category, z\_category, LaserX) \cdot \sum_{(x,y) \in ColA(LaserX)} |E_x^{out}(x, y; x_{category}, z_{category})|^2 \} . \quad (7.9)$$

Applying Eq. (7.9) for different laser incident position $LaserX$ we have simulated, and normalizing to the Raman intensity from the center of the nanowire, i.e., $I_s^{Ram}(LaserX)/I_s^{Ram}(0)$, we obtain our FDTD simulated result in Figure 7-9. From this figure, we see that the maximal Raman intensity occurs at 500nm away from the tip. That is when the full laser spot just hits the nanowire. Figure 7-10 is a plot of maximal, and average $|E[(x, y, z) \in VOL(LaserX)]|^2 / |E[(x, y, z) \in VOL(0)]|^2$. From Figure 7-9 and Figure 7-10, as the laser spot moves from tip towards center, the average internal E^2 reaches it maximal first, followed by maximal E^2, and after these two, Raman intensity reaches its maximal. This is reasonable because the Raman intensity we observed not only depends on how efficiently incident laser excites internal dipoles and how efficiently

electric emission from internal oscillating dipoles can reach external detector, but also on the volume of the nanowire illuminated by the laser.

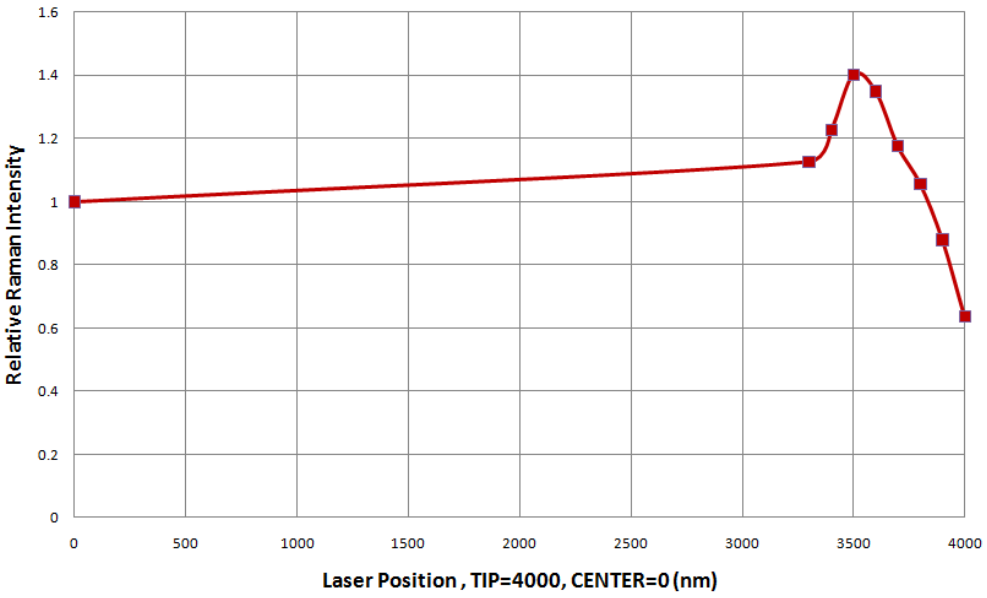

Figure 7-9: Relative Raman intensity $I_s^{Ram}(LaserX)/I_s^{Ram}(0)$ when laser incident on different positions $LaserX$ of the GaP nanowire.

The enhancement factor obtained from these FDTD simulations is 1.40, much smaller than the enhancement factor we observed in experimental results from GaP nanowires on Si substrate. The possible explanations include: (1) in experiments, we have additional enhancement from the interface of GaP nanowire and Si substrate; (2) in experiments, the GaP nanowires have surface roughness along the nanowire; (3) nanowire's diameter may play an important role in enhancement factor, and this calculated one (1.40) is only correct for nanowires whose diameters are 180nm; (4) real nanowires have more complicated structures, such as twinnings and coatings.

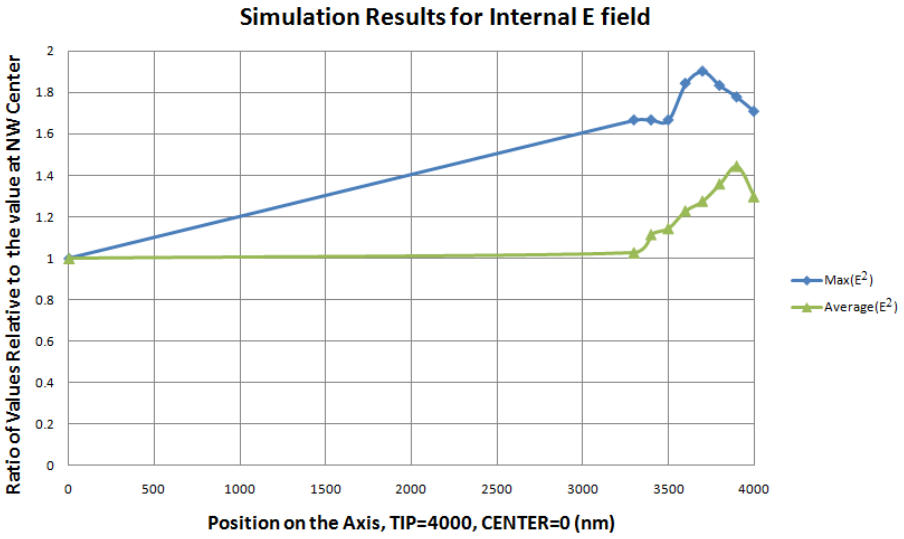

Figure 7-10: Ratio of Max and Average internal E^2 when laser is incident on the tip area to the corresponding value when laser is incident at the center of the nanowiere.

7.4.1 GaP Nanowires with Sinusoidal Surface Roughness

In the previous section, we assume our nanowires can be represented by a cylinder. Here, we take into account the surface roughness along the nanowire. Instead of a cylinder with length L = 8 microns and diameter D = 180nm, we model a nanowire with 400 small cylinders and each cylinder has a length of L = 20 nm. Referring to the coordinates in Figure 7-7 (a), the cylinder whose centers of tips locate at $(-4000 + (n-1) * 20,0,180)$ and $(-4000 + n * 20,0,180)$ has a diameter of $180 + 10cos\,(2\pi\frac{n}{20})$. All numerical values are in the unit of nm. Thus, in this model, the nanowire has a sinusoidal surface roughness with wavelength of 400nm and amplitude of 10nm for diameter. The spatial computation step is 5nm in y and z direction, and 10 nm in x direction. Figure 7-11 shows the surface roughness near the tip by plotting the

number of computation grid points within the nanowire on each yz plane against the location of the yz plane.

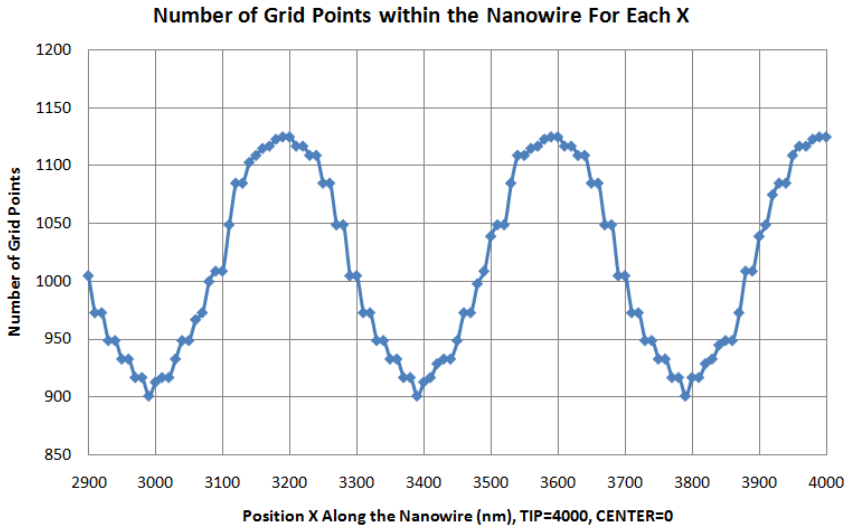

Figure 7-11: Illustration of surface roughness by the number of grid points contained by the nanowire at different positions along the nanowire.

We follow the same procedures as those in the previous section, and obtain the $I_S^{Ram}(LaserX)/I_S^{Ram}(0)$ from a nanowire with such sinusoidal surface roughness in Figure 7-12. In this figure, we still have our strongest Raman intensity at 500nm away from the tip, the same as the result from a smooth nanowire. The enhancement factor in this model is 1.46, almost the same as the enhancement factor from a smooth nanowire. A unique feature here is the dip at 600nm away from the tip. This can be explained by the diameter dip at 600nm away from the tip as depicted in Figure 7-11. Electric fields near the surface of x = 3400nm are expected to be smaller than those fields at its two sides, and dipoles near surface have more contributions to the electric fields within the emission

collection area which has already been illustrated by Figure 6-13 (b). These two factors together, lead to the dip in Raman intensity for x = 3400nm.

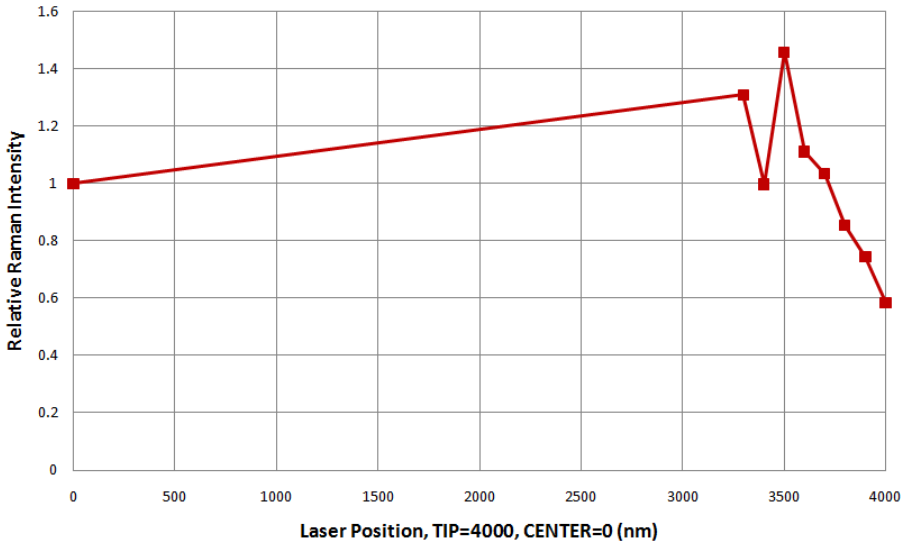

Figure 7-12: Relative Raman intensity $I_S^{Ram}(LaserX)/I_S^{Ram}(0)$ when laser incident on different positions $LaserX$ of the GaP nanowire with rough surface.

7.5 Hot Tip Effect Experimental Procedures for GaP Nanowires on TEM Grids

The GaP nanowires studied were fabricated by CVD as described in Chapter 2.4. The nanowires were harvested from the quartz boat and did not have gold particles on their tips. Figure 7-13 shows TEM images for 6 different GaP nanowires over TEM grid. The diameters of the nanowires studied here are between 100nm to 200nm. Their tips have different shapes but none of them have gold particles attached.

The procedures for experiments with GaP nanowires on TEM grids are the same as the procedures described in Chapter 7.2. However, in addition to the 514.5nm excitation with polarization parallel to the nanowire axis, we also investigated the nanowires under 514.5nm excitation but with polarization perpendicular to the nanowire axis, and 488nm and 647nm excitation with polarization parallel to the nanowire axis. The order of experiments was parallel 514.5nm, perpendicular 514.5nm, 488nm, 647nm, and TEM. Studies under 514.5nm excitation with polarization parallel to the nanowire axis have the largest sample space, and subjects under other studies are randomly drawn from the parallel 514.5nm sample space.

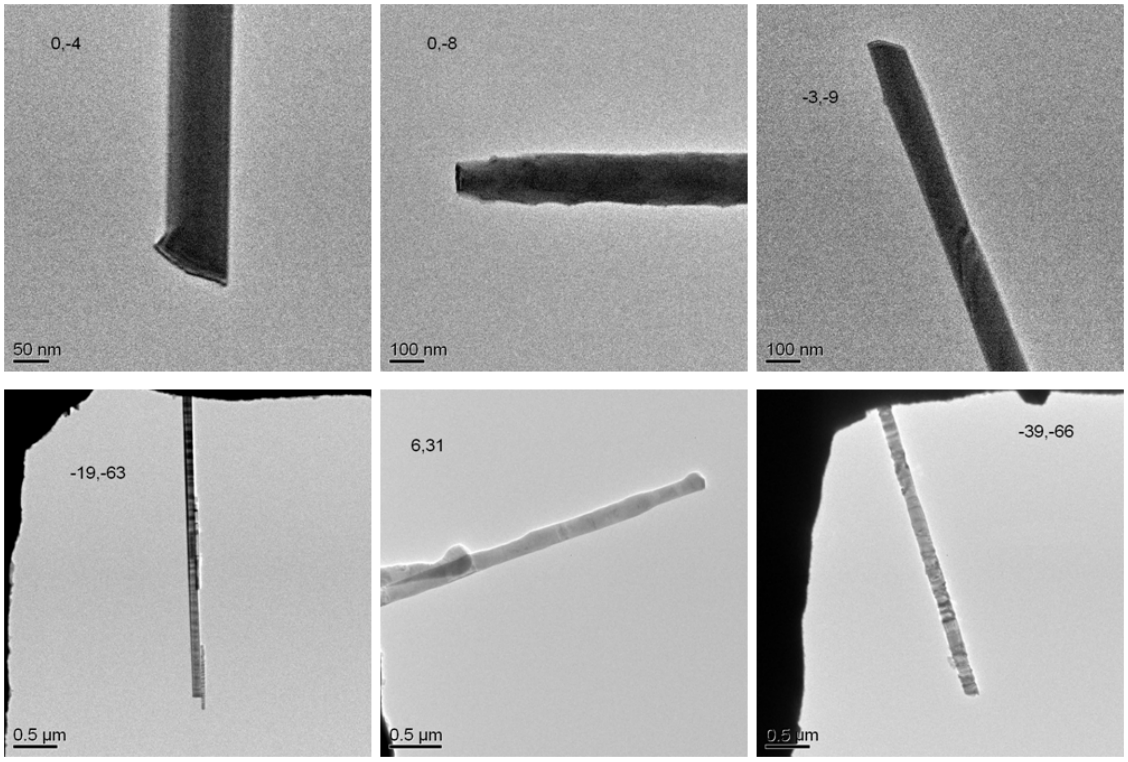

Figure 7-13: Selected TEM image of GaP nanowires over TEM grid.

7.6 Results and Discussions for GaP Nanowires on TEM Grids

7.6.1 Hot Tip Effect's Dependence on Incident Laser's Polarization

NWID	EF(514) parallel	EF(514) perpendicular
0,-4	1.13	1.32
0.-8	1.69	5.96
6,31	2.14	2.61
-6,-74	1.21	2.83
-7,-63 top	1.57	1.14
-39,-66	1.77	1.23
-42,-67 top	1.80	1.32
-19,-63	1.67	0.79
-42,-67 bottom	1.91	0.78
-7,-63 bottom	0.75	1.66
-3,-9	1.06	1.00

Table 7-1: Comparison of enhancement factor (EF) for GaP nanowires on TEM grid when excited by laser with different polarization.

The experimental results for the test of hot tip effect's dependence on incident laser's polarization are summarized in Table 7-1. We studied 9 samples in total, under 514.5nm excitation with polarization parallel to the nanowire axis and 514.5nm excitation with polarization perpendicular to the nanowire axis. 4 of the 9 nanowires shadowed in Table 7-1 exhibit significantly different enhancement factors excited by the two different polarizations. For each of these 4 samples, the enhancement factor under one polarization is at least twice as greater as the EF under the other polarization. Therefore, the enhancement factor under one polarization is not the same as the enhancement factor under the other polarization. Besides, a test for correlation between

the two groups of enhancement factors reveals the correlation is only 0.1 which indicates nearly no linear relation between these two group of enhancement factors.

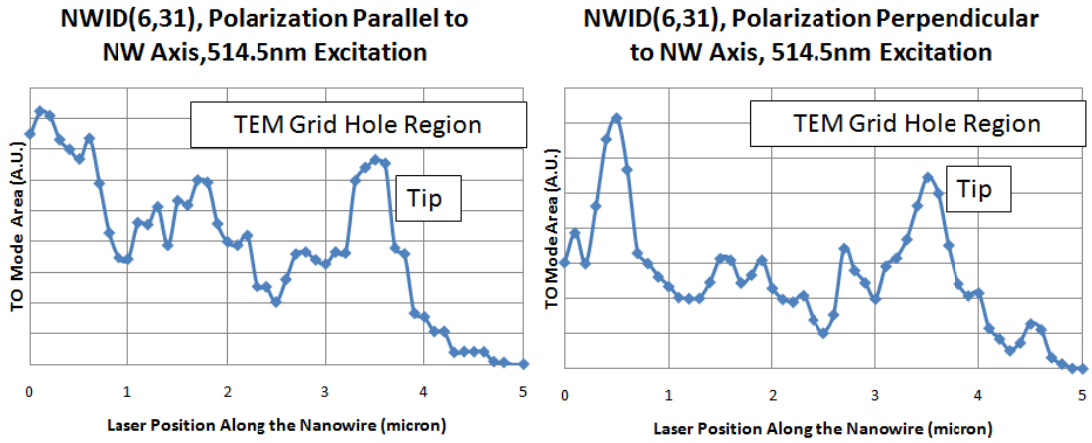

Figure 7-14: A GaP nanowire on TEM grid shows hot tip under both 514.5nm excitation with polarization parallel to the nanowire axis and 514.5nm excitation with polarization perpendicular to the nanowire axis.

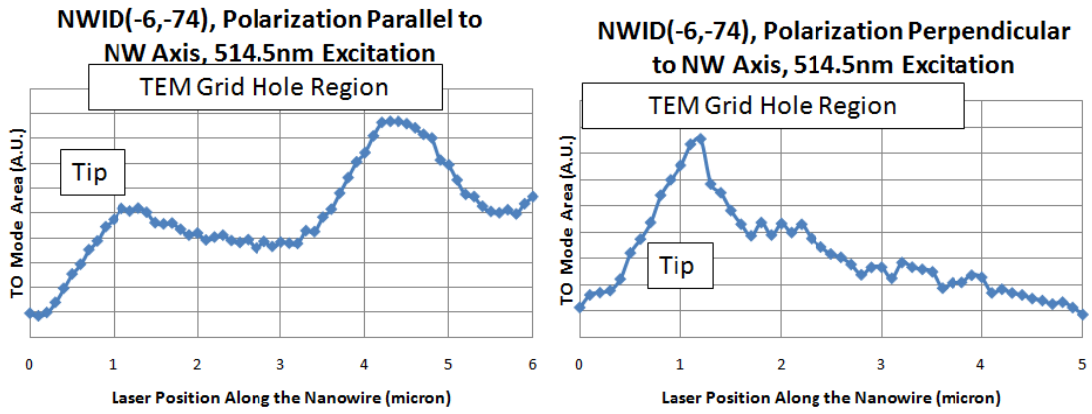

Figure 7-15: A GaP nanowire on TEM grid shows hot tip only under 514.5nm excitation with polarization perpendicular to the nanowire axis.

Figure 7-14 and Figure 7-15 are two examples of GaP nanowires. The first exhibits hot tip effects independent of the polarization of the incident laser, while the second nanowire only shows a hot tip effect when the polarization of the incident laser is perpendicular to the nanowire axis.

7.6.2 Hot Tip Effect's Dependence on Incident Laser's Frequency

NWID	EF(488)	EF(514)	EF(647)
0,-4	1.59	1.13	
0.-8	1.03	1.69	0.79
6,31	0.80	2.14	1.93
-6,-74	2.81	1.21	1.29
-7,-63 top	1.44	1.57	3.53
-7,-63 bottom	0.74	0.75	
-19,-63	1.93	1.67	0.93
-39,-66	2.12	1.77	1.33
-42,-67 bottom	6.08	1.91	1.23
-42,-67 top	1.59	1.80	0.84

Table 7-2: Summary of hot tip effect's dependence on incident laser's energy.

In this section, we investigate the hot tip effect from three different laser excitations – 488nm, 514.5nm and 647nm. The photon energies from both 488nm and 514.5nm are between the direct and indirect bandgap of a GaP crystal. The 647 excitation is below the indirect bandgap.

The experimental results for the test of hot tip effect's dependence on incident laser's frequency are summarized in Table 7-2. To obtain the hot tip effect's dependence

on the incident laser frequency, we will test two hypotheses: (1) the enhancement factor increases under a higher frequency excitation which means the condition that the incident photon energy is closer to the bandgap is a favorable factor for the EF; (2) the enhancement factor decreases under a higher frequency excitation which means the condition that the incident photon energy is closer to the bandgap is an unfavorable factor for the EF.

In Table 7-2, the blue colored row (NWID: -7, -63 top) is a clear conflict to our first hypothesis and the red colored rows (NWID: (0,-4); (-19, -63); (-39,-66); (-42, -67 bottom)) are conflicts to the second hypothesis. The shadowed rows exhibit mixed trends for increasing incident photon energy. Therefore, we cannot draw any definite conclusions for the two proposed hypotheses.

A noteworthy point here is that since we are comparing enhancement factors from different excitation energies, we must be aware that resonance inside the nanowire could be different for cases with different incident laser's wavelength. This resonant effect is presented in section 7.7. It adds complexity to our analysis for the hot tip effect dependence on incident laser energy, but does not affect our conclusion here that we do not have sufficient data to draw any statistically significant inference.

Figure 7-16 shows the line profile the Raman intensity as the laser scans along the nanowire axis. Both nanowires have hot tip effect under 514.5nm excitation, but the nanowire shown on the left column exhibits hot tip effect under 488nm excitation but not 647nm excitation, while the nanowire shown on the right column has hot tip effect under 647nm excitation but not 488nm excitation.

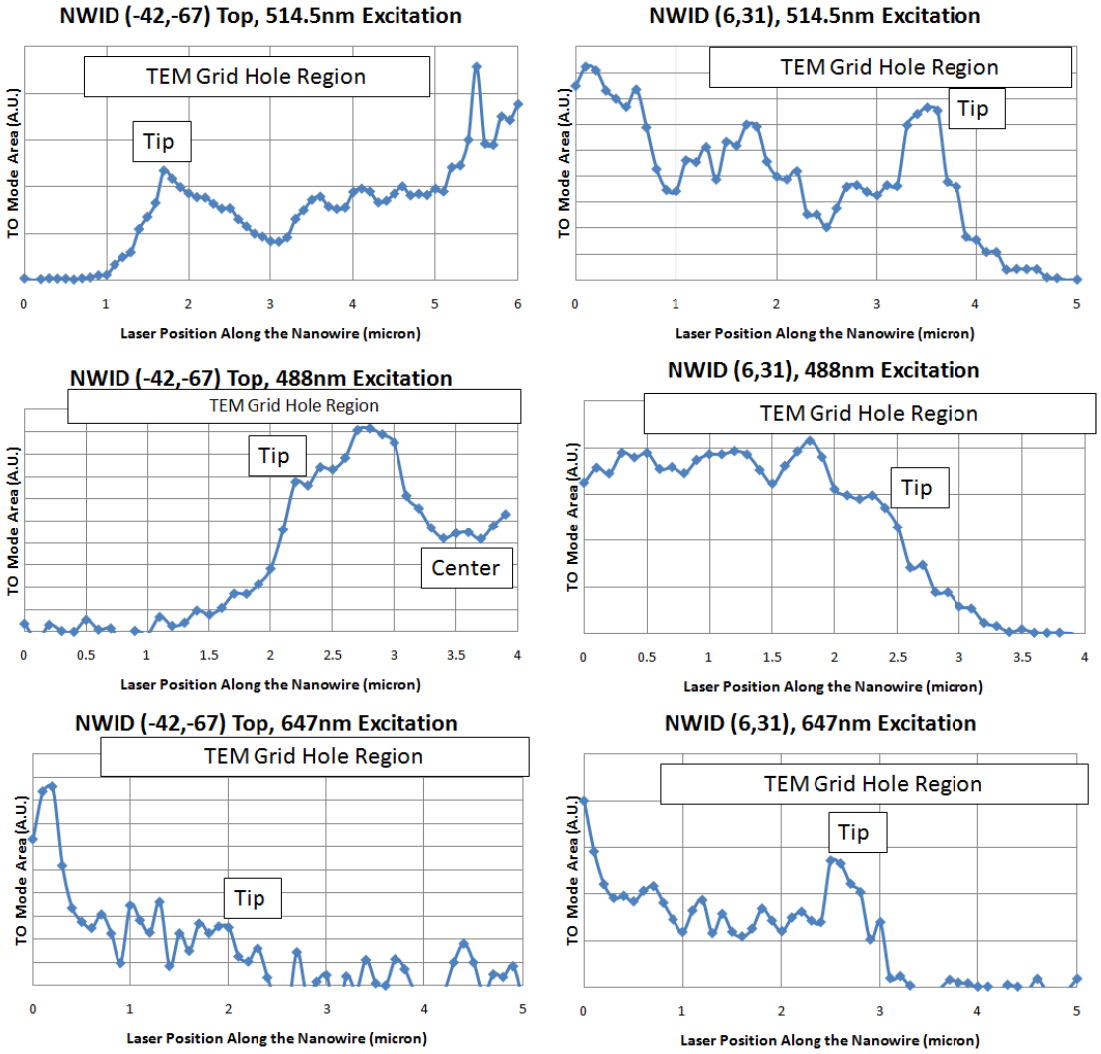

Figure 7-16: Examples of two GaP nanowire on TEM grid with hot tip effect under 514.5nm excitation exhibit different behavior under 488nm and 647nm excitation.

7.6.3 Factors Correlated to Hot Tip Effect

In this section, we will explore phenomena associated with hot tip effect. Before this discussion, I will first present several definitions and the treatment for data.

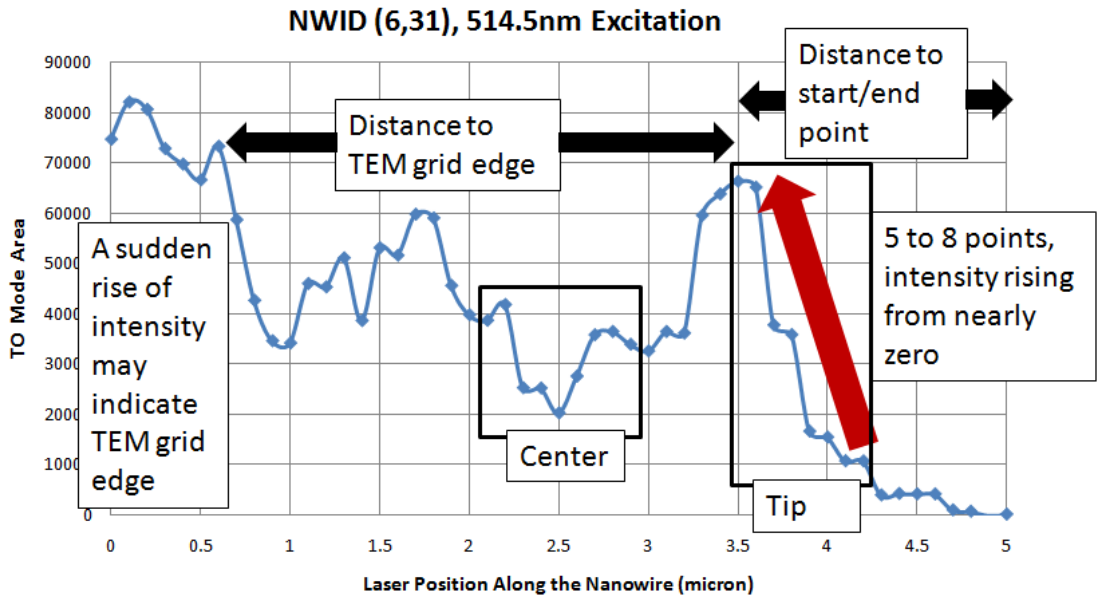

Figure 7-17: Illustration of how to find tip and center on a Raman intensity line scan profile.

Since the tip position is not directly labeled on a Raman intensity line scan profile, and the recorded scanned lines such as those in the insets of Figure 7-4 through Figure 7-6 are usually not accurate due to imperfect stage coordinates calibration, we are flexible in defining the "tip" in a Raman intensity line scan profile. We want to limit this flexibility here so that we can have a uniform treatment for all data.

Figure 7-17 illustrates the procedures to mark the tip. From the FDTD simulations in this chapter, we have learnt that starting from the tip until 500nm away from the tip, the Raman intensity increases as the laser spot moves along the nanowire axis towards the center. That result is based on the assumption that our laser spot is strictly 1 micron in diameter. We release this restriction a little bit, and expect that the Raman intensity right

on the tip is a start point for a continuously increasing curve from a relative small value to a regional maximal value within 800nm. Thus, the region between that starting point and the regional maximal point is defined as “Tip Region”. We verify this region by two ways. The recorded scanned lines such as those in the inlets of Figure 7-4 to Figure 7-6 are off the actual scanning lines, but they still provide useful information for possible positions of the scanning start/end point and TEM grid edge. The position of TEM grid edge can be further verified in a line scan profile as a sudden increasing of Raman intensity around the possible point of TEM grid edge. The actual distance between TEM grid edge and nanowire tip can be measured from TEM image. Therefore, we can check the position of tip by tip’s distance to TEM grid edge and scanning start/end point.

From Figure 7-9, we have learnt that the Raman intensity decreases quickly after the laser passes the maximal Raman intensity position for a smooth nanowire. Therefore, on a Raman intensity line scan profile, we label the region containing the minimal intensity as long as that position is at least 500nm away from the maximal intensity point in the tip region to be the center region. We use the same number of points in the center region as the number of points in the tip region.

As long as we are able to identify at least 5 points for the tip and center region, respectively, we include that nanowire for our study. The nanowire may be polycrystalline, may have a sharp tip or even a smaller nanowire attached to the tip (NWID: -19,-63 in Figure 7-13).

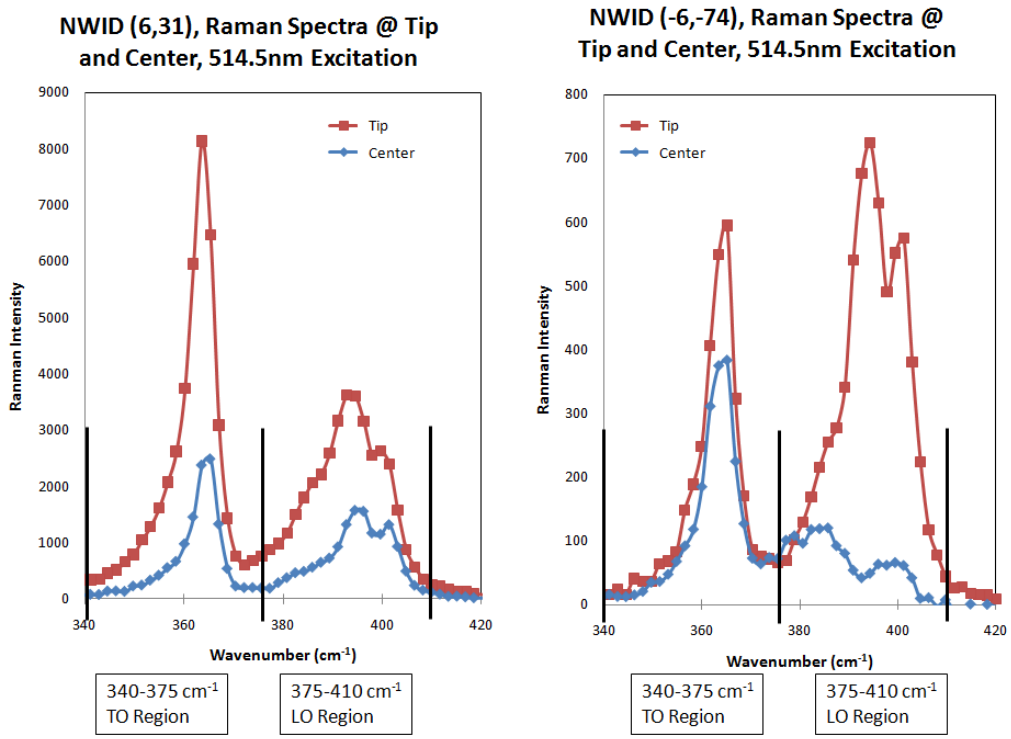

Figure 7-18: Examples of significant different spectra taken at the tip and center of a GaP nanowire on TEM grid.

After the definition of tip region and center region, we review the Raman spectra taken from the tip and center as depicted in Figure 7-18. One of the obvious difference is the peak shift in the LO region. We quantify all the differences and later investigate the correlation between these differences and hot tip enhancement factor.

We denote x as the position along nanowire – the horizontal axis in a Raman intensity line scan profile, k as the wavenumber (in unit of cm^{-1}) in a Raman spectrum, and $I(k)$ as the intensity for a specific k in a Raman spectrum.

For each x in a Raman intensity line scan profile, we have one Raman spectrum $I(k)$ vs. k. TO and LO mode area has already been defined in Eq. (7.1). Here we define peak position of TO and LO as:

$$POS_{TO}(x) = \frac{\sum_{k=340}^{375} I(k)\cdot k}{\sum_{k=340}^{375} I(k)}, \tag{7.10}$$

$$POS_{LO}(x) = \frac{\sum_{k=375}^{410} I(k)\cdot k}{\sum_{k=375}^{410} I(k)}. \tag{7.11}$$

The width of TO and LO mode is defined as:

$$WID_{TO}(x) = \sqrt{\frac{\sum_{k=340}^{375} I(k)\cdot[k-POS_{TO}(x)]^2}{[\sum_{k=340}^{375} I(k)]-1}}, \tag{7.12}$$

$$WID_{LO}(x) = \sqrt{\frac{\sum_{k=375}^{410} I(k)\cdot[k-POS_{LO}(x)]^2}{[\sum_{k=375}^{410} I(k)]-1}}. \tag{7.13}$$

Therefore, for each nanowire, its LO or TO peak position and width at the tip or center region is the average of corresponding equation among Eq. (7.10) – (7.13) over x in the tip or center region. The TO or LO enhancement factor is defined as the ratio of maximal TO or LO area in the tip region to average TO or LO area in the center region. All these quantitative values are summarized in Table 7-3. In Table 7-3, "T" means "Tip" and "C" represents "Center". We will further normalize these data, but first compute the average and standard deviation of peak position and width for LO and TO by pooling data from tip and center together. The normalized TO peak position is defined as:

$$N\_POS\_TO(T\ or\ C) = \frac{POS\_TO(T\ or\ C) - Average(POS\_TO)}{Stdev(POS\_TO)}. \tag{7.14}$$

NW ID	TO T/C	LO T/C	POS_TO T	POS_TO C	WID_TO_T	WID_TO_C	POS_LO T	POS_LO C	WID_LO T	WID_LO C
-14,-75	0.72	0.82	364.57	363.76	5.29	5.29	387.05	386.15	7.75	8.02
-7,-63 bottom	0.75	1.14	363.59	363.47	4.63	4.73	392.77	390.68	7.01	7.65
-40,-69	0.82	0.83	362.95	363.23	5.14	5.21	387.82	386.99	8.69	9.00
-14,-66	0.85	0.85	363.92	364.19	5.93	5.74	385.94	386.17	7.78	7.81
-28,-65	1.00	0.73	366.00	365.14	5.64	5.63	385.50	386.46	8.83	8.64
-17,-67	1.05	1.23	363.24	364.42	5.39	5.45	387.07	385.95	7.85	7.86
-3,-9	1.06	3.82	362.64	364.01	5.01	4.98	392.09	387.47	7.11	8.28
0,-4	1.13	1.14	364.45	364.31	5.20	5.16	387.10	386.48	8.10	7.93
-6,-74	1.21	2.32	363.11	363.20	4.64	4.72	394.07	391.87	7.16	8.13
-7,-63 top	1.57	3.15	363.17	363.18	4.81	5.07	392.02	387.85	6.80	8.09
-19,-63	1.67	1.70	363.15	362.54	5.13	5.03	388.58	388.84	7.99	8.19
0.-8	1.69	2.41	363.65	363.90	4.45	4.65	396.27	394.49	7.45	8.24
-39,-66	1.77	2.60	361.79	362.00	4.67	4.51	392.86	391.65	8.35	8.29
-42,-67 top	1.80	2.89	362.30	362.07	4.88	4.96	392.99	390.13	7.40	7.74
-42,-67 bottom	1.91	2.85	362.08	362.37	5.00	4.98	391.65	391.25	7.35	7.73
6,31	2.14	2.00	362.56	363.02	4.57	4.50	392.93	393.53	7.59	7.52
			Average() Stdev()		Average() Stdev()		Average() Stdev()		Average() Stdev()	

Table 7-3: Summary of LO and TO enhancement factor, peak position and width from tip and center for all GaP nanowires on TEM grid.

The other normalized variables follow the similar definition in Eq. (7.14). These normalizations assure us to compare the effects from different variables on an equal footing.

The TO peak position and TO peak width have relatively small deviations among GaP nanowires and between tips and centers. Any TO properties has little correlations with the TO enhancement factor.

LO enhancement factor, as we have already observed in above line scan profiles, is highly correlated with the TO enhancement factor. However, $(\frac{LO}{TO})_T/(\frac{LO}{TO})_C$, an indicator for change of nanowire growth direction, does not exhibit linear relation with TO enhancement. Therefore, twinnings along the nanowire axis are not responsible for tip enhancement or suppression.

LO peak positions and width vary a lot among nanowires or between tip and center of the same nanowire. TO tip enhancement factor has a stronger positively linear relation with LO peak position at the center and a weaker positively linear relation with the LO peak position at the center. The enhancement factor does not correlate with LO peak width either at the tip or at the center. Besides, the LO peak position at the tip is highly correlated with the LO peak position at the center.

The regression equation for TO enhancement factor against LO peak position at the center $N\_POS\_LO\_C$ is:

$$EF(TO) = 1.396 + 0.355 \cdot N\_POS\_LO\_C + \epsilon\,, \tag{7.15}$$

where the last term ϵ is the error term and it represents contributions to EF(TO) from factors other than the $N\_POS\_LO\_C$.

Regression Statistics	
Multiple R	0.697
R Square	0.486
Adjusted R Square	0.449
Standard Error	0.344
Observations	16.000

ANOVA

	df	*SS*	*MS*	*F*	*Significance F*
Regression	1	1.564	1.564	13.217	0.003
Residual	14	1.657	0.118		
Total	15	3.222			

	Coefficients	*Standard Error*	*t Stat*	*P-value*	*Lower 95%*	*Upper 95%*
Intercept	1.396	0.088	15.795	0.000	1.206	1.585
N_POS_LO_C	0.355	0.098	3.636	0.003	0.145	0.564

Table 7-4: Tables of fitting results for linear regression.

The y-intercept in Eq. (7.15) is the enhancement factor we should obtain if the nanowire have its LO peak at the average position. This number is very close to the enhancement factor obtained from FDTD simulation.

The enhancement factor is positively correlated with the LO peak position at the center and the tip. Therefore, the LO peak position represents the characteristics of the whole nanowire. Any effect causing the LO peak position to upshift is possibly responsible for the hot tip effect, such as strain. Since the LO mode in this study is actually the mixure of LO and SO mode, any downshift of the SO mode or increase in the SO/LO ratio would suppress of the enhancement factor. Because increasing the dielectric constant of the surrounding medium would downshift the SO mode [26], coatings around the GaP nanowires could downshift SO peak position and decrease enhancement factor.

Adding any other variables, even the LO enhancement factor, to Eq. (7.15) does not make the additional variable statistically significant for a multi-variable linear regression. With the difficulty in quantifying the geometrical information in the TEM image, Eq. (7.15) is the best we can achieve.

In Figure 7-19, the blue diamonds represent measured TO enhancement factors from each GaP nanowire and is plotted against computed $N\_POS\_LO\_C$. The red straight line is the prediction of enhancement factors which Eq. (7.15) gives. From this figure, we can see that the fit works well when the $N\_POS\_LO\_C$ is either small (~ -1) or large (> 1), but when the $N\_POS\_LO\_C$ is near zero, our fit deviates away from the measurements. This explains that the $N\_POS\_LO\_C$ is the main factor affects EF and when its value diminishes to zero, contributions to the EF from other unidentified minor factors start to dominate and deviate our predictions away from the measurements.

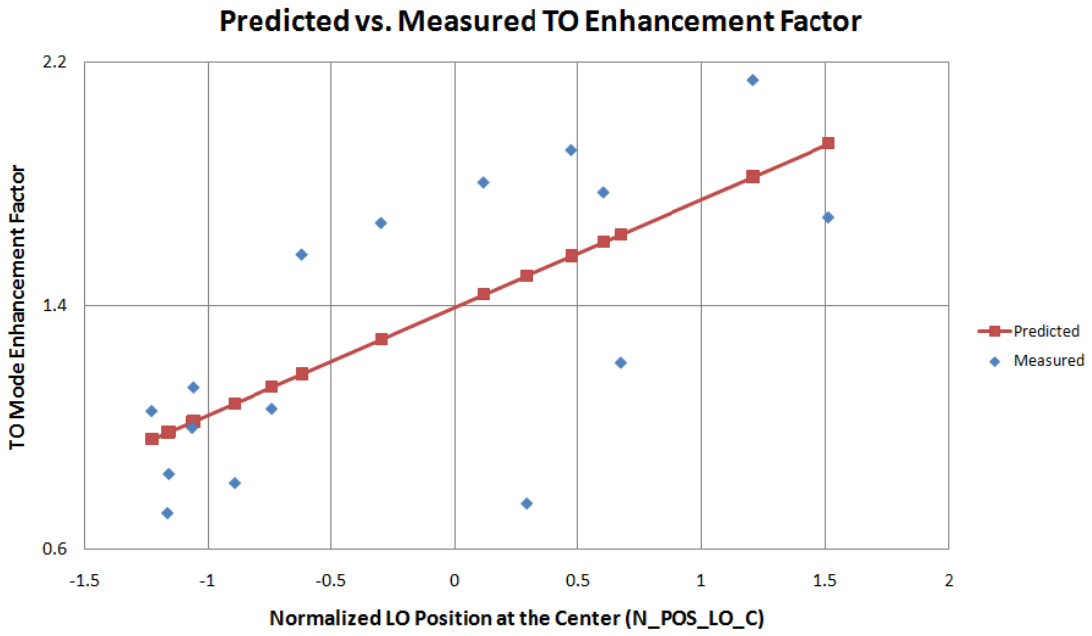

Figure 7-19: Comparison between measured TO enhancement factor and predicted TO enhancement factor vs. normalized LO region peak position using Eq. (7.15).

7.7 FDTD Simulations for E Field Resonance within GaP Nanowires

In the previous section, we explained the variance in TO enhancement factors using raw and structured experimental data. Here, we show that the variance may due to different degree of resonance inside GaP nanowires with different diameters. We applied FDTD method to compute electric field distributions and intensities inside the nanowire and within the laser spot. The simulations presented here were performed in the early stage of the whole hot tip effect project and thus some simulation parameters used here were not the same as those presented before. For example, the waist of incident laser is

220nm compared to the 663nm used elsewhere in this dissertation. This waist does not represent the experimental condition and therefore the simulation results in this section should not be compared to either the experimental results or the simulation results in other sections. Besides, the length of the nanowire used here is 10 microns. However, a comparison of the total electric field intensity within the laser spot inside the GaP nanowires with different diameters, as illustrated in Figure 7-20, clearly shows that for certain diameter we observe relatively large resonance compared to the resonances in other nanowires.

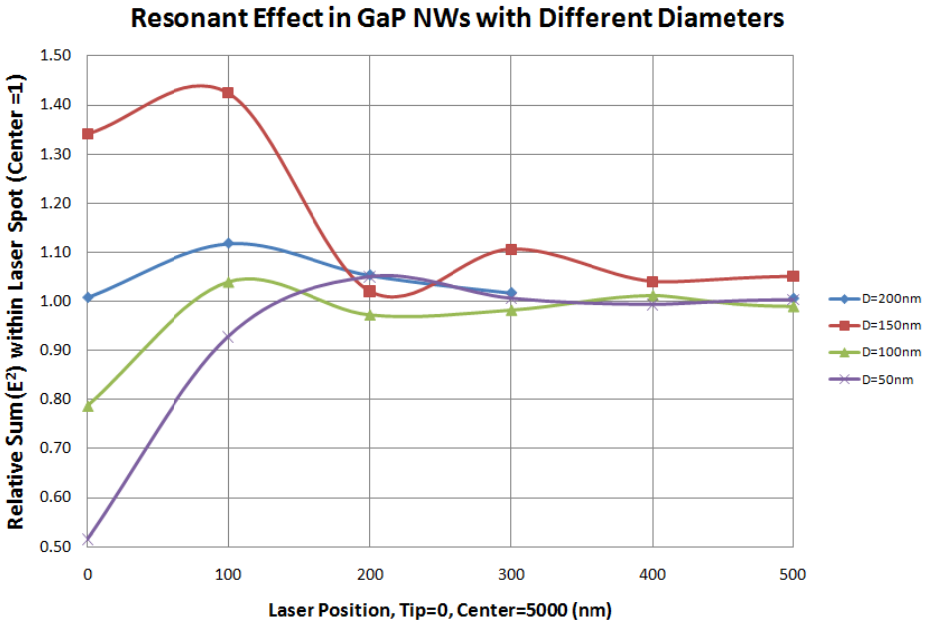

Figure 7-20: E field resonance inside GaP nanowires with different diameters.

In Figure 7-20, the x-axis records the position of incident laser spot relative to the nanowire tip. Zero on the x-axis represents that the center of laser spot is at the tip of the nanowire and 500 on the x-axis means that the center of the laser spot is on the nanowire

axis and 500nm away from the tip. The y-axis represents the sum of electric field intensity within the laser spot and inside the nanowire when the center of the laser spot is at x divided by the sum of electric field intensity when the center of the laser spot is at the nanowire center (x=5000). For this set of simulations, a large resonance occurs when the diameter of the nanowire is 150nm. Therefore, we believe that when certain conditions meet, such as the relative position of laser to the nanowire tip and a combined requirement for laser wavelength, nanoiwre's diameter and length, there constructs a strong electric resonance inside the nanowire and thus the nanowire exhibits a large enhancement factor.

7.8 Conclusion

The hot tip effect for GaP nanowires grown by either PLV or CVD method is not correlated with the polarization of the incident laser, nor does it correlate with the incident laser's energy. The theoretical enhancement factor is 1.40 for a well-shaped smooth nanowire and this value is in good agreement with the y-intercept in the fit of experimental data from GaP nanowires on TEM grids. Electric field resonance inside nanowire is a possible explanation to the variance of enhancement factors among nanowires. Other underlying factors increasing or decreasing the EF remain unknown. However, we know from the fit that the underlying factor(s) should also affect the peak positions of the LO or SO mode or the relative intensity of LO/SO. The mechanism for additional enhancement from GaP on Si substrate hasn't been studied yet. There is a long journey ahead for a thorough understanding of the hot tip effect.

References

1. Lu, W., et al., *Nanoelectronics from the bottom up*. Nature Materials, 2007. **6**: p. 841 – 850.
2. Wagner, R. S., et al., *Vapor-Liqui-Solid Mechanism of Single Crystal Growth.* Applied Physics Letters, 1964. **4**(5): p. 89-90.
3. Wu, Y., et al., *Direct Observation of Vapor-Liquid- Solid Nanowire Growth.* Journal of Chemical Society, 2001. **123**(13): p. 3165-3166.
4. Lew, K.K., et al., *Vapor-Liquid-Solid Growth of Silicon-Germanium Nanowires.* Anvanced Materials, 2003. **15**(24): p. 2073-2076.
5. Adu, K. W., *Synthesis and Raman Scattering Studies of Novel Semiconductor Nanostructures:Si , Ge and GaAs Twinning Superlattice Nanowires.* Ph.D. Thesis, 2004.
6. Long, D. A., *The Raman Effect: A Unified Treatment of the Theory of Raman Scattering by Molecules*. 2002, West Sussex: John Wiley & Sons.
7. *Horiba Jobin Yvon T64000 manual.* Horiba Ltd.
8. *Renishaw InVia Micro-Raman System Manual.* Renishaw Plc.
9. Meyer, D. J., et al., *Applications and processing of SiGe and SiGe:C for high-speed HBT devices.* Materials Science in Semiconductor Processing, 2001. **4**(6): p. 529-533.
10. Paul, D. J., *Silicon germanium heterostructures in electronics: the present and the future*. Thin Solid Films, 1998. **321**(1-2): p. 172-180.
11. Yang, J. E., et al., *Band-Gap Modulation in Single-Crystalline $Si_{1-x}Ge_x$ Nanowires*. Nano Letters, 2006. **6**(12): p.2679-2684.
12. Lee, J., et al., *Responsivity and impact ionization coefficients of $Si_{1-x}Ge_x$ photodiodes*. IEEE Transactions on Electron Devices, 1996. **43**(6): p. 977-981.
13. Weber, J., et al., *Near-band-gap photoluminescence of Si-Ge alloys*. Physical Review B, 1989. **40**(8): p. 5683-5693.
14. Giannozzi, P., et al., *Ab initio calculation of phonon dispersions in semiconductors*. Physical Review B, 1991. **43**(9): p. 7231-7242.
15. Beraud, A., et al., *Disorder-induced broadening of transverse acoustic phonons in Si_xGe_{1-x} mixed crystals*. Physica B, 2004. **350**(1-3): p. 254-257.
16. Rat, E., et al., *Disorder broadening of the acoustic branches in Si_xGe_{1-x} mixed crystals*. Physica B, 2000. **276-278**: p. 429-430.
17. Molinas-Mata, P., et al., *Phonon dispersion relations for Ge/Si superlattices grown along the [100] and [111] directions*. Superlattices and Microstructures, 1991. **10**(1): p. 39-46.

18. Molinari, E., et al., *Calculated phonon spectra of Si/Ge (001) superlattices: Features for interface characterization*. Applied Physics Letters, 1989. **54**(13): p.1220-1222.
19. Ren, S. F., et al., *Microscopic investigation of phonon modes in SiGe alloy nanocrystals*. Physical Review B, 2004. **69**(23): p. -.
20. Alonso, M. I., et al., *Raman spectra of c-$Si_{1-x}Ge_x$ alloys*. Physical Review B, 1988. **39**(14): p. 10056-10062.
21. Sharma, V., et al., *Optical Properties of Ge Nanowires Grown on Silicon (111) and (100) Substrates*. Materials Research Society Symposium Proceedings, 2005. **832**: p. 329-334.
22. Kolobov, A. V., *Raman scattering from Ge nanostructures grown on Si substrates: Power and limitations*. Journal of Applied Physics, 2000. **87**(6): p. 2926-2930.
23. Sheng, C., et al., *Suppression of Si-Ge interfacial vibration mode in the Raman spectrum of a Si6Ge4 superlattice*. Physical Review B, 1996. **53**(16): p. 10771–10774.
24. Watanabe, M., et al., *Absorption correction and thickness determination using the ζ factor in quantitative X-ray microanalysis*. Ultramicroscopy, 1996. **65**(3-4): p. 187-198.
25. Xiong, Q., et al., *Raman Scattering from Surface Phonons in Rectangular Cross-sectional w-ZnS Nanowires*. Nano Letters, 2004. **4**(10): p. 1991-1996.
26. Gupta, R., et al., *Surface Optical Phonons in Gallium Phosphide Nanowires*. Nano Letters, 2003. **3**(12): p 1745–1750.
27. Zhang, X., et al., *Diameter-Dependent Composition of Vapor-Liquid-Solid Grown $Si_{1-x}Ge_x$ Nanowires*. Nano Letters, 2007. **7**(10): p. 3241-3245.
28. Kim, J. M., et al., *Two-Photon Photopolymerized Tips for Adhesion-Free Scanning-Probe Microscopy*. Nano Letters, 2005. **5**(2): p. 309–314.
29. Zhang, Z., et al., *Raman scattering from surface optical phonon mode in gallium phosphide nanomaterials*. Journal of Nanopartical Research, 2010. 12(3): p. 961-966.
30. Lew, K. K., et al., *Effect of Growth Conditions on the Composition and Structure of $Si_{1-x}Ge_x$ Nanowires Grown by vapor-Liquid-Solid Growth*. Journal of Materials Research, 2006. **21**(11): p. 2876-2881.
31. Nishimura, C., et al., *Raman Characterization of Ge Distribution in Individual $Si_{1-x}Ge_x$ Alloy Nanowires*. Applied Physics Letters, 2008. **93**(20): p. -.
32. Bohren, C. F., et al., *Absorption and Scattering of Light by Small Particles*. 1983, New York: John Wiley & Sons.
33. Draine, B. T., et al., *Beyond Clausius-Mossotti: Wave Propagation on a Polarizable Point Lattice and the Discrete Dipole Approximation*. The Astrophysical Journal, 1993. **405**: p. 685-697.
34. Goodman, J. J., et al., *Application of fast-Fourier-transform techniques to the discrete-dipole approximation*. Optics Letters, 1991. **16**(15): p. 1198-1200.

35. Draine, B. T., et al., *User Guide for the Discrete Dipole Approximation Code DDSCAT 6.1*. http://arxiv.org/abs/astro-ph/0409262.
36. *OptiFDTD Technique Background and Tutorials*. Optiwave Systems Inc.
37. Ajiki, H, et al., *Carbon Nanotubes – Optical Absorption in Aharonov-Bohm Flux*. Japanese Journal of Applied Physics, 1994. **34**(1): p. 107-109.
38. Ajiki, H., et al., *Aharonov-Bohm effect on magnetic properties of carbon nanotubes*. Physica B, 1996. **216B**(3-4): p. 358-361.
39. Yu, P. Y., et al., *Fundamentals of semiconductors : physics and materials properties*. 2001, Berlin ; New York: Springer.
40. Cao, L., et al., *Enhanced Raman Scattering from Individual Semiconductor Nanocones and Nanowires*. Physical Review Letters, 2006. **96**(15): p. -.
41. Chen, G., et al., *Optical Antenna Effect in Semiconducting Nanowires*. Nano Letters, 2008. **8**(5): p. 1341-1346.
42. Xiong, Q., et al., *Raman scattering studies of individual polar semiconducting nanowires: phonon splitting and antenna effects*. Applied Physics A, 2006. **85**(3): p. 299-305.

Vita

Qiujie Lu

Education

Ph.D. in Physics, The Pennsylvania State University, USA 2004-2010

B.S. in Phyiscs, Fudan University, Shanghai, China 2000-2004

Awards

David C. Duncan Fellowship, The Pennsylvania State University, USA 2008

Tang's Fellowship, Fudan University, Shanghai, China 2001-2004

Publications and Presentations

- Polarized Raman scattering from single GaP nanowires

  Jian Wu, Duming Zhang, **Qiujie Lu**, Humberto R. Gutierrez, Peter C. Eklund. *Physical Review B,* 2010. 81(16).

- Raman Scattering from $Si_{1-x}Ge_x$ Alloy Nanowires

  Qiujie Lu, Kofi W. Adu, Humberto R. Gutiérrez, Gugang Chen, Kok-Keong Lew, Pramod Nimmatoori, Xi Zhang, Elizabeth C. Dickey, Joan M. Redwing, and Peter C. Eklund. *The Journal of Physical Chemistry C,* 2008. 112 (9): p. 3209-3215

- Optical Antenna Effect in Semiconducting Nanowires

  G. Chen, Jian Wu, **Qiujie Lu**, H. R. Gutierrez, Qihua Xiong, M. E. Pellen, J. S. Petko, D. H. Werner and P. C. Eklund. *Nano Letter*, 2008. *8* (5): p. 1341–1346

- Polarized Rayleigh and Raman Study of single CuO Nanowire

  Qiujie Lu, Jian Wu, Humberto R. Gutierrez, Timothy J. Russin, Peter C. Eklund. APS March Meeting 2009

- Enhanced Raman Scattering Near the Tip of Semiconducting Nanowires

  Qiujie Lu, Jian Wu, Awnish Gupta, Peter C. Eklund. APS March Meeting 2008

- Raman Scattering from Si1-xGex Alloy Nanowires

  Qiujie Lu, Kofi Adu, Xi Zhang, Kok-Keong Lew, Pramod Nimmatoori, Elizabeth C. Dickey, Joan M. Redwing, Peter C. Eklund. APS March Meeting 2007